Title

Enhancing the Phase Separation Rate of Aqueous Two-Phase Systems for Applications in Point-of-Care Diagnostics

Author

Pereira, David

Publication Date

2017

Peer reviewed|Thesis/dissertation

UNIVERSITY OF CALIFORNIA

Los Angeles

Enhancing the Phase Separation Rate of Aqueous Two-Phase Systems for Applications in Point-of-Care Diagnostics

A dissertation submitted in partial satisfaction of the requirements for the degree Doctor of Philosophy in Bioengineering

by

David Pereira

2017

ABSTRACT OF THE DISSERTATION

Enhancing the Phase Separation Rate of Aqueous Two-Phase Systems for Applications in Point-of-Care Diagnostics

by

David Pereira

Doctor of Philosophy in Bioengineering

University of California, Los Angeles, 2017

Professor Daniel T. Kamei, Chair

Aqueous two-phase systems (ATPSs), traditionally utilized in industrial bioseparations, are showing increasing potential as an approach for concentrating components in paper-based point-of-care bioassays. Specifically, our lab was the first to demonstrate that ATPSs can increase the sensitivity of the lateral-flow immunoassay (LFA) by concentrating biomarkers into one of the two phases, after which, the phase containing the concentrated biomarkers was extracted prior to their detection. While this method demonstrated consistent improvements to the LFA, its applicability in point-of-care settings was restricted by two main factors. First, the time to separate into two distinct phases varied among different classes of ATPSs, but usually required hours to achieve effective biomolecule concentration. Second, the method required several user steps in the form of sample mixing with the ATPS components, and the subsequent extraction and application of the phase containing the concentrated biomolecule to the LFA after phase separation occurred. More recently, our lab demonstrated that when the mixed,

homogenous ATPS was applied to a paper membrane, phase separation was observed within the paper membrane itself as the solution wicked across the paper. This largely unexplored phenomenon reduced the phase separation time of a polyethylene glycol (PEG)-salt ATPS from hours in a tube to minutes on paper.

This thesis focuses on advancing the phenomenon of paper-based phase separation as a means of enhancing the phase separation rate of ATPSs and making them more suitable for point-of-care applications. First, we extended the paper-based phase separation phenomenon to a naturally slow phase separating system, the Triton X-114 ATPS. Next, we investigated the dehehydration of the phase forming components directly into the paper matrix, and the subsequent phase separation upon resolubilization of the components by a liquid sample. Within these two investigations, the ATPS was then integrated with the LFA to improve the detection of biomarkers of infectious diseases such as malaria and chlamydia. Furthermore, we investigated the use of the Washburn equation as a mathematical framework to describe the flow behavior of ATPS phases within porous media in order to better predict phase separation behavior within paper.

The Triton X-114 ATPS is a micellar ATPS that is comprised of the Triton X-114 nonionic surfactant. This particular ATPS, previously used by our lab to concentrate biomarkers for the LFA, is one of the slowest separating systems, partially due to the small interfacial tension and density difference between its two phases (the micelle-poor and micelle-rich phases). We applied the Triton X-114 ATPS to paper membranes and demonstrated, using a distinctively different design in which the solution flows vertically up a multilayered paper wick, that paper-based phase separation can also be achieved with the Triton X-114 system. In this case, we found that gravitational effects had no influence on the flow of the dense gold nanoparticles as the less dense micelle-poor phase containing the gold wicked ahead of the micelle-rich phase. This was

the first time that a micellar ATPS was applied directly to a fiberglass paper membrane to significantly speed up its macroscopic separation from at least 8 hrs in a test tube to approximately 3 min on paper. The paper-based Triton X-114 ATPS was then integrated with the LFA to simultaneously concentrate a malaria protein biomarker into the leading micelle-poor phase, and then detect it without the need of a user-dependent phase extraction step. The single-step integration improved the LFA detection limit for the protein by 10-fold in buffered saline and complex serum media. This was also the first time within our lab that we concentrated an infectious disease biomarker in complex biological fluids.

The design used for the abovementioned Triton X-114 study is applicable when dealing with oral and vaginal swab samples as the swab would need to be mixed with a buffer solution to solubilize the target. However, in urine, saliva, or blood applications, one would prefer to just add the biological fluid to the device. The second focus of the thesis was therefore to further improve the user-friendliness of the ATPS-LFA integration by removing initial sample preparation steps. To achieve this, we investigated the novel concept of sequential rehydration of the two-phase components that were initially dehydrated into the paper matrix as a way to achieve paper-based ATPS phase separation. We used two different polymer-salt ATPSs: the PEG-salt system and the UCON-50-HB-5100 (UCON)-salt system, optimizing the component concentrations and rehydration order to yield the appropriate phase separation conditions for each system. Upon rehydration of the components, phase separation successfully occurred within the paper, leading to the formation of a leading polymer-poor phase and a lagging polymer-rich phase. As mentioned above, the benefit of this method is that a biological sample no longer needs to be manually mixed with the components and instead can be directly added to the device. These dehydrated systems were then integrated with the LFA to produce paper-based assays in which all the necessary components for target concentration and detection were stored within the

paper matrix. The dehydrated PEG-salt ATPS and UCON-salt ATPS were integrated with the LFA to simultaneously concentrate and detect large *Chlamydia trachomatis* whole bacteria and smaller human IgM antibodies, respectively. Ultimately, our designs demonstrated 10-fold improvements to the detection limits for both *Chlamydia trachomatis* and IgM, and could therefore improve LFA sensitivity without adding steps to the user. These exciting developments solve the initial limitations of the ATPS-LFA integration, making their use as point-of-care diagnostic devices for infectious diseases one step closer to reality.

Although paper-based phase separation of several different aqueous two-phase systems have been experimentally demonstrated, there is a need for a mathematical model that can accurately predict two-phase system wicking behavior in paper-based devices, as it would benefit the process of device design. We decided to evaluate the Washburn model as a framework for fluid flow of the PEG-salt ATPS and Triton X-114 ATPS in porous media. Using a combination of imbibition studies and characterization of the Washburn fluid parameters for each individual phase, we determined that the viscosity difference between the two phases is a dominant factor in the ability of a given ATPS to phase separate in paper. More specifically, the Washburn model correctly predicts that the less viscous phase will constitute the leading phase, independent of flow direction in a horizontal or vertical orientation. In this validation of the model, we then applied it to predict the phase separation capabilities of two polymer-polymer systems, the PEG-Dextran system and the PEG-polyacrylic acid (PEG-PAA) system. We predicted and successfully demonstrated that the PEG-PAA system could phase separate due to its large enough difference in phase viscosities, while the PEG-Dextran system could not phase separate due to its small viscosity difference. Furthermore, this theoretical framework was extended to predict the phase separation of ATPSs in polyethylene glycol dimethacrylate-based microporous hydrogels. We were able to predict and show for the first time that phase separation

of various ATPSs could be achieved within hydrogels, demonstrating that the phase separation enhancement phenomenon can occur in various types of porous media.

The dissertation of David Pereira is approved.

Gaurav Sant

Kyung Hyun Sung

Benjamin M Wu

Daniel T. Kamei, Committee Chair

University of California, Los Angeles

2017

This work is dedicated to my father, Gary, and to my mother, Cheri.

Nothing makes me prouder than to have followed in their footsteps.

TABLE OF CONTENTS

ACKNOWLEDGMENTS

First and foremost, my eternal gratitude goes to my principal investigator, Dr. Daniel Kamei. Throughout the five years I have spent as a member in his lab, he has pushed me to think more critically, to pay attention to the details, and to reason from first principles. One thing that sets him apart is that he emphasizes the importance of the thought process that goes into an experiment rather than the end result. Even if the result was bad, it was how we rationalized the result and articulated our next steps that mattered most to him. By having the opportunity to practice this skill on a daily basis, I can say that my craft as a researcher has dramatically improved thanks to his mentorship.

However, it was not only his work ethic, but his dedication to every member of his lab that resonated with me. His daily interactions with his students, as well as his willingness to pour hours into practice talks and proofreading manuscripts (such as this dissertation), speak volumes about his selfless character and values. Dan continuously pushes his students past their comfort zone out of an unconditional desire to see them achieve their full potential, not just as scientists or researchers, but as leaders and contributing members to society. He will be brutally honest about our mistakes, but when we succeed, he will be the most supportive person in the room. To this end, Dan is more than simply a mentor, but also a role model, a father figure, and a trusted friend. I believe it is impossible to leave his lab without becoming transformed in some way, and I like to think that as I move on to the next chapters in my life, I have also internalized his values and a high standard by which to conduct my professional and personal life.

I am also grateful for the past and present members of the lab that constitute the "Kamei-zing" family; each one holds a special place in my graduate school memories.

Ricky first introduced me to the diagnostics projects and spent many hours patiently training me on techniques related to aqueous two-phase systems and the LFA. He was an excellent mentor who valued my input and encouraged me to openly discuss my thoughts. I genuinely looked forward to bouncing ideas off of him each day. Furthermore, his ambition was contagious, and it fueled me during the time we overlapped in the lab. I am excited to be working with him again and taking my skill set to a new level at his company. Kristine was extremely supportive and welcoming to me from the start. Although we teased each other a lot of times, she was also a great friend whom I could approach whenever I needed advice or just some cheering up. Garrett was also extremely supportive of me and an excellent role model in terms of work ethic and resilience (among other things). His sense of humor made lab so much more enjoyable as we would laugh at each other's terrible jokes. Brian and Allison were undergrads at the time I joined, but made a significant impact on me during those first months I was getting accustomed to the lab. Their professionalism made coauthoring my first review paper with them quite enjoyable, and throughout the process we managed to bond and find many other similar interests. As for the current grad students, Sherine is extremely hard-working, persistent, and detail-oriented (although not as prone to laugh at my terrible jokes) while Brad is extremely sharp, quick to pick things up, and just as equally detail-oriented. I am confident that the lab is in good hands in the future.

I am also thankful for all the undergraduate students who have offered their time and energy to these projects. Sam Zhang was extremely helpful in running experiments for the malaria diagnostic project. She is a very independent worker with a critical eye, which was invaluable throughout the writing process as well. Chloe Wu provided immense help

with the dehydration project and also significantly spearheaded the work on the hydrogel experiments. We bonded over Thai food and ice cream (or rather, food in general) and she continues to amaze me with her work ethic and research capacity. I know she will be very successful in her own PhD studies at MIT. Emily Lee also helped tremendously with the dehydration project and the flow modeling experiments. Like Chloe, she has an analytical talent that amazes me and I'm excited to see what more she can accomplish in the future. It has been a rare privilege to work with such like-minded and dedicated individuals. This lab has given me the chance to explore, fail, learn and ultimately grow in so many aspects. Whether it was powering through a mathematical derivation, or spending weeks preparing for a conference talk, or even solving problems on the spot, each experience provided those intangible benefits that I could not imagine I would obtain any other way. Although leaving is bittersweet, the acquired friendships, values, and lessons will continue to be a part of me for the rest of my life.

Finally, I would like to thank certain friends and family who have shown me love and unwavering support.

Vincent – Vincent and I have lived under the same roof for 5 full years; I like to believe that we worked out so well as apartment mates because we have quite similar personalities. Throughout the years, he has helped me out of accidental lockouts, welcomed me into his home with his family for Thanksgiving, granted me the honor to be a groomsman at his wedding, and has been a trusted confidante when I needed to talk out my thoughts regarding graduate school and my personal life. I want to thank him for keeping me in his prayers when I needed it the most and for knowing just the right things to say to keep me going.

Rico – Rico has been my dance instructor, supportive friend, and a source of inspiration. As a fellow Leo, he demonstrates a professional, high-caliber work ethic and passion that I've rarely seen. I notice the way he can command a room and dominate his craft, and it fuels me to dominate mine in a similar fashion. At the same time, he is easygoing and uplifting, and never ceases to put a smile on my face.

Hamed – Although we probably met less than a year ago and our interactions mainly consisted of run-ins in the hallway, Hamed had this unending upbeat and friendly attitude. It did wonders in keeping up my spirits during some of my stressful times. Our conversations, sometimes light-hearted and other times deep, always consisted of mutual encouragement for one another. I am exceptionally grateful for these talks and will miss them in the future.

Furthermore, I would like to acknowledge the UCLA Wushu Team, Foundations Choreography, and the UCLA dance community for providing a space in which I could challenge myself, express myself, relieve stress, and develop a sense of balance that is so crucial to enduring graduate school. Despite the late-night hours in parking lots, I left each and every practice invigorated, and I continue to be extremely humbled by the amount of support I have received throughout the process. Most importantly, my UCLA experience would not have been nearly as rich nor fulfilling without the memories and friendships I developed from this supportive community.

Finally, I thank my mother for imparting her words of wisdom, for calming me down when I was stressed, and for having the expertise and insight to help me with my scientific problems, particularly in chemistry and nanoparticle synthesis. It was normal for us to talk on the phone for hours about one particular scientific topic. Those around me

assumed I was conversing with a labmate, only to be completely surprised upon hearing me say "Love you, mom" to end the conversation. I thank my father for stimulating my scientific curiosity, for making sure I maintain perspective, and for doing anything and everything it took to lift burden off my shoulders. My parents have made tremendous sacrifices to get me to this point, and although I have not always shown it, I truly appreciate it. I do not think they knew how much it pained me to have to deny their requests to come home or stay longer because I had work to do in lab, but I hope that it was all worth it. I could not ask for a more supportive family. I love them with all my heart.

Chapter 2 is a version of D.Y. Pereira, R.Y.T Chiu, S.C.L. Zhang, B.M. Wu, and D.T. Kamei, *Single-step, paper-based concentration and detection of a malaria biomarker*. Anal Chim Acta, 2015. 882: 83-89, doi:10.1016/j.aca.2015.04.040. Elsevier Copyright © 2015. Reprinted with permission of Elsevier. D.T. Kamei was the director of research for this article. This work was supported by UCLA funds to D.T. Kamei.

Chapter 3 is a version of G.L. Mosley, D.Y. Pereira, Y. Han, SY. Lee, C.M. Wu, B.M. Wu, and D.T. Kamei, *Improved lateral-flow immunoassays for chlamydia and immunoglobulin M by sequential rehydration of two-phase system components within a paper-based diagnostic*. Microchim Acta, 2017. 184: 4055-4064, doi:10.1007/s00604-017-2434-6 Springer-Verlag GmbH Austria 2017 Copyright © 2017. Reprinted with permission of Springer-Verlag GmbH Austria 2017. D.T. Kamei was the director of research for this article. This work was supported by an NSF SBIR grant 1549003 and a grant from the UCLA School of Dentistry. The authors acknowledge the help of Ivo Atanasov and the use of instruments at the Electron Imaging Center for NanoMachines and CNSI at UCLA.

VITA

2012	B.S., Biochemistry University of California, Santa Barbara Santa Barbara, CA
2013-2017	Teaching Assistant Department of Bioengineering University of California, Los Angeles

PUBLICATIONS

D.Y. Pereira, A.T. Yip, B.S. Lee, and D.T. Kamei, "Modeling mass transfer from carmustine-loaded polymeric implants for malignant gliomas" *JALA* **19**(1) (2014), 19-34.

D.Y. Pereira, R.Y.T. Chiu, S.C.L. Zhang, B.M. Wu, and D.T. Kamei, "Single-step, paper-based concentration and detection of a malaria biomarker", *Anal Chim Acta*, **882** (2015), 83-89.

G.L. Mosley, D.Y. Pereira, Y. Han, SY. Lee, C.M. Wu, B.M. Wu, and D.T. Kamei, "Improved lateral-flow immunoassays for chlamydia and immunoglobulin M by sequential rehydration of two-phase system components within a paper-based diagnostic" *Microchim Acta*, **184** (2017), 4055-4064. doi:10.1007/s00604-017-2434-6

PODIUM PRESENTATIONS

D.Y. Pereira, S.C.L. Zhang, C.M. Wu, S.Y. Lee, B.M. Wu, D.T. Kamei. “Improving Paper-based Protein-Detection with Dehydrated Two-Phase Micellar Components”, 2016 Biomedical Engineering Society Annual Meeting, Minneapolis, MN, October 2016.

D.Y. Pereira, R.Y.T. Chiu, S.C.L. Zhang, B.M. Wu, D.T. Kamei. "Single-step Concentration and Detection of a Malaria Biomarker in Serum", 2015 Biomedical Engineering Society Annual Meeting, Tampa, FL, October 2015.

D.Y. Pereira, R.Y.T. Chiu, S.C.L. Zhang, B.M. Wu, D.T. Kamei. "Single-step, Paper-based Concentration and Detection of a Malaria Biomarker in Serum", The Annual UC Systemwide Bioengineering Symposium, Santa Cruz, CA, June 2015.

Chapter 1. Motivation and Background

1.1 Introduction

1.1.1 Infectious Disease Detection in Resource-Poor Regions

Over 95% of deaths related to major infectious diseases (including malaria, acute respiratory infections, HIV, and tuberculosis) occur in resource-poor countries that have limited access to electricity, laboratory equipment, and trained personnel [1]. Many of these deaths would have been preventable had the disease been diagnosed at an early enough stage in its progression. Developing reliable diagnostic tests that can be used at the point-of-care (POC) can result in earlier disease diagnosis, improved patient treatment, and more efficient outbreak prevention.

The World Health Organization Sexually Transmitted Diseases Diagnostics Initiative established a set of generic development guidelines for diagnostic assays to be used in resource-poor settings. These guidelines are summarized under the acronym ASSURED [2]:

- **A**ffordable by those at risk of infection
- **S**ensitive (low occurrences of false positives)
- **S**pecific (low occurrences of false negatives)
- **U**ser-friendly (simple to use and requiring minimal training)
- **R**apid and robust
- **E**quipment-free
- **D**elivered to those who need it

These guidelines primarily aim to provide same-day diagnosis and therefore increase the total number of tests for these infections. While the most applicable assay that can be used for each ASSURED criterion depends on the disease or condition, the success of a specific assay generally relies on how well it satisfies all or most of the overall criteria relative to other assays (Table 1.1). For example, although the polymerase chain reaction (PCR) may be highly sensitive, it is generally not affordable, equipment-free, user-friendly, nor deliverable to rural areas. Therefore, current PCR technologies have not seen widespread use in these areas and have instead been limited to laboratories in the developing world.

Table 1.1 Advantages and disadvantages of common diagnostic assays and tests.

Type	Advantages	Disadvantages	Time to Obtain Results
Enzyme-linked immunosorbent assay (ELISA)	High throughput; sensitive; can be affordable	Requires lab equipment and power; requires multiple steps and personnel training	3-5 days
Polymerase chain reaction [3]	Very sensitive	Requires power and temperature control	2-3 days
Lateral-flow immunoassay [4,5]	Minimal training required; rapid results; no power necessary; affordable paper materials	Low sensitivity; not high-throughput	15-30 minutes
Cell culture and microscopy [6]	Can be sensitive and specific	Bulky equipment; requires trained personnel	1-2 weeks

1.1.2 The Lateral-Flow Immunoassay

One particular assay with potential in POC settings is the lateral-flow immunoassay (LFA). LFAs utilize antibodies to target a specific antigen, and use a colorimetric indicator, usually either gold colloidal nanoparticles or latex nanoparticles, to produce a readable signal.

Figure 1.1 illustrates a typical LFA configuration, which is comprised of several sequential zones that are typically comprised of different paper materials.

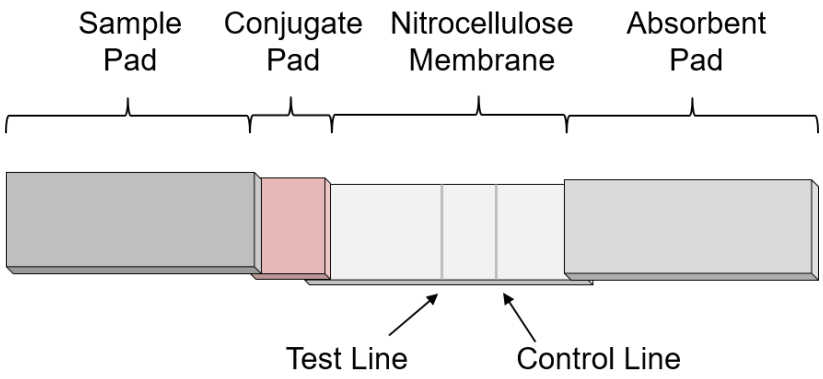

Figure 1.1 General schematic of a lateral-flow test strip.

In an LFA test, the sample solution is added to the sample pad located at the lower end of the test strip. The sample pad can be pretreated with blocking agents that enhance the lateral flow and prevent nonspecific binding of sample antigens to the paper membrane. The sample pad is typically made of either cellulose or glass fiber materials. This pad may also act as a filter for large particulate contaminants or other particles, such as red blood cells, that may be present in the sample. The second component is the conjugate pad, which contains dried and immobilized conjugate particles that are the colorimetric indicators of the test. In commercial tests, this particle is typically colloidal gold or a latex bead, but other possibilities include enzyme conjugates, other colloidal metals (e.g., silver nanoparticles), and fluorescent or paramagnetic particles. The third component is the nitrocellulose membrane which contains the test and control lines that constitute the detection zone. Finally, the absorbent pad wicks excess solution and acts as a sink to drive fluid flow across the strip. For this purpose, the absorbent pad is commonly made of a high-density cellulose material.

The assay format can be either sandwich (direct) or competitive (inhibitive). Sandwich assays are typically used to detect biomarkers with multiple antigenic sites, such as human chorionic gonadotropin (hCG), viruses, or bacteria. Antibodies specific to the target of interest are immobilized on the test line, while the same or similar antibodies that are also specific for the target are conjugated to the colorimetric gold indicator. The colloidal gold-antibody complex is henceforth referred to as a gold nanoprobe. Secondary antibodies specific to the primary antibody on the gold nanoprobe are typically immobilized on the control line. If the target molecules are present in a given sample, they will first bind to the antibodies on the gold nanoprobes. As the nanoprobe-antigen complexes move up the LFA strip, the target will also bind to the antibodies on the test line. In this case, a positive result is indicated by the presence of a red-colored test line, which results from the trapping of the gold nanoprobes at the test line region (Figure 1.2). Alternatively, a negative result is indicated by the absence of a test line as the gold nanoprobes will not become trapped at the test line region. When the nanoprobes pass the control line region, they will bind to the immobilized secondary antibodies and will also produce a visible control line. The control line is necessary to verify that the fluid and the gold nanoprobes have indeed flowed up the strip.

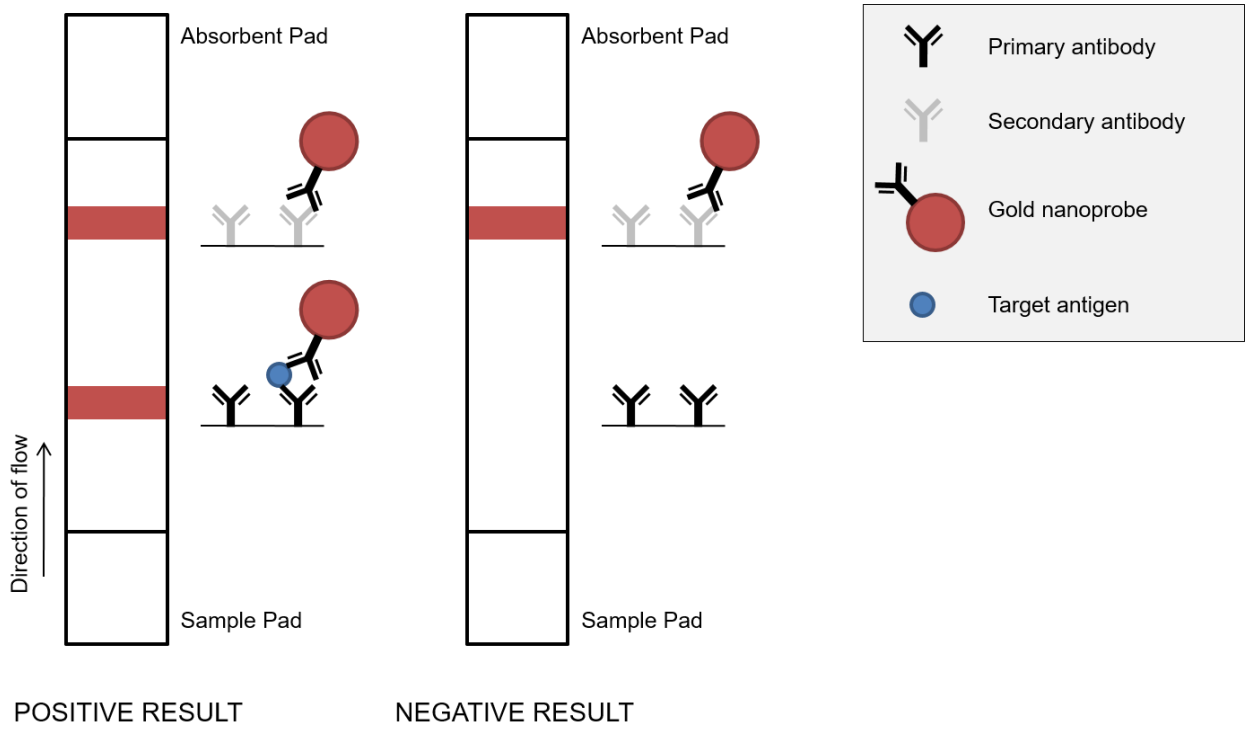

Figure 1.2 Schematic of positive and negative results for the sandwich LFA format.

Competitive formats are typically used to detect small molecules or molecules with a single antigenic site, which cannot bind to two antibodies simultaneously. In this format, the target itself, or a portion of the target (such as a nontoxic chain of a toxin molecule), is immobilized to the test line region of the nitrocellulose membrane. Primary antibodies that are specific for the target are conjugated to the gold nanoprobes, and secondary antibodies that are specific to the primary antibody are immobilized on the control line. If the sample contains enough target molecules to saturate the target-specific antibodies on the gold nanoprobes, the nanoprobes will be unable to bind to the immobilized target on the test line and will bypass the test line altogether (Figure 1.3). Thus, the absence of an apparent test line indicates a positive result. If the sample does not contain enough of the target, the gold nanoprobes will contain some unsaturated antibodies. These antibodies will instead bind to the immobilized target on the test

line, and form a visible test line indicating a negative result. A control line should still be visible to indicate a valid test, irrespective of the result on the test line.

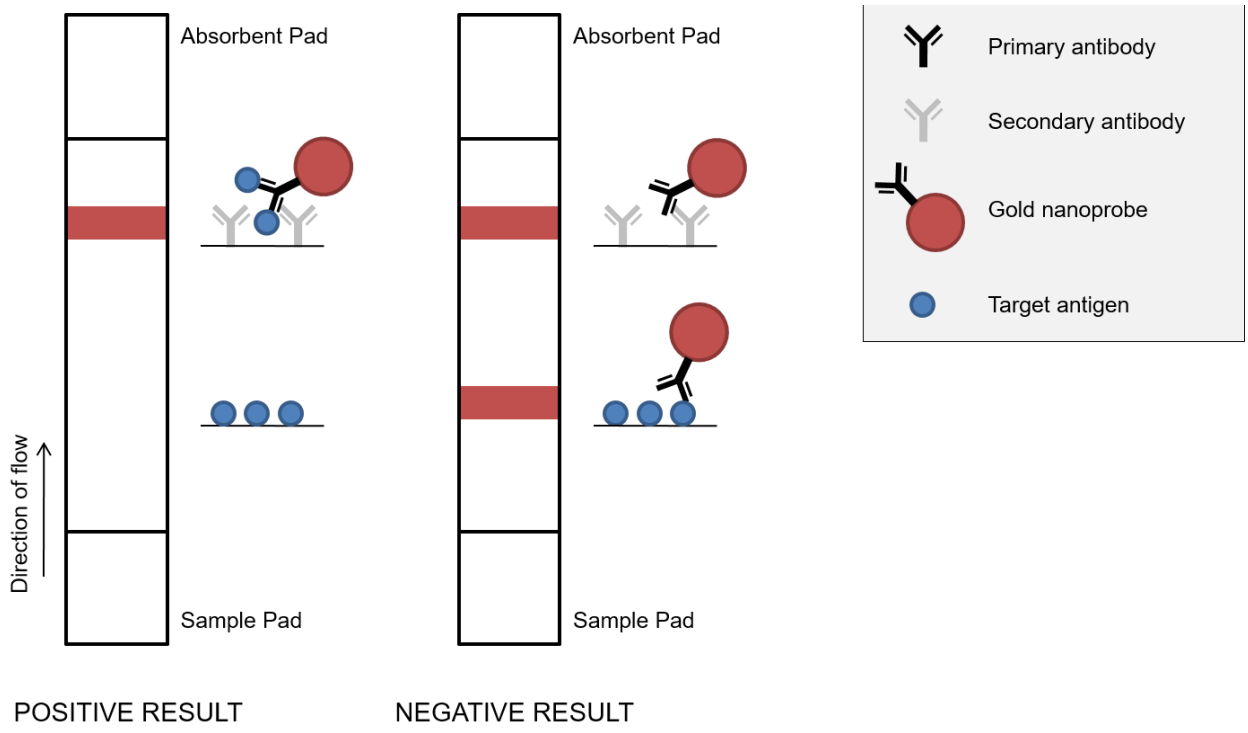

Figure 1.3 Schematic of positive and negative results for the competitive LFA format.

The fact that the LFA requires small sample volumes, requires minimal power and equipment, and yields rapid results makes it an attractive option as a POC assay that fulfills many ASSURED criteria. However, the LFA has been known to demonstrate limited sensitivity when compared to more sophisticated laboratory-based assays. While it has embraced commercial success in the form of pregnancy tests, this is largely due to the high concentrations of hCG that are present in women at the onset of pregnancy [7]. The LFA has demonstrated market potential in disease diagnosis, as well as food safety, environmental monitoring, and military and biodefense [4]. However, the inability to reliably detect biomarkers in low concentrations has limited the widespread use of the LFA in these segments. Several methods have been proposed to improve LFA sensitivity, which is linked to a decrease in the detection

limit. Some of these methods include the use of fluorescent particles and signal amplification [8–10]; however, another method is to concentrate the biomarker target prior to its application to the LFA test.

1.2 Overview of Aqueous Two-Phase Systems (ATPSs)

1.2.1 Types of Two-Phase Systems

Aqueous two-phase systems (ATPSs) are biphasic systems that have been extensively used for the separation of cells, membranes, viruses, proteins, nucleic acids, and other biomolecules. These systems are used in a liquid-liquid extraction format and can be easily scalable and require minimal equipment compared to other molecule concentrating methods such as pellet-based and membrane-based centrifugation [11]. Since both phases of an ATPS are predominantly comprised of water, they provide a milder environment for biomolecules than conventional oil-water systems. The separation of polymer or micellar solutions into two phases occurs under a variety of conditions, depending on the number and chemical nature of the components.

Three of the most common types of ATPSs include polymer-polymer, polymer-salt, and micelle-based systems. One common polymer-salt system is the polyethylene glycol (PEG) and phosphate salt system. In the PEG-phosphate salt system, phase separation can be induced when the phosphate salt concentration is above a critical value. From a mechanistic viewpoint, the addition of phosphate salt ions act to disrupt hydrogen bonds between water molecules and PEG polymers [12,13]. As these bonds are disrupted, nearby PEG polymers are allowed to approach each other and experience greater attractive van der Waals interactions. These interactions between PEG polymers become more favorable while the interactions between PEG and water become less favorable. Pockets of polymer-rich domains and salt-rich domains are then formed

in solution, which continue to coalesce over time. As these domains become larger in size, they migrate according to their relative densities. Since the salt-rich domains tend to be more dense, they move downward relative to the PEG-rich domains. This ultimately results in the formation of a top PEG-rich phase and a bottom salt-rich phase.

Micellar ATPSs are composed mainly of water and surfactants. In this thesis, the phase separation of solutions containing the nonionic surfactant Triton X-114 was investigated. At concentrations above the critical micelle concentration (CMC), the Triton X-114 molecules self-assemble to form micelles. In these micelles, the hydrophobic tails assemble in the center to minimize contact with water, and the hydrophilic heads align at the micelle surface to maximize their interactions with water. The Triton X-114 ATPS exhibits a homogenous, isotropic phase at low temperatures. At temperatures above a certain critical point, the solution undergoes macroscopic phase separation to yield a top, micelle-poor phase and a bottom, micelle-rich phase. The phase separation mechanism has some similarities with that of the PEG-salt system. In this case, hydrogen bonds between water molecules and the hydrophilic heads of the micelles are weakened with an increase in temperature. The interactions between the micelles and water molecules become less favorable, and the interactions between micelles become more favorable due to their increased van der Waals interactions as they approach each other. This allows the formation of micelle-rich domains and micelle-poor domains, which also coalesce with their respective domains and move according to density differences.

Generally, an ATPS will arise only when the phase system components are present in a certain range of proportions. The concentrations at which phase separation will occur are represented in a phase diagram. Figure 1.4 shows an example phase diagram for a PEG-salt system in water. The curved line is called the *bimodal or coexistence curve*, and it delineates the

two-phase region (above the binodal) from the one-phase, homogeneous region (below the binodal). Pairs of points that lie on the binodal are called *nodes*, and the lines joining them are called *tie lines*. These tie lines vary in length and provide information on the final component concentrations in each phase, as well as the volume ratio of the resulting solution. This volume ratio is generally defined as a ratio between the volume of the top phase and the volume of the bottom phase, and varies depending on the position of the specific condition on the tie line. For example, a condition at point A will produce two phases equal in volume (1:1 ratio), whereas a condition at point B will produce a large PEG-rich phase relative to the salt-rich phase. Point C dictates the *critical point*. At the critical point, the concentrations and the volumes of the two phases become nearly equal. Phase diagrams are generally empirically developed, but provide a valuable means of predicting the characteristics of a system from specific initial conditions.

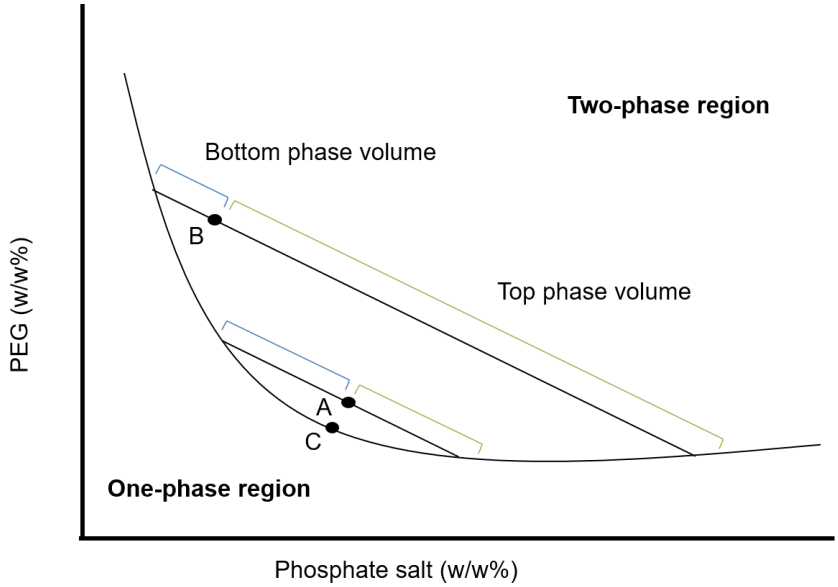

Figure 1.4 A generic phase diagram for a PEG-phosphate salt system. Point A represents a two-phase system with equal volumes of phases. Point B represents a two-phase system with a large top phase volume and a small bottom phase volume. The relative volumes of the two phases can be predicted from the length of the tie line on either side of the system's initial condition. The relative bottom phase volume is highlighted with the blue bracket, while the relative top phase volume is highlighted with a green bracket. Note that point B lies on a different tie line than point A. Point C represents the critical point.

1.2.2 The Time of Phase Separation

The time required for the phases of a two-phase system to separate can greatly vary depending on the system (Table 1.2). The primary factors that determine this time include the difference in density between the two phases, their interfacial tension, their viscosities, the time required for small droplets to form and coalesce, and the resulting volume ratio of the two phases [14]. Generally, if the more viscous phase is larger in volume relative to the other, then the separation and settling time tends to be longer than if the less viscous volume is larger in volume. This is possibly due to the greater drag force on the microdomains of the smaller phase as they try to coalesce and move to their respective macroscopic phase.

Table 1.2 Approximate phase separation times of extreme volume ratios in various two-phase systems.

Phase system	Times
Polyethylene glycol – dextran sulfate	1 hour [14]
Polyethylene glycol – phosphate salt	1-2 hours*
Polyethylene glycol – dextran	1-2 hours*
Triton X-114 micellar	8 hours*
Dextran – methylcellulose	12 hours [14]

*experimentally determined by our research group

The phase separation is also described as dependent on the tie line length (TLL) on the phase diagram. According to Albertsson, at a condition that is close to the critical point (a short TLL), the small density difference and small interfacial tension between the two phases results in an increase in settling time [14]. Moving away from the critical point, as the TLL increases, faster settling times are observed due to increases in the density difference and interfacial tension. However, at conditions that are considerably far away from the critical point (a very long TLL), the polymer concentration and viscosity become large enough that it can lead to a longer settling time. Studies by Asenjo and coworkers modeled the phase separation rate of PEG-salt systems as a function of the viscosity of the dominant phase, the interfacial tension, and

the density difference between the two phases [15]. According to their models, the solutions with a dominant salt-rich phase (in which the salt-rich phase produced the larger relative volume after separation) were able to separate faster, mostly due to an increased difference in density. In cases when the top PEG phase is the dominant phase, the density difference still plays a role, but it needs to compete with the effect of the increased viscosity attributed to the PEG polymers. This results in a slight decrease in the phase settling time.

1.3 Applying Aqueous Two-Phase Systems in Diagnostics

The combination of ATPSs with the LFA was first developed by our group, and in the area of paper-based diagnostics, this integration represents our lab's significant contribution to this emerging field. The use of the Triton X-114 micellar ATPS was initially used to concentrate bacteriophage M13 (M13), a model virus that is similar in size to the Ebola virus [16]. The large M13 bacteriophage was shown to partition extremely to the bottom micelle-poor phase due to the repulsive, steric and excluded-volume interactions between the virus and the Triton X-114 micelles. Models of partitioning and concentration factor show that the extent of concentration could be manipulated simply by varying the ATPS volume ratio. For example, a concentration factor of 10 was achieved by using a 1:9 volume ratio to produce a top phase that was one-tenth the total volume. As predicted, this 10-fold pre-concentration translated to a 10-fold improvement in the LFA detection limit for M13.

The Triton X-114 micellar system was also used to concentrate a model protein transferrin (Tf) [17]. In this case, the smaller Tf did not experience enough repulsive excluded-volume interactions to experience extreme partitioning behavior to one of the two phases. To address this issue, the gold nanoprobes used as colorimetric indicators for the LFA were injected into the mixed ATPS solution. The gold nanoprobes were approximately 20 nm in diameter, and

therefore, experienced a greater excluded-volume effect and partitioned to the top micelle-poor phase after capturing the target in solution. In this case, the target protein was concentrated 10-fold by concentrating the nanoprobes used to capture them. This "fishing" technique also resulted in a 10-fold improvement in the LFA detection limit for Tf.

This proof-of-concept approach has been extended to the PEG-phosphate salt ATPS, which has a shorter phase separation time. This system was used to concentrate M13 and transferrin in a predictable manner, which also led to improvements in their detection limits when applied to LFA [18,19]. Overall, our group was able to utilize various ATPSs to concentrate proteins and viruses. This additional concentration step provided a means of significantly improving the detection limit of LFAs in a relatively simple and user-friendly manner. This two-step method can be improved however. Implementing the ATPS will result in an increased overall assay time, as the solutions must be given time to phase separate. Depending on the ATPS that is used, this step can be the bottleneck in time that may render the test impractical. Furthermore, the phase containing the concentrated biomarker must be extracted and applied to the LFA strip. This step is subject to variability if the assay user is not properly trained in the extraction technique.

1.4 Simultaneous ATPS-Based Concentration and LFA-Based Detection in a Paper Device

More recently, our group achieved a significant reduction in the macroscopic phase separation time of a PEG-phosphate salt ATPS by applying it directly to a paper-based device [20]. Rather than applying the concentrated sample after phase separation is completed, this approach enables the direct addition of a sample that has been mixed with the PEG and phosphate salt components directly into a fiberglass membrane. Through this newly discovered

phenomenon, a well-mixed homogenous solution was shown to rapidly separate into its two phases as it flowed through the paper membrane, allowing for paper-based concentration of biomolecules in a predictive manner. To our knowledge, this was the first time that a paper membrane was used to facilitate the phase separation of an aqueous two-phase system.

The addition of ATPS to paper was particularly helpful in our diagnostic application of ATPSs. First, it significantly shortened the phase separation time for the PEG-salt system. Also, the salt-rich phase containing the target of interest was found to flow first at the fluid front, so the setup could be linked directly to an LFA strip and an intermediate phase extraction step was no longer necessary. These two factors shortened the overall assay time, allowing for a complete result within 22 min of the start of the test. To further capitalize on the phenomenon, the paper device was expanded vertically to increase the cross-sectional area of flow and exploit potential gravitational effects on the macroscopic phase separation process. By adding this 3-D component, our group achieved paper-based phase separation of solutions designed to produce 9:1 volume ratios in tubes. Accordingly, the salt-rich phase was sent to a small region in the fluid front and the partitioned target was seen to be more concentrated within the paper membrane (Figure 1.5). When the integrated system was used to detect transferrin, it still demonstrated a 10-fold improvement in detection limit, indicating that addition of the ATPS onto paper resulted in no sacrifices in sensitivity.

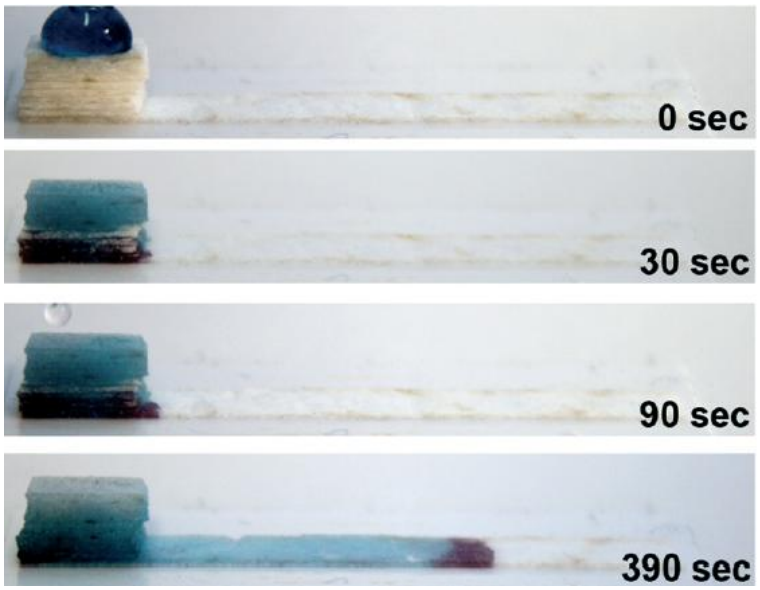

Figure 1.5 A PEG-salt solution was seen to phase separate in a 3-D paper architecture.

Our lab's work in combining LFA with ATPS represents a novel contribution to this field of paper-based diagnostics that recently has had other advances in concentrating molecules [21,22] and improving analytical detection [23–28].

1.5 Concluding Remarks and Thesis Overview

The mechanism of paper-based ATPS phase separation and how it can enhance the phase separation rates are still largely unexplored. Therefore, this thesis aims to further extend the phenomenon to a wider variety of systems and to start investigating ways that this phenomenon can be modeled so that it can be better incorporated into device designs and applications in the future. Since the PEG-salt system phase separates relatively fast compared to most aqueous two-phase systems, we investigated the Triton X-114 micellar system and its potential for phase separation in paper, as this system is one of the slowest phase separating systems. We then aimed to further simplify the ATPS-LFA design to eliminate user steps completely. To achieve this, we investigated dehydrating the phase forming components directly into the paper matrix and using the sample fluid to sequentially rehydrate the components to promote phase separation. These

techniques were all coupled with the LFA to detect appropriate biomarkers for infectious diseases. Throughout this process, we aimed to detect relevant disease biomarkers for malaria and chlamydia, and aimed to detect these biomarkers in complex fluids such as serum. Furthermore, we investigated the use of the Washburn equation as a mathematical framework to describe the flow behavior of ATPS phases within porous media, and used the framework to predict phase separation of various two-phase systems within paper, and for the first time, within hydrogels.

Chapter 2. Paper-Based Triton X-114 Micellar ATPS for Malaria Detection

2.1 Introduction

2.1.1 Malaria Background

An estimated 627,000 malaria-related deaths occurred in 2012, most of which were young children in sub-Saharan Africa [1]. In these areas, malaria is the leading cause of illness and death. The disease is caused by *Plasmodium* parasites that are transmitted to humans through infected *Anopheles* mosquitoes. There are four main parasite species that cause malaria in humans: *Plasmodium falciparum*, *Plasmodium vivax*, *Plasmodium malariae*, and *Plasmodium ovale*. Malaria caused by *P. falciparum* is the most common and the most deadly. Although artemisinin-based treatment options exist, the key to effective management of malaria is early and accurate diagnosis, which is extremely difficult to obtain in rural clinics that do not have adequate access to power, laboratory equipment, or basic health care infrastructure.

2.1.2 Methods of Detecting Malaria

The current gold standard diagnosis method is the detection of malaria parasites from a drop of patient's blood under a microscope, spread out as a "blood smear" on the microscope slide. Giemsa stains are commonly used to visualize parasite-infected cells. However, this method depends on the availability and quality of reagents and equipment, as well as on the expertise of the technician. PCR may be used to detect parasite nucleic acids, and may provide greater sensitivity than microscopy. However, PCR has seen limited use in clinics primarily because results are not available quickly enough to be of value in the diagnosis. In addition, in rural areas, clinics lack access to microscopes and PCR equipment, so there is a critical need for

accurate, inexpensive, and user-friendly tests that can be used in areas where these technologies are logistically impractical.

Rapid diagnostic tests (RDTs) are designed to provide a useful alternative to microscopy in situations when microscopy is not an option. These RDTs tend to detect parasite biomarkers rather than the parasite itself. The most common biomarkers include the histidine-rich protein-2 (HRP-2), *Plasmodium* lactate dehydrogenase (pLDH), and *Plasmodium* aldolase (pAldo). HRP-2 is a histidine- and alanine-rich, water-soluble protein that is expressed only in *P. falciparum* species. In addition, these antigens persist for about two weeks in the circulating blood after the parasitaemia has cleared, which may compromise their value in follow-up tests for active infection [29–31]. On the other hand, pLDH does not persist in the blood after treatment. Furthermore, it is expressed not only by *P. falciparum*, but also by *P. vivax*, *P. malariae*, and *P. ovale*. These differences suggest that RDTs will also differ in their detection capabilities depending on their target of interest.

Currently, there are several commercially available malaria RDTs that target one or multiple biomarkers. These RDTs have been tested in laboratory settings as well as in the field, and the reports of sensitivity have been mixed. For example, the BinaxNOW Malaria Test from Alere Inc. (the first FDA-approved RDT for malaria in 2007) was shown to have sensitivities ranging from 72.2% to 84.2% in laboratory settings [32,33]. However, as it only detects HRP-2, reported sensitivities dropped significantly when testing for non-falciparum species [34]. Recent RDTs have been designed to detect multiple species in a single test by detecting both HRP-2 and pLDH, or various classes of pLDH. These include the First Response Malaria Ag Combo RDT (Premier Medical Corporation Ltd) and the Carestart Malaria pLDH RDT (Access Bio, Inc.).

Quality testing of these products has generated sensitivities between 74.3% and 91.4% [35,36], indicating that these tests are also subject to variability.

2.1.3 Applying the Triton X-114 Micellar ATPS to Paper

As previously mentioned, our group achieved a significant reduction in the macroscopic phase separation time of a PEG-phosphate salt ATPS by applying it directly to a paper-based device [20]. Phase separation was reduced from about one hour to only 6.5 min. On the other hand, the Triton X-114 micellar system phase separates much more slowly than the PEG-phosphate salt ATPS. In fact, it would take at least 8 hours for a 1:9 volume ratio (top micelle-poor phase to bottom micelle-rich phase) to establish phase separation equilibrium in test tubes, which is not acceptable for POC applications. Here, we designed a novel paper-based setup, which also incorporated 3-D architecture, and used it to enhance the phase separation time of the Triton X-114 ATPS. By doing so, we demonstrated the capacity of paper membranes to accelerate multiple types of ATPSs, including one of the slowest-forming known types. We also integrated the 3-D paper setup to the LFA and used it to concentrate and detect malaria pLDH in samples of PBS. Finally, we repeated the detection of pLDH in solutions of serum (fetal bovine serum) to more closely mimic complex sample media, and determined the improvements in assay time and detection limit over a conventional LFA setup.

2.2 Materials and Methods

2.2.1 Preparing Gold Nanoprobes (anti-pLDH GNPs)

The gold nanoparticles were prepared according to Frens and coworkers with slight modifications [37]. Using this method, a solution of gold nanoparticles with an average hydrodynamic diameter of 24 nm was obtained, which appeared as a dark cherry-colored solution. The size of the gold nanoparticles was obtained by dynamic light scattering

measurements using a Zetasizer Nano ZS particle analyzer (Malvern Instruments Inc, Westborough, Massachusetts).

After forming the nanoparticles, the pH of a 1 mL gold nanoparticle solution was first adjusted to pH 9 using 1.5 N NaOH. Subsequently, 16 µL of mouse monoclonal anti-*P.falciparum/P. vivax* LDH antibodies (BBI Solutions, Cardiff, UK) at a concentration of 0.5mg/mL were added to the colloidal gold solution and mixed for 30 min on a shaker. To prevent nonspecific binding of other proteins to the surfaces of the colloidal gold nanoparticles, 200 µL of a 10% w/v bovine serum albumin (BSA) solution were added to the mixture and mixed for 20 min on a shaker. To remove free, unbound antibodies, the mixture was then centrifuged for 30 min at 4 ℃ and 12,000 rpm, followed by resuspending the pellet of colloidal gold nanoparticles in 200 µL of a 1% w/v BSA solution. The centrifugation and resuspension steps were repeated two more times, and after the third centrifugation, the pellet of gold nanoparticles was resuspended in 100 µL of 0.1 M sodium borate buffer at pH 9.0. The gold nanoparticles functionalized with anti-pLDH antibodies will henceforth be referred to as anti-pLDH gold nanoprobes (anti-pLDH GNPs). The BSA-coated gold nanoparticles not functionalized with antibodies were used for visualization purposes and will henceforth be referred to as BSA-GNs.

2.2.2 Preparation and Visualization of Triton X-114 ATPS

Equilibrium volume ratios (the volume of the top phase divided by the volume of the bottom phase) of the Triton X-114 ATPS were found by varying the initial w/w concentration of Triton X-114 (Sigma-Aldrich, St. Louis, MO) in solutions of Dulbecco's phosphate-buffered saline (PBS; Invitrogen, Grand Island, NY, pH 7.4, containing 1.47 mM KH_2PO_4, 8.1 mM Na_2HPO_4, 137.92 mM NaCl, 2.67 mM KCl, and 0.49 mM $MgCl_2$) and FBS (Invitrogen, Grand

Island, NY). These solutions were allowed to phase separate and reach equilibrium at 25 ℃ in a temperature-controlled water bath. BSA-GNs in Triton X-114/PBS solutions exhibited favorable partitioning to the top phase, while BSA-GNs in Triton X-114/FBS solutions partitioned favorably to the bottom phase. Consequently, the conditions for a 1:9 volume ratio (*i.e.*, volume of the top phase divided by that of the bottom) for Triton X-114/PBS and a 9:1 volume ratio in Triton X-114/FBS were found and used for further experiments. These volume ratios allowed for a 10-fold concentration of the nanoparticles.

In order to visualize the two phases of the micellar ATPS in PBS, 100 μL of BSA-GNs and 4 μL of Brilliant Blue FCF dye (The Kroger Co., Cincinnati, OH) were added to 2.5 g solutions containing the previously determined concentration of Triton X-114 for a 1:9 volume ratio in PBS. These solutions were well-mixed through vortexing and incubated at 25 ℃. Pictures of the solutions were taken hourly until reaching equilibrium at 8 hrs. Equilibrium was established when the solution lost its cloudy appearance, all visible domains moved to their respective phases, and the measured interface height remained stable. The cherry-colored BSA-GNs and blue-colored dye were colorimetric indicators of the micelle-poor phase and micelle-rich phase, respectively. All images were captured using a Canon EOS 1000D camera (Canon U.S.A., Inc., Lake Success, NY) in a controlled lighting environment.

To visualize the phase separation of the micellar ATPS in PBS within the 3-D paper wick, 200 mg of a mixed, homogeneous solution containing 2 μL of Brilliant Blue FCF dye and 10 μL of BSA-GNs were vortexed and subsequently placed in a water bath at 25 ℃. The 3-D paper wick was formed by stacking three 5 × 15 mm fiberglass paper sheets on one edge of a 5 × 40 mm strip of fiberglass. After the prepared solution was incubated at 25 ℃ for 5 min, the 3-D

paper wick was placed vertically in the solution, allowing the paper stack to absorb the solution. Images of the paper strip were captured at 0, 30, 60, and 180 s.

2.2.3 Detection of pLDH with LFA Only

LFA test strips utilizing the competitive assay format were assembled in a similar manner to our previous studies [17]. In this format, immobilized *P. falciparum* L-lactate dehydrogenase (pLDH; My BioSource, San Diego, CA, USA) constituted the test line and immobilized goat anti-mouse IgG secondary antibodies (Bethyl Laboratories, Montgomery, TX) specific to the primary anti-pLDH antibody constituted the control line. If enough pLDH is present to saturate the GNPs in a sample, the pLDH-GNP complexes moving through the LFA strip will not bind to the immobilized pLDH on the test line, resulting in the absence of a visible colored band at the test line. If pLDH is not present, unoccupied antibodies on the GNPs will bind the immobilized pLDH, and a colored band will form at the test line region. Regardless of the presence of pLDH, the antibodies on the GNPs will bind the secondary antibodies immobilized at the control line and form a visible line, indicating successful sample flow through the strip. Therefore, a negative result is identified by two colored bands (one test line and one control line), while a positive result is identified by one colored band only at the control line.

To verify the detection limit of pLDH with LFA only, anti-pLDH GNPs were added to a sample solution and allowed to bind pLDH present in the sample to form pLDH-GNP complexes. 20 µL of sample solution, consisting of 10 µL of anti-pLDH GNPs and 10 µL of a known concentration of pLDH in either PBS or FBS, were mixed with 30 µL of running buffer (0.2% BSA, 0.3% polyoxyethylenesorbitan monolaurate (Tween 20), 0.1 M Tris buffer, pH 8) in a test tube. The LFA test strip was inserted vertically into the sample solution, which wicked through the strip via capillary action upward towards the absorbance pad. Images of the test

strips from both PBS and FBS samples were taken after 20 min in a controlled lighting environment.

2.2.4 Detection of pLDH with 3-D Paper-Based ATPS and LFA

The design of the LFA test strip was slightly modified with the addition of the 3-D paper wick. Specifically, the cellulose sample pad that connected to the nitrocellulose membrane was replaced with a 5 × 20 mm fiberglass pad. On top of this fiberglass pad, three additional strips of 5 × 15 mm fiberglass sheets were stacked to form a total of four layers of fiberglass paper. The fiberglass layers were tightly wrapped with Scotch tape adhesive (3M, St. Paul, MN, USA).

For detection of pLDH in PBS samples, 200 µL of a well-mixed 1:9 volume ratio ATPS containing 10 µL of anti-pLDH GNPs and a known concentration of pLDH were added into a test tube. The solution was incubated for 5 min at 25 ℃ to ensure the solution became turbid, indicating the onset of phase separation, and to allow the GNPs to capture the pLDH in solution. The 3-D wick-modified LFA strip was then placed in the mixed ATPS, and the fluid was allowed to pass through the 3-D wick towards the absorbent pad. Images of the resulting detection region were captured after 20 min.

The detection of pLDH in FBS samples followed a very similar protocol, with the exception that 200 µL of a mixed 9:1 volume ratio ATPS were prepared instead. Test conditions, including incubation times and times for the lines to develop, were consistent with those for PBS samples. Images of the detection region were also captured after 20 min.

2.2.5 Quantitative Analysis of LFA

The images of the LFA strips that were taken after 20 min were processed using a custom MATLAB script. To quantify the LFA results, the images were converted to 8-bit grayscale

matrices, which were then split in half so that the intensities of the control line and the test line could be analyzed separately. The location of the control or test line in each half matrix was then found by locating the darkest spot, or minimum intensity, detected by vectors perpendicular to the lines. The average grayscale intensities of a 15 pixel-high rectangular region centered at the average location of these minima and spanning the length of each line were denoted as I_{test} or $I_{control}$. The mean grayscale intensity of a reference region, denoted as $I_{reference}$, was used to normalize the intensities of the test and control lines by removing the effect of background color. This reference region was set to be 15 pixels wide and 50 pixels upstream of the test line. The signals of the control and test lines, respectively, are represented by the following equations:

$$Signal_{control} \equiv I_{reference} - I_{control}$$

$$Signal_{test} \equiv I_{reference} - I_{test}$$

The resulting signal values were then converted such that high values correlated to dark regions on the strip. High signal values thus indicated that a strong line appeared on the LFA strip, while low values indicated that either a weak line appeared or no line appeared at all.

2.3 Results and Discussion

2.3.1 Triton X-114 ATPS Phase Separation in the Test Tube

In solutions of PBS above a certain temperature, the Triton X-114 micellar ATPS forms a top, micelle-poor phase and a bottom, micelle-rich phase [38]. Molecules present in solution partition between the two phases based on their physical and chemical characteristics, such as hydrophobicity and size. It was previously shown that hydrophilic BSA-GNs partitioned extremely into the micelle-poor phase, driven in large part by repulsive, steric, excluded-volume interactions between the nanoparticles and the larger and more abundant micelles in the micelle-rich phase [17,20]. Nanoparticles functionalized with specific antibodies can form complexes

with a target molecule, and these complexes will also partition extremely to the micelle-poor phase. Nonfunctionalized BSA-GNs, which appear cherry-colored due to surface plasmon resonance, [39,40] were used to visualize the resulting micelle-poor phase after phase separation. In contrast, Brilliant Blue FCF dye is small and hydrophobic, and therefore, it partitioned extremely to the micelle-rich phase. When added into a mixed ATPS solution, the blue-colored dye was used to visualize the resulting micelle-rich phase after phase separation.

The time required to achieve phase separation varies among different two-phase systems. For example, while the PEG-phosphate salt ATPS phase separates quickly relative to most two-phase systems, the Triton X-114 micellar ATPS requires a significantly longer amount of time to achieve macroscopic phase separation equilibrium due to the small density difference and interfacial tension between the two phases. The phase separation time also increases with more extreme volume ratios, such as 1:9 or 9:1, because one phase becomes proportionately much smaller, and the microscopic domains of that phase experience difficulty coalescing. Images of the 1:9 volume ratio ATPS in PBS were taken at specific time points at 25 ℃; complete macroscopic phase separation equilibrium was not achieved until after approximately 8 hrs (Figure 2.1a). The resulting micelle-poor phase volume was measured to be one-tenth of the total solution volume, verifying a 1:9 volume ratio.

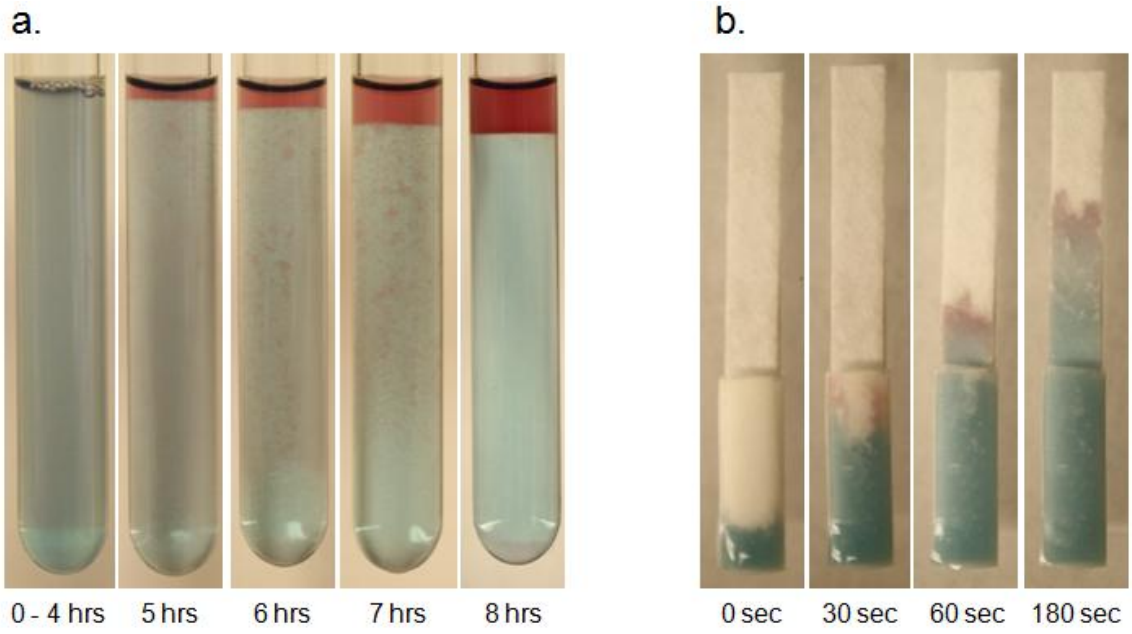

Figure 2.1 Comparison of the times required to achieve phase separation for a 1:9 volume ratio Triton X-114 system in PBS. Brilliant Blue FCF dye and cherry-colored BSA-GNs were the colorimetric indicators for the bottom, micelle-rich and top, micelle-poor phases, respectively. (a) At 25℃, the Triton X-114 ATPS achieved macroscopic phase separation equilibrium in 8 hrs in a test tube. (b) When the 3-D paper wick was applied to the mixed ATPS, phase separation was already observed within the wick at 30 s, as the micelle-rich domains were retained near the bottom of the wick and the micelle-poor domains were able to flow up the wick more freely. Upon exiting the wick, the distinct phases remained separated from each other, and the micelle-poor phase remained concentrated within a small volume at the leading front, indicating a more complete separation at 180 s (3 min).

2.3.2 Using Paper Membranes to Enhance Triton X-114 ATPS Phase Separation

Previously, our group utilized a 3-D architecture to significantly decrease the phase separation time of the PEG-phosphate salt ATPS within paper membranes [20]. We hypothesized that the multiple layers of paper is an essential factor for enhancing the phase separation in paper. Thus, in a similar manner, a "3-D paper wick" consisting of multiple layers of thin, tightly-bound paper strips was designed to increase the phase separation process of the Triton X-114 ATPS. When the 3-D wick was placed upright into a mixed ATPS solution in PBS, the solution flowed vertically up the strip. Almost immediately after the addition of the strip, the micelle-poor phase containing GNPs quickly flowed ahead of the slower-moving micelle-rich phase containing the blue-colored dye (Figure 2.1b). Note that the separation is already observed

within the 3-D wick portion of the strip after approximately 30 s, with more complete separation seen at 180 s (3 min) after the fluid has already exited the wick.

These experiments support our hypothesis that the additional layers of the wick provide increased cross-sectional area normal to the direction of flow to aid in the coalescence of the microscopic phase domains and allow a greater volume to wick through the paper in a given time. Moreover, the less viscous micelle-poor domains are expected to move ahead more quickly in the porous paper and coalesce, while the micelle-rich domains are expected to be held back and move more slowly due to their greater viscosity and potential favorable interactions with the paper material. As a result, macroscopic separation of the two phases, shown to occur on the order of hours in a test tube, is witnessed within only a matter of minutes in the paper membrane. An additional benefit of the 3-D paper wick is the processing of larger volumes of ATPS solutions. Generally, the number of layers in the 3-D wick was increased to accommodate solutions of larger volume. Factors that were optimized in the final design included strip length, width, and number of strips. The optimal design was able to achieve complete phase separation over the length of the wick, and minimize the distance required for the separated micelle-poor phase to travel in order to exit the wick. To our knowledge, this is the first application of a paper membrane to significantly enhance the phase separation time of a micellar ATPS that naturally separates on a relatively large time scale. These paper-based architectures can potentially be used to enhance many other two-phase systems that require even longer times to separate.

2.3.3 Enhancing Triton X-114 ATPS Phase Separation in FBS

In contrast to the PBS solutions, the Triton X-114 ATPS formed in FBS samples instead produced a top, micelle-rich phase and a bottom, micelle-poor phase. This is likely due to the density difference caused by additional proteins and salts found in FBS, as was seen in other

Triton X-114 phase extraction experiments from complex fluids [41]. Since the GNPs instead partitioned extremely to the bottom phase, it was then necessary to adjust the initial Triton X-114 concentration to produce a concentrated bottom phase with one-tenth of the total volume, or in other words, a 9:1 volume ratio.

Since the orientation of the two phases is reversed in serum, we wanted to determine how the reversed orientation may affect the phase separation in the 3-D paper wick. In fact, when the 3-D wick was placed in a mixed ATPS in FBS, we observed results very similar to those of the PBS experiments. Accordingly, although the density difference drives the micelle-poor phase in FBS to the bottom in a test tube, the micelle-poor phase still remains the faster phase to flow up the 3-D wick. The micelle-poor phase is therefore the leading front irrespective of the phase orientation dictated by relative phase densities in a test tube. This further corroborated our hypothesis that the more viscous micelle-rich phase is consistently slower moving and held back by the porous membrane, indicating that viscosity effects dominate over any density effects in flow behavior of the micellar ATPS introduced to paper.

2.3.4 Improving LFA-Based Detection of pLDH in PBS

In a previous proof-of-concept study, our group utilized the Triton X-114 micellar ATPS and GNPs to concentrate the model protein transferrin by 10-fold prior to its detection by LFA, which successfully corresponded to a 10-fold improvement in the detection limit. However, the point-of-care application of this approach was limited by the long wait time needed for the two phases to macroscopically separate. In addition, the prior approach included an extraction step during which the micelle-poor phase containing concentrated GNPs bound to transferrin was withdrawn using syringe and needle sets and applied to a standard LFA strip. While our novel application of the ATPS to paper would significantly decrease the phase separation time and

address the first issue, eliminating this extraction step would also improve the ease-of-use. Since the micelle-poor phase containing concentrated GNPs flows at the leading front upon exiting the 3-D paper wick, we attached the wick upstream of the nitrocellulose-based detection region of an LFA paper strip. Doing so enables a seamless transition from the concentration step to the detection step and eliminates the need for syringe extraction. The final design for the integrated paper-based diagnostic strip is shown in Figure 2.2a. The 3-D wick (the concentration zone) consisting of multiple layers of fiberglass paper strips is connected to a nitrocellulose membrane with immobilized control and test lines (the detection zone), which is then connected to an absorbent pad used as a sink to drive fluid flow. All the components are secured on an adhesive backing, and the 3-D wick is dipped vertically in a turbid ATPS solution.

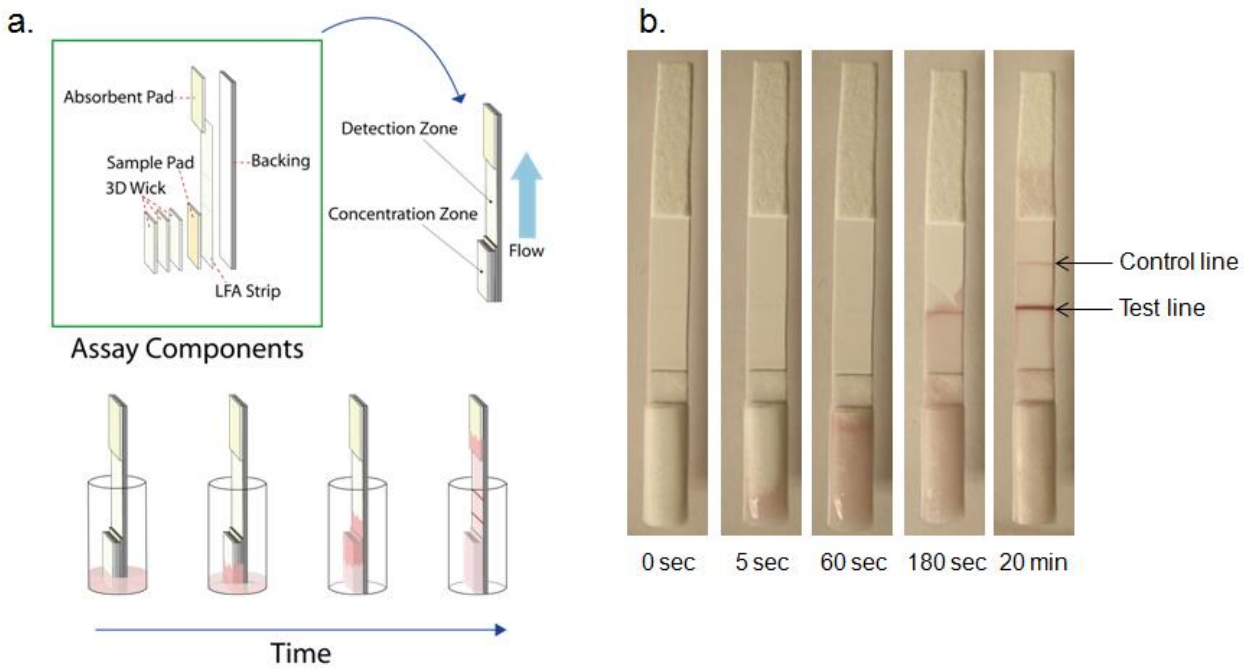

Figure 2.2 Integrating the paper wick and Triton X-114 micellar ATPS with LFA. (a) The integrated diagnostic strip consists of a concentration zone in which phase separation occurs, followed by a detection zone containing the immobilized test and control line components. (b). A true negative test was confirmed within 20 min when analyzing a solution containing no pLDH.

In the pLDH detection tests, the Brilliant Blue FCF dye was no longer used, and functionalized anti-pLDH GNPs were used in place of the BSA-GNs. The anti-pLDH GNPs exhibit very similar partitioning behavior as the BSA-GNs, but will be able to capture pLDH and act as a colorimetric indicator in the LFA.

First, the detection limit for the LFA-only control, which did not incorporate the ATPS and 3-D paper wick, was identified using 20 μL of total sample volume. Since the LFA-only control was able to successfully detect pLDH at 10 ng μL^{-1} but could not successfully detect pLDH at 1 ng μL^{-1}, its detection limit was determined to be 10 ng μL^{-1}. In order to show an improvement in detection limit by detecting lower concentrations of pLDH, we exposed the same number of GNPs used in the LFA-only control to the same number of pLDH molecules by increasing the total volume of solution containing the lower concentration of pLDH. Although a volume increase would typically dilute the GNPs and lead to a reduction in the amount of GNPs entering the detection zone in a given period of time, the addition of the ATPS and 3-D wick is expected to concentrate the GNPs into a small volume at the leading front. Effectively, the GNPs are exposed to the same amount of pLDH at a lower concentration, but are then concentrated into a similar volume as that which was processed by the LFA-only control. When using a 1:9 ATPS that was expected to concentrate the GNPs by 10-fold, the total sample volume was increased 10-fold (to 200 μL) to ensure the same amount of GNPs entering the detection region when compared to the LFA-only control.

Figure 2.2b demonstrates the use of the modified LFA device in a negative control test which does not contain pLDH in solution. When the modified LFA strip was dipped into an ATPS solution containing anti-pLDH GNPs in PBS, the GNPs rapidly concentrated to the leading front of the solution in the 3-D wick segment, as evidenced by the darker red color at the

60-second mark. The solution flowed easily across the nitrocellulose membrane without the use of additional running buffers. The GNPs quickly reached the detection region while much of the solution was retained in the paper wick. Visible bands appeared at both the control and test line regions within 20 min, indicating a valid negative test.

Once a valid negative test was verified, the pLDH concentrations were varied to determine the detection limit of the integrated device in a 1:9 volume ratio solution. The results of these experiments demonstrated that while a conventional LFA detected pLDH at concentrations of 10 ng μL^{-1} (producing a true positive result), our diagnostic strip integrating the Triton X-114 ATPS and LFA was capable of detecting pLDH at 1.0 ng μL^{-1}, which is a 10-fold improvement in the detection limit (Figure 2.3).

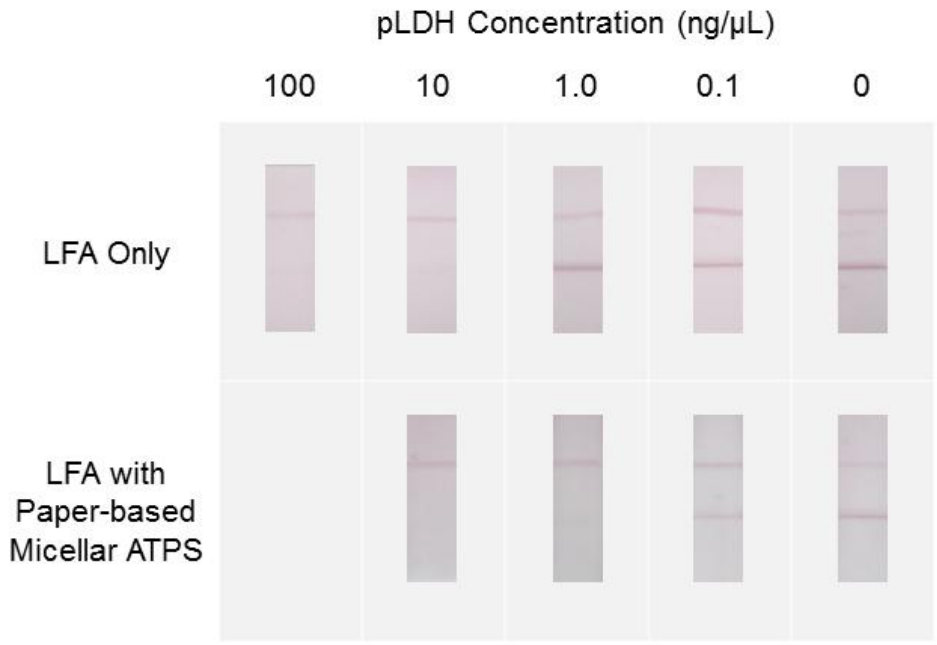

Figure 2.3 The paper-based 1:9 volume ratio ATPS achieved a 10-fold improvement in the detection limit of pLDH in PBS at 25 ℃. Standard LFA detected pLDH at 10 ng μL^{-1} but could not accurately detect pLDH at 1 ng μL^{-1}. The integrated diagnostic strip successfully detected pLDH at 1 ng μL^{-1}.

2.3.5 Improving LFA-Based Detection of pLDH in FBS

These experiments were repeated in FBS samples using the modified operating conditions to produce 9:1 volume ratios. Once more, the 3-D paper-based diagnostic device demonstrated a 10-fold detection limit improvement by successfully detecting pLDH in FBS at 1.0 ng μL^{-1}, while the LFA-only control successfully detected pLDH in FBS at 10 ng μL^{-1} but not at 1.0 ng μL^{-1} (Figure 2.4). The experiments utilizing the integrated paper-based device in FBS samples demonstrated slower fluid flow through the nitrocellulose-based detection region. This was likely due to the greater initial concentration of Triton X-114 and the presence of other serum components that increased the overall viscosity of the sample. Although control and test line signals were fully developed within 20 min (Figure 2.4), the entire micelle-poor phase flowed past the detection region only if given 10 extra min, leading to a reduction in background noise (Figure 2.5). As with the case of the above tests in PBS, all tests in FBS did not require any prior dilution in buffers, extraction steps, or running buffer additions to aid flow.

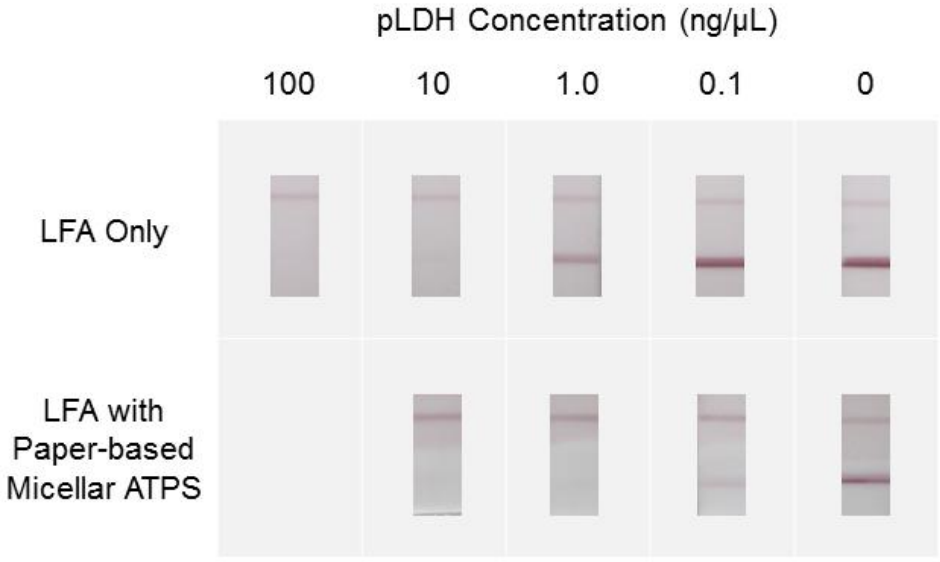

Figure 2.4 The paper-based 9:1 volume ratio ATPS achieved a 10-fold improvement in the detection limit of pLDH in undiluted FBS at 25 °C. Standard LFA detected pLDH at 10 ng μL^{-1} but could not accurately detect pLDH at 1 ng μL^{-1}. The integrated diagnostic strip successfully detected pLDH at 1 ng μL^{-1}.

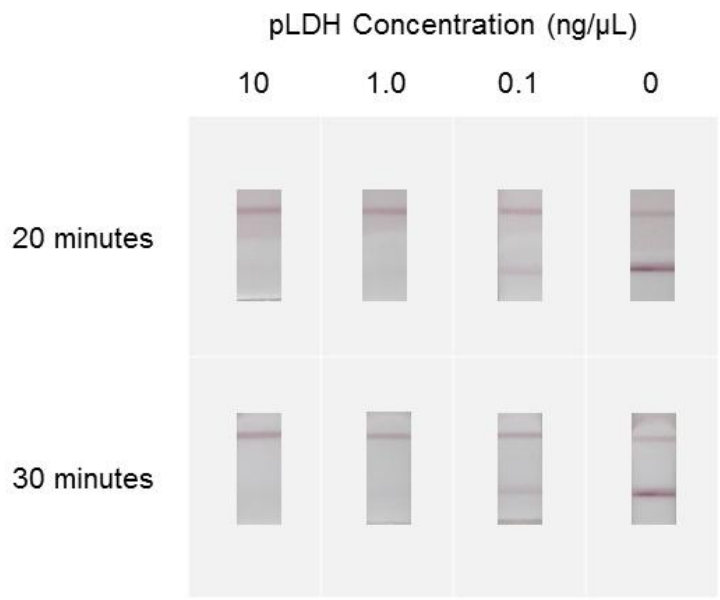

Figure 2.5 The detection of pLDH with a 9:1 ATPS and 3-D wick LFA strip. Although control and test lines develop within 20 min, the entire micelle-poor phase does not completely flow past the detection region in this time frame. This leads to increased background noise as seen by the dark red background in between the control line and test line at 20 min. If given an additional 10 min, the micelle-poor phase was able to flow completely past the detection region. Since the control and test line intensities are very similar from 20 to 30 min, we concluded that reliable results can be seen at the 20-min mark.

In order to compare the test line signal intensity between FBS and PBS runs, the ratio of the test line signals for positive samples relative to the test line signals for a negative sample in the same type of solution was found:

$$Relative\ test\ line\ signal\ \equiv \frac{Signal_{test-positive}}{Signal_{test-negative}} * 100\%$$

Relative test line signals with values less than 20% were defined as positive detection of pLDH, while relative test line signals greater than 20% indicated negative detection of pLDH. When detecting pLDH in either FBS or PBS, the use of the Triton X-114 ATPS allowed for detection of pLDH at 1 ng μL^{-1}, while the LFA-only case detected pLDH only at concentrations of 10 ng μL^{-1} or higher. This 10-fold improvement in detection limit was confirmed with our custom MATLAB script, where the relative test line signals for both the FBS and PBS cases had values

less than the 20% threshold value at 10 ng μL^{-1} for the LFA-only setup and at 1 ng μL^{-1} for the integrated LFA-ATPS system.

By demonstrating an improvement in the LFA detection of the malaria pLDH in serum, our device can potentially be used to improve the current state of malaria rapid diagnostic tests (RDTs). Despite the increasing production and use of malaria RDTs, they are in most cases required to be used in conjunction with additional methods, such as blood film microscopy, to verify results [42,43]. While the ELISA is more sensitive than many lateral-flow assays, it requires a longer assay time (several hours), laboratory equipment, and trained personnel. In contrast, lateral-flow assays (or RDTs) produce results within minutes and do not require laboratory personnel and equipment, but generally have higher, or worse, detection limits. Limited sensitivity and variations in ease-of-use are two factors that prevent the LFA from being used as a reliable stand-alone assay in remote malaria-affected settings [30]. Our integrated paper-based device has the potential to address these two concerns. A recent comparison of commercial RDTs to ELISA for pLDH detection at the same sensitivity revealed that the RDT detection limits are approximately 10-fold higher than those of ELISA [44]. Our proposed approach improves the detection limit of a conventional LFA setup by 10-fold, and therefore, has the potential to bring the pLDH detection limit of LFA much closer to that of the more sensitive ELISA. The integrated concentration component of the device allows for significant improvements in sensitivity. In addition, since many of these RDTs require dilution in a sample buffer or the use of running buffer to aid fluid flow, our diagnostic device demonstrates improvements in user-friendliness by eliminating these steps. While this approach has the potential to improve existing malaria RDTs, we envision that this platform technology can also be applied for the diagnosis of a variety of infectious diseases in resource-poor environments.

2.4 Conclusions and Discussion

In this study, we developed a 3-D paper-based diagnostic strip that utilizes the Triton X-114 micellar ATPS to concentrate and detect a malaria protein biomarker pLDH, resulting in a 10-fold detection limit improvement over LFA. Through this process, we demonstrated for the first time that a micellar ATPS can be applied directly to a fiberglass paper membrane to significantly speed up its macroscopic separation from at least 8 hrs to approximately 3 min. Although the complete mechanism for the enhanced phase separation requires further investigation, we have shown that the viscous micelle-rich phase is consistently retained near the bottom of the vertically placed strip, regardless of its orientation relative to the micelle-poor phase in a gravity-driven test tube configuration. The faster-flowing micelle-poor phase containing the dense gold nanoparticles is accordingly focused at the leading front of fluid moving through the paper strip. This phenomenon allows for the immediate concentration of pLDH in a sample as it flows to a downstream LFA component for subsequent detection. No additional buffers were needed to trigger or complete the assay, rendering the assay virtually free of user intervention after the sample is applied to the diagnostic strip. The integration of the concentration and detection steps improves the sensitivity of the conventional LFA without sacrificing its advantages in ease-of-use and time-to-result.

The robust setup easily handles undiluted serum samples, provides rapid results with minimal user intervention, and requires no electricity or complex laboratory equipment. Therefore, it is an ideal point-of-care device for the potential detection of malaria pLDH in remote resource-poor settings. Furthermore, the micellar ATPS and 3-D paper wick components form a platform technology that can be integrated with existing commercial LFA products to significantly improve their sensitivity. Once optimized, our novel approach has the potential to

enhance the detection of a variety of diseases affecting resource-poor environments, making the use of inexpensive paper-based diagnostics more reliable and widespread in these areas.

Chapter 3. Improved Lateral-Flow Immunoassay for Bacterial and Antibody Biomarkers via Sequential Rehydration of Aqueous Two-Phase Components

3.1 Introduction

Infectious diseases such as chlamydia and HIV greatly affect both developed and developing countries. Chlamydia is a sexually transmitted infection (STI) caused by the bacterium *Chlamydia trachomatis* which, if left untreated, can lead to pelvic inflammatory disease in women and cause permanent damage to the reproductive system [45]. The prevalence of chlamydia has been steadily rising in the United States since 1993, with over 1.4 million new chlamydia infections reported in 2014 [46]. Although chlamydia is relatively straightforward to treat, and shows no signs of emerging resistance to primary pharmacological treatment options [47], it is still one of the most common STIs in the United States [46]. HIV, on the other hand, is caused by the human immunodeficiency virus which attacks the body's immune system, specifically the CD4 cells. In 2015 alone, there were about 2.1 million new cases of HIV worldwide, and about 39,513 people were diagnosed with HIV in the United States [48]. One approach for addressing the increasing prevalence of chlamydia and HIV is through low-cost point-of-care (POC) screening of at-risk populations, which has shown promising results in theoretical models [49,50] and isolated trial studies [51,52].

Unfortunately, current gold standard laboratory-based diagnostics, such as ELISA tests, nucleic acid amplification tests (NAATs), or cell culture methods, are not suitable for POC screening. This is due to the high cost of equipment, the requirement for trained personnel, and the lengthy time to result. In contrast, paper-based diagnostics are a more suitable technology,

with two components that are necessary for effective large-scale screening: on-site diagnosis and treatment within the same visit, and administration by untrained or minimally trained personnel. The most commonly used paper diagnostic is the lateral-flow immunoassay (LFA), a visually interpreted antibody-based diagnostic recognized for its widespread use in pregnancy tests [53]. Unfortunately, chlamydia LFA tests are currently not sensitive enough to be effective diagnostics [54], a limitation that most paper-based diagnostics for infectious diseases suffer from [55]. Although HIV LFA tests are more established in the consumer market than chlamydia LFA tests, there is still room for their sensitivity to be improved to further minimize the risk of false negatives and potential transmission of the virus.

Significant efforts have been made to improve the sensitivity of LFAs and paper-based assays, which range in their fabrication, their choice of nanomaterials, and their use of instrumentation [56]. Some key innovations include work with two-dimensional paper networks by the Yager lab [24,25,57–60] and microfluidic paper-based analytical devices by the Whitesides lab [61–63]. The most commonly used format of the LFA utilizes gold nanoparticles as reporters that provide direct colorimetric visualization. However, these molecules are limited in their analytical sensitivity. To improve gold nanoparticle-based detection, researchers have developed systems using agglomeration bifunctional gold nanoparticles [64], dual-layered particles with signal enhancement techniques [65,66], and surface enhanced Raman scattering (SERS) detection using gold-silver core-shell nanoparticles [67]. Although these methods provide between 8 to 100-fold improvements in the limit of detection when compared to traditional LFAs, they typically require additional equipment, additional steps, or rigorous optimization of the conjugation process. An alternative approach to improve the LFA sensitivity is to concentrate the target biomarker prior to its application to the assay. Previously, our lab

developed an equipment-free method to thermodynamically pre-concentrate target analytes prior to their application to LFA tests. In short, this is accomplished by utilizing aqueous two-phase systems (ATPSs), which separate into two distinct liquid phases, where the target analyte partitions extremely into one of those phases, effectively concentrating the target. In the first approach, a 3-step diagnostic process involved (i) mixing a large volume of target solution with ATPS components, (ii) waiting for macroscopic phase separation, and (iii) extracting and applying the concentrated target phase to the LFA test. With this method, improvements in the limit of detection for both large viruses [16,19] and small protein targets [17,18] were achieved. Additionally, our lab discovered that the phase separation process is expedited when the ATPS flows through paper, reducing the overall diagnostic time from hours down to minutes by eliminating the waiting and extraction steps. The phenomenon demonstrated the ability to simultaneously concentrate and detect protein biomarkers within paper [20,68]. This diagnostic process still required an initial ATPS component mixing step prior to application of the solution to an LFA strip, which can be suitable for applications that already require initial mixing into a predetermined buffer (i.e., a swab-based diagnostic).

However, other diagnostic applications can benefit from the direct addition of a sample without additional mixing with other solutions and buffers. In this work, the authors describe a single-step ATPS paper-based diagnostic assay based on the novel concept of sequential resolubilization of ATPS components to give rise to the desired phase separation behavior within paper. This concept was demonstrated using two different polymer-salt ATPSs in two different diagnostic applications – one to detect *C. trachomatis* for a chlamydia diagnostic, and the other to detect human immunoglobulin M (IgM) in a potential HIV antibody diagnostic application. IgM antibodies produced against HIV 1/2 are common biomarkers for commercial HIV LFAs.

While newer generations of tests detect for both HIV 1/2 antibodies and the p24 antigen to improve specificity for HIV, disease-specific IgM detection has also been used to diagnose viral diseases such dengue and the Zika virus, making the IgM a model target for a variety of disease applications. The chlamydia diagnostic utilized a novel **A**TPS **r**ehydration and **r**esolubilization **o**ptimized **w**ick (designated as the ARROW) that employed the polyethylene glycol and potassium phosphate (PEG-salt) ATPS. In this design, the sample solution is added to the device, and the solution directly resolubilizes the ATPS components during flow, resulting in phase separation and subsequent concentration of *C. trachomatis* within paper. The IgM diagnostic design utilized a test tube containing dried nanoprobe conjugates and a paper strip design containing dried UCON-50-HB-5100 and potassium phosphate (UCON-salt) ATPS components. In this **t**ube and **U**CON-based **b**iomarker **e**xtraction setup (designated as the TUBE), the dried components are designed to be resolubilized in a specific order in which the target is first captured by the conjugates and then concentrated within paper.

Note that the execution of both designs is more difficult than merely dehydrating components and subsequently rehydrating them, as the rehydrated components need to yield the appropriate phase separation conditions. Accordingly, this process was optimized so that it properly integrated with an LFA and demonstrated its ability to improve the LFA limit of detection for infectious disease biomarkers by 10-fold without compromising the accuracy of the test results. To our knowledge, this is the first demonstration of dehydrating ATPS components onto paper, allowing only the sample to be added to achieve phase separation and concentration of the target.

3.2 Materials and Methods

3.2.1 Preparation of Anti-IgM Antibody-decorated Gold Nanoprobes (anti-IgM GNPs)

Citrate-capped gold nanoparticles were synthesized according to Frens and coworkers with slight modifications [37]. Briefly, 100 µL of 1% w/v gold(III) chloride hydrate solution was dissolved in 10 mL of UltraPure sterile water (Rockland Immunochemicals Inc., Gilbertsville, PA). The solution was stirred and heated to a boil, after which 90 µL of a 2% (w/v) tribasic sodium citrate solution was added. The color of the reaction mixture was allowed to turn red-orange over the course of 10 min. To form functionalized gold nanoprobes (GNPs), 60 µL of 100 mM sodium borate buffer (pH 9) was added to 1 mL of a citrate-capped gold nanoparticle suspension, followed by 16 µg of anti-human IgM antibodies (IgM-Ab) (MyBioSource, San Diego, CA). The reaction mixture was placed on a shaker for 30 min to facilitate the formation of dative bonds between the antibodies and the GNPs. 100 µL of 10% w/v bovine serum albumin (BSA) was then added to the suspension and then placed on a shaker for 10 min. Free antibodies were removed by centrifugation and the pellet was resuspended in 100 µL of 100 mM sodium borate buffer (pH 9.0). All materials, chemicals, and reagents were purchased from Sigma-Aldrich (St. Louis, MO) unless otherwise specified.

3.2.2 Preparation of Anti-*Chlamydia trachomatis* Antibody-decorated Dextran-coated Gold Nanoprobes (anti-CT DGNPs)

Dextran-coated gold nanoparticles (DGNs) were synthesized according to Min and coworkers with slight modifications [69]. Since these nanoparticles have been previously shown by our group to provide enhanced stability in high-salt conditions, they were used specifically with the PEG-salt ATPS which requires a higher salt concentration than the UCON-salt system. Briefly, 750 mg of dextran (Mw 15,000–25,000) from *Leuconostoc spp*. was dissolved in 10 mL

of UltraPure sterile water. The solution was stirred and heated to a boil, after which 135 µL of a 1% w/v gold(III) chloride hydrate solution was added. The color of the reaction mixture turned reddish-violet, and was stirred and boiled for about 20 min. To form functionalized dextran-coated gold nanoprobes (DGNPs), 35 µL of 100 mM sodium borate buffer (pH 9) was added to 1 mL of a DGN suspension, followed by 16 µg of anti-*C. trachomatis* antibodies (CT-Ab). The reaction mixture was placed on a shaker for 20 min to facilitate the formation of dative bonds between the antibodies and the DGNs. 100 µL of 10% w/v BSA was then added to the suspension and then placed on a shaker for 10 min. Free antibodies were removed by centrifugation and the pellet was resuspended in 100 µL of 100 mM sodium borate buffer (pH 9.0).

3.2.3 Preparation of LFA tests for *C. trachomatis* and IgM Detection

Conventional LFA strips consisted of overlapping pads placed on an adhesive backing. The pads were as follows: a sample pad, a conjugate pad that houses dried nanoprobe conjugates, a nitrocellulose membrane with immobilized antibodies or proteins that constitute the test and control lines for biomarker detection, and an absorption pad to wick and drive fluid across the entire strip. All LFA tests in this study utilized the sandwich assay format. In this format, the presence of the target biomarker in sufficient quantities will produce a red test line, as the gold nanoprobes will first bind to the biomarker, which will then be captured by immobilized antibodies on the test line. An absence or insufficient quantity of the biomarker will result in no visible test line. The presence of a control line indicates the completion of flow and the validity of the test.

On the LFA tests for *C. trachomatis*, a solution of 2 mg mL^{-1} anti *C. trachomatis* antibodies and 25% w/v sucrose was first printed onto a nitrocellulose membrane to form the test

line. Secondary anti-IgG antibodies, which bind to the primary antibodies on the anti-CT DGNPs, were printed downstream of the CT-Ab test line to form the control line. The membrane was then left in a vacuum-sealed desiccation chamber overnight to immobilize the antibodies.

On the LFA tests for human IgM, a solution of 1.5 mg mL^{-1} anti-human IgM antibodies (EastCoast Bio, North Berwick, ME) and 25% w/v sucrose was first printed onto a nitrocellulose membrane to form the test line. A solution of 0.2 mg mL^{-1} Protein A, which binds to the primary antibodies on the anti-IgM GNPs, was printed to form the control line. The membrane was also left in a vacuum-sealed desiccation chamber overnight.

3.2.4 Preparation of the ARROW and TUBE Designs

To dehydrate the ATPS and LFA components in paper, pieces of fiberglass paper were cut into appropriate geometries and placed onto a Petri dish. Solutions of the ATPS components were made to the appropriate concentrations and pipetted onto the paper segments. To prepare the ARROW, the ATPS components used were polyethylene glycol (PEG) 8000 and potassium phosphate salt dissolved in phosphate-buffered saline (PBS). To prepare the TUBE design, the ATPS components used were UCON-50-HB-5100 and potassium phosphate salt dissolved in PBS. To dehydrate the components, the paper segments were placed under very low pressure using a Labconco FreeZone 4.5 lyophilizer (Fisher Scientific, Hampton, NH) for 2 hours.

3.2.5 Scanning Electron Microscopy (SEM) Characterization

Paper segments were cut and treated using the dehydration methods described above. Paper samples included segments dehydrated with 15% (w/w) potassium phosphate, 10% (w/w) PEG, a mixture of 30% (w/w) UCON-50-HB-5100 and 3% (w/w) potassium phosphate, or no additional components (i.e., blank fiberglass). The paper segments were individually placed onto a dry carbon tape-covered holder and sputtered with a metallic coating using a South Bay

Technology Ion Beam Sputtering/Etching System (South Bay Technology, San Clemente, CA). Samples were imaged at about 500x magnification at 10 kV using a ZEISS Supra 40VP SEM (ZEISS, Irvine, CA) at the Electron Imaging Center for NanoMachines and CNSI at UCLA.

3.2.6 Observing the Rehydration Order of PEG and Potassium Phosphate

In order to visualize the phase separation of the ATPS on paper, BSA-conjugated DGNPs (BSA-DGNPs), which are burgundy/light purple due to surface plasmon resonance [70,71], and Brilliant Blue FCF dye (The Kroger Co., Cincinnati, OH) were both added to a solution of an ATPS made in PBS. It was confirmed that upon completion of the phase separation of this system in a test tube, the BSA-DGNPs partitioned extremely to the PEG-poor phase, while the Brilliant Blue dye partitioned to the PEG-rich phase [20]. Therefore, this suspension was used to identify the locations of PEG-poor phase (burgundy/light purple in color), PEG-rich phase (light blue in color), and mixed domain regions (dark blue/dark purple in color) directly on the paper.

Experiments were performed with only a single sheet of the ARROW and without a tapered tip in order to better observe the phase separation behavior. In one condition, the potassium phosphate was dehydrated upstream of the PEG, and in another condition the PEG was dehydrated upstream of the potassium phosphate. In a third condition, the PEG was mixed with potassium phosphate and then dehydrated together. The concentrations of the dehydrated components were 15% (w/w) potassium phosphate and 10% (w/w) PEG 8000. Images were taken with a Canon EOS 1000D camera (Canon U.S.A., Inc., Lake Success, NY).

3.2.7 Observing the Rehydration Order of UCON-50-HB-5100 and Potassium Phosphate

In order to first determine the partitioning of the colorimetric indicators in the UCON-50-HB-5100-potassium phosphate ATPS, red-colored BSA-conjugated GNPs (BSA-GNPs) and Brilliant Blue FCF dye were both added to an ATPS solution in PBS. After phase separation in a tube, the BSA-GNPs partitioned extremely to the bottom, UCON-poor phase while the Brilliant Blue dye partitioned into the top, UCON-rich phase. Therefore, for phase separation of dehydrated ATPSs, the location of the UCON-poor phase was identified with the red color of the BSA-GNPs. Similarly, the locations of UCON-rich phase and mixed domain regions were identified with light blue and dark purple color, respectively.

Three different conditions were tested using the UCON-salt system on a single strip of paper. In one condition, the UCON-50-HB-5100 was dehydrated downstream of potassium phosphate, in a second condition the UCON-50-HB-5100 was dehydrated upstream of potassium phosphate, and in the last condition, the UCON-50-HB-5100 was mixed with potassium phosphate and then dehydrated together. The concentrations of the dehydrated components were 30% (w/w) UCON-50-HB-5100 and 3% (w/w) potassium phosphate. Images were taken at different time points with a video camera.

3.2.8 Observing the Dynamics of Phase Separation

To visualize phase separation of the dehydrated ATPS systems, only the ARROW component of the diagnostic, with 15% (w/w) potassium phosphate dehydrated upstream of dehydrated 10% (w/w) PEG 8000, was used. This setup did not contain the LFA membrane or conjugate pad. The suspension containing the BSA-DGNPs and Brilliant Blue dye was allowed to flow along the strip until the fluid reached the end the paper. To visualize phase separation of

the dehydrated UCON-salt ATPS, the mixed condition UCON-salt pad was dehydrated with 30% (w/w) and 3% (w/w) potassium phosphate onto a fiberglass paper strip. This setup did not include the LFA membrane or the tube with dehydrated GNPs. A PBS solution containing BSA-GNPs and Brilliant Blue dye was allowed to flow up the strip. Images were captured at different time points using a video camera.

3.2.9 Detection of *C. trachomatis* using the Integrated LFA and ARROW

LFA tests were performed to detect varying *C. trachomatis* concentrations between 0.5 and 500 μg mL^{-1}, such that they were evenly spaced on a logarithmic scale, for the LFA only system and the integrated LFA and ARROW system. The sample suspensions contained *C. trachomatis* (EastCoast Bio, North Berwick, ME) diluted in PBS. The sample solution volumes were 70 and 600 μL per test for the control and dehydrated ATPS conditions, respectively. A smaller sample volume was used for the control because it did not have the ARROW component, and therefore, did not require as much sample volume to run the test. The control LFA strip was comprised of a sample pad (treated with 1% BSA), a conjugate pad containing the anti-CT DGNPs, a nitrocellulose membrane, and an absorbent pad. The integrated design substituted the initial sample pad with the ARROW component. The authors did not include a blank paper wick to mimic the ARROW component in the control since comparing to the case without the wick was a more stringent comparison as *C. trachomatis* can be lost in a blank wick. The tests were allowed to run for 15 minutes before images were taken with a Canon EOS 1000D camera.

3.2.10 Detection of Human IgM using the Integrated LFA and TUBE

LFA tests were conducted on sample solutions of human IgM (EastCoast Bio, North Berwick, ME) in PBS, with varying human IgM concentrations from 0.01 to 10 μg mL^{-1}. Here, the sample volumes used for the control case and the dehydrated ATPS conditions were 25 μL

and 150 µL, respectively. The control LFA strip was comprised of a sample pad (treated with 1% BSA), a conjugate pad containing the anti-IgM GNPs, a nitrocellulose membrane, and an absorbent pad. In the TUBE design, the sample pad and conjugate pad were omitted and replaced with the dehydrated UCON-salt strip and a spacer pad treated with 1% BSA in water. GNPs of an equal amount as the control case were mixed with BSA to a total BSA concentration of 1% (w/v), and applied to a microcentrifuge tube. The tube was then placed under very low pressure using a Labconco FreeZone 4.5 lyophilizer for 1 hour, leaving the GNPs in dried powder form.

To run the test using the TUBE design, an IgM sample was added to the sample tube to rehydrate the GNPs and allow binding to the target. Then, the test strip with the dehydrated UCON-salt pad was dipped into the tube and the sample was allowed to wick up the strip toward the absorbent pad. The tests were allowed to run for 12 minutes before images were taken with a Canon EOS 1000D camera.

3.2.11 Quantitative Image Analysis

Images were analyzed using a customized MATLAB script previously developed and described by our lab [19]. Briefly, in this program, LFA images are cropped just inside the edges of the membrane before being analyzed. The program takes several calibration images of a positive test with visible control and test lines, and uses those to determine the length from the control line to the test line. It then analyzes the experimental images by determining the average pixel intensity on the test line and subtracting the average pixel intensity of the membrane background. Finally, it returns the relative test line signal as a percentage of the maximum signal intensity tested (which is produced by the highest concentration tested). The pixel intensity was plotted using GraphPad Prism.

3.3 Results and Discussion

3.3.1 Importance of the Rehydration Order of PEG and Potassium Phosphate

The novel ARROW design introduces the unexplored concept of phase separation after sequential ATPS component resolubilization during fluid flow, which is in contrast to the traditional method of ATPS research that examines phase separation in a stagnant solution with an initial homogenous distribution of ATPS components. Therefore, the authors investigated the effect of the PEG and potassium phosphate rehydration order on the phase separation behavior within the paper. To do this, the authors utilized a suspension comprised of BSA-DGNPs and Brilliant Blue dye which allowed for the visualization of the phase separation process as the suspension flowed through the paper, a technique utilized in previous studies [20]. In short, the BSA-DGNPs partitioned into the PEG-poor phase indicated by the burgundy/light purple color, while the blue dye partitioned into the PEG-rich phase indicated by the light blue color. Regions of macroscopically mixed domains contained both BSA-DGNPs and blue dye, indicated by the dark blue/dark purple color. During fiberglass paper preparation, the location of the dehydrated ATPS components was altered, such that one condition had the dehydrated potassium phosphate located upstream of the dehydrated PEG (denoted 'Salt → PEG'), one condition had the dehydrated PEG located upstream of the dehydrated potassium phosphate (denoted 'PEG → Salt'), and a third condition contained a mixture of the PEG and potassium phosphate dehydrated across the entire length of the strip.

From these results (Figure 3.1), the authors note several interesting observations. First, the 'mixed' condition resulted in no visible phase separation as the entire strip appeared purple due to the mixture of PEG-rich and PEG-poor domains. In addition, the leading PEG-poor fluid had a significantly darker burgundy color in the 'Salt → PEG' condition compared to the 'PEG

→ Salt' condition, indicating that the 'Salt → PEG' condition contained more BSA-DGNPs in the leading fluid, and therefore, is more effective at concentrating large species. Furthermore, the PEG-rich phase exhibited significantly more volumetric growth over time in the 'Salt → PEG' condition compared to the PEG-rich phase in the 'PEG → Salt' condition. This suggests that, in the 'Salt → PEG' condition, the newly formed PEG-poor domains are able to get out of the mixed domain region and more efficiently pass through the trailing PEG-rich phase and collect into the leading PEG-poor phase. This results in the PEG-rich phase becoming larger as the mixed domains region becomes smaller. One possible reason for this phenomenon is the formation of PEG-poor channels within the PEG-rich phase that connect to the leading PEG-poor phase. Research in multiphase fluid flow within porous media has found that less viscous fluids will develop preferred channels when displacing more viscous fluids [72].

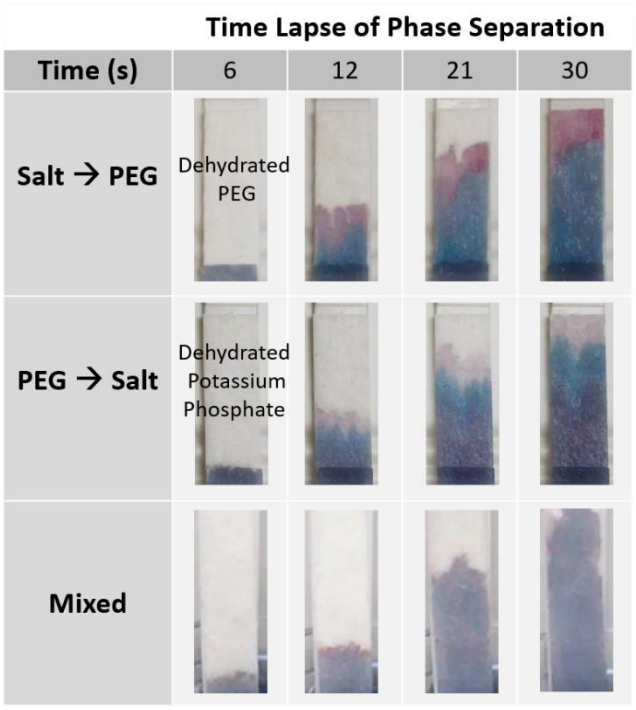

Figure 3.1 PEG-salt ATPS component rehydration order. Time-lapse visualization of phase separation within a single sheet of the ARROW design when the PEG and potassium phosphate were rehydrated in separate regions, and when they were rehydrated as a mixture. Close up images are shown of the downstream region where phase separation occurred, and therefore, the first image is at t=6 s instead of t=0 s. Visualization and identification of the

PEG-rich phase, PEG-poor phase, and macroscopically mixed domain regions were accomplished by flowing a suspension of BSA-DGNPs and Brilliant Blue dye.

The authors hypothesized that switching the location of the ATPS components, such that PEG is resolubilized prior to potassium phosphate, reduces or prevents the formation of PEG-poor channels. When considering a sample solution flowing through the 'PEG → Salt' condition at the location that the leading fluid transitions from the dehydrated PEG region to the dehydrated potassium phosphate region, the fluid contains a high concentration of resolubilized PEG and no potassium phosphate. As the fluid flows into the dehydrated potassium phosphate region, the concentration of potassium phosphate increases and phase separation occurs. If this situation is examined from the perspective of a traditional PEG and potassium phosphate phase diagram [73], initial phase separation in this leading fluid will occur at the region of high PEG and low potassium phosphate concentrations. This initial phase separation would result in a large PEG-rich phase volume and a small PEG-poor phase volume, as described by the lever rule [73,74]. The authors hypothesized that the larger volume of the initial PEG-rich phase prevents PEG-poor channels from being formed and connecting to the leading PEG-poor phase. This would hinder subsequently formed PEG-poor domains from passing through and collecting into the leading fluid. This hypothesis is supported by our observations of the 'PEG → Salt' condition, notably: (i) the lower concentration of BSA-DGNPs in the leading PEG-poor phase, indicated by the lighter burgundy color, and (ii) the presence of a macroscopically mixed domain region, located behind the PEG-rich phase, indicated by the dark purple color. From these observations, the authors decided to use the 'Salt → PEG' condition in the final design incorporated with the LFA.

3.3.2. Importance of the Rehydration Order of UCON-50-HB-5100 and Potassium Phosphate

In the TUBE design, the authors also investigated the order of UCON-50-HB-5100 and potassium phosphate rehydration order on the phase separation behavior in paper, using the same colorimetric indicators as previously described. Three different combinations were tested (Figure 3.2): one in which the dehydrated potassium phosphate was located upstream of the dehydrated UCON-50-HB-5100 ('Salt → UCON'), one in which the dehydrated UCON-50-HB-5100 was located upstream of the dehydrated potassium phosphate ('UCON → Salt'), and one in which the two components were mixed together and applied evenly along the entire fiberglass strip ('Mixed'). The authors observed that the 'UCON → Salt' condition resulted in very little noticeable separation, as can be seen by the purple color caused by the blending of both the mixed domains of BSA-GNPs and the blue dye along the strip. This is in agreement with the hypothesis that a high volume of a highly concentrated UCON-rich phase prevents the formation of UCON-poor channels, and in this case, completely prevents the formation of a distinct UCON-poor leading front. On the other hand, phase separation was observed in the 'Salt → UCON' condition, in which the leading front containing the GNPs was visible within 15 seconds. In the 'mixed' condition, phase separation occurred within 10 seconds, indicating that rehydrating a mixture of UCON and potassium phosphate does not hinder the collection of UCON-poor domains and the formation of the UCON-poor phase. Although the 'mixed' condition produced a leading front volume approximately equal to that of the 'Salt → UCON' case, it also produced a lower flow rate, which has been shown to provide additional benefits in improving the LFA detection limit [75]. For this reason, the 'mixed' condition was used in the design later incorporated with the LFA.

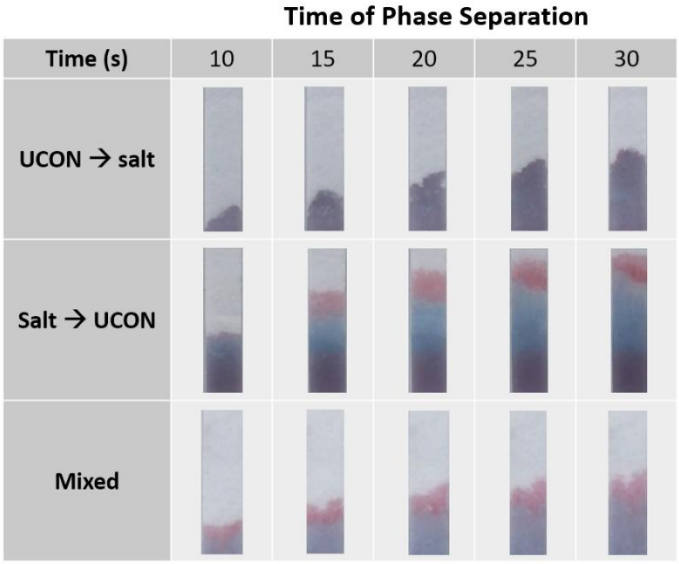

Figure 3.2 UCON-salt ATPS component rehydration order. Time-lapse visualization of phase separation within a single fiberglass strip when the UCON-50-HB-5100 and potassium phosphate were rehydrated in separate regions, and when they were rehydrated as a mixture. Images were cropped to contain the same area of a strip in order to observe relative flow rates. Visualization and identification of the UCON-rich phase, UCON-poor phase, and macroscopically mixed domain regions were accomplished by flowing a suspension of BSA-GNPs and Brilliant Blue dye.

3.3.3. The Dynamics of Phase Separation

Once the rehydration conditions for the two ATPSs were optimized, the phase separation time within these two systems was observed. It was important to demonstrate that these methods of dehydration allowed for rapid rehydration of the ATPS components during the flow of the sample solution through the diagnostic. As shown in Figure 3.3a, successful phase separation is observed in the ARROW setup, in which phase separation occurred shortly after the suspension flowed into the dehydrated PEG region. The newly-formed PEG-poor region collected into the leading fluid in front of the PEG-rich region, mimicking an important phenomena discovered in our previous work [20], which is necessary considering that the PEG-poor region will contain the concentrated *C. trachomatis* and needs to be in the leading fluid when flowing through the conjugate pad. The process of flowing through the ARROW only took approximately 30 s.

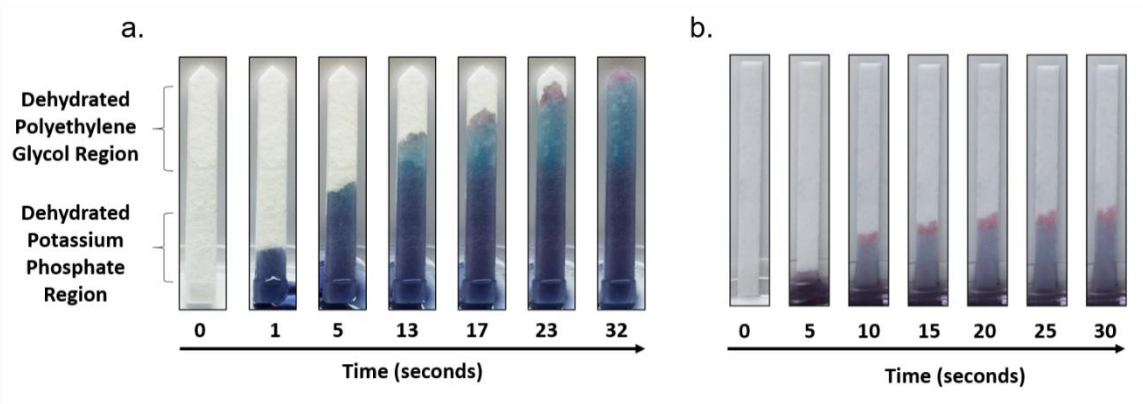

Figure 3.3 Dynamics of phase separation. a. Time-lapse images were taken of the ARROW with separated two-phase components during the process of fluid flow. The fluid consisted of a suspension of BSA-DGNPs and Brilliant Blue dye, which allowed for visualization of the phase separation. b. Time-lapse images were taken of the mixed UCON-salt design during the process of rehydration by a suspension of BSA-GNPs and Brilliant Blue dye.

Interestingly, the PEG-poor region in the leading fluid expanded as the fluid flowed through the dehydrated PEG region, which is best observed in the transition from time points 13 s to 23 s. During this time period, the PEG-rich region also expanded but maintained its initial location at the beginning of the dehydrated PEG region. These two observations together suggest that the dehydrated PEG and potassium phosphate quantities are sufficient to continue phase separation after initial phase separation in the leading fluid, and that the newly formed PEG-poor domains are flowing through the PEG-rich region to collect at the leading PEG-poor region.

Phase separation was also seen in the mixed UCON-salt design (Figure 3.3b) within 10 s. Here, the UCON-poor region containing BSA-GNPs collected into the leading fluid front, concentrating the GNPs from the large initial solution into a small volume, which remained consistent throughout the duration of the flow study. After the phase separation (10 s to 30 s), there was a noticeable decrease in the flow speed through the strip, which is likely attributed to the formation of the viscous UCON-rich lagging phase.

3.3.4. Integrating the LFA with the Dehydrated ATPS

The dehydrated components of the PEG-salt ATPS and the UCON-salt ATPS were used to produce two different assay designs. The dehydrated PEG-salt ATPS diagnostic device (Figure 3.4) was comprised of two major components: the ARROW and the standard LFA. The ARROW consisted of several fiberglass paper sheets layered and compacted together. Considering that the function of the ATPS is to concentrate the target pathogen, it was necessary that the ARROW was able to wick up a large volume of sample solution. 15% (w/w) potassium phosphate was dehydrated in the upstream portion of each fiberglass sheet, while 10% (w/w) PEG 8000 was dehydrated in the downstream portion of each fiberglass sheet. It was important to leave blank space between the dehydrated PEG and the tip of the sheet to allow for collection of the PEG-poor phase that contained the concentrated pathogen. The downstream tip of each sheet was tapered to form a point, which facilitates proper transition of the liquid into the conjugate pad.

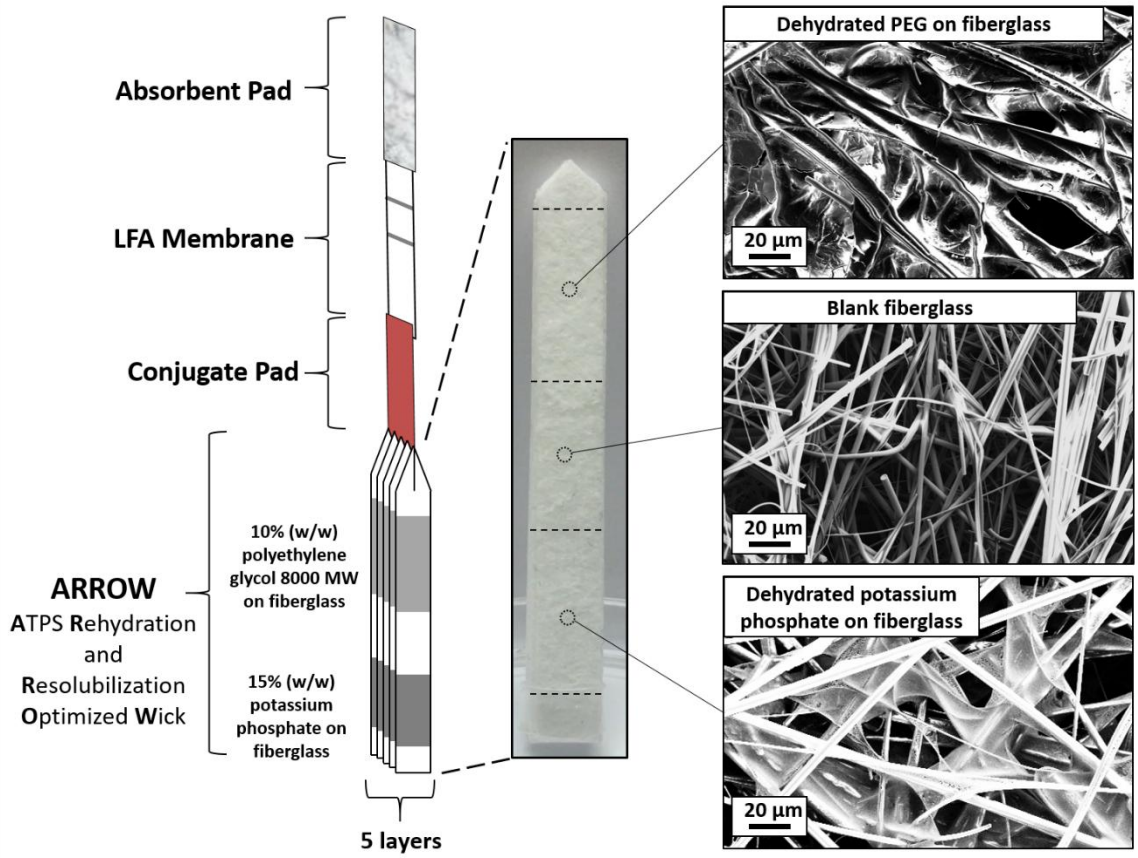

Figure 3.4 The integrated ARROW and LFA diagnostic design layout, which includes a photo of the ARROW and SEM images of the dehydrated PEG on fiberglass, blank fiberglass, and dehydrated potassium phosphate on fiberglass. The top and bottom tips of the fiberglass paper sheet were also blank fiberglass.

The simplistic design of the ARROW achieves thermodynamic concentration and can be mass-produced with relative ease. While the design may add some complexity relative to standard LFA diagnostics, this complexity only involves the assembly process, whereas the processes used to apply and dehydrate components onto the ARROW strips are not significantly different from those used in standard LFA manufacturing. The LFA portion of the diagnostic consisted of the conjugate pad, containing the colorimetric indicator, connected to a nitrocellulose membrane with printed primary and secondary antibodies, and followed by an absorbent pad. The LFA portion interfaced with the ARROW by fitting a small upstream portion of the conjugate pad perpendicularly into a slit that had been cut in the ARROW.

The ARROW was designed to concentrate a biomarker capable of partitioning to a single phase on its own. Since the *C. trachomatis* whole bacteria is relatively large (0.8 to 1 μm), it can partition extremely to the PEG-poor phase without intervention. However, many infectious disease biomarker targets, such as the HIV antibodies typically detected in HIV rapid tests, are smaller in scale and do not partition extremely to a single phase. Therefore, another strategy must be utilized to concentrate these biomarkers. Previously, our group demonstrated that the gold nanoparticle conjugates typically used in LFA can be added directly into an ATPS, where they partition extremely to the UCON-poor phase in a polymer-salt ATPS [17,18]. In this format, the GNPs were added to the sample solution and were allowed to bind the target present in solution before phase separation occurred. After the onset of phase separation, the large GNP-target complexes partitioned to the UCON-poor phase, thus concentrating the target into the UCON-poor phase. Extraction of the GNPs and application to the LFA yielded improvements in the detection limit of these protein targets. One of the goals of the current study is to incorporate this mechanism into the dehydrated format to concentrate smaller targets, using a human IgM antibody (970 kDa, or approximately 37 nm in diameter) as a model biomarker target.

The TUBE design (Figure 3.5) was comprised of two main components: the sample tube, and the test strip that consists of the UCON-salt pads connected to the standard LFA. In this design, it is imperative that the GNPs access the entire sample solution and bind to the target prior to the ATPS concentration step. It is also important that after binding the target, the GNPs access the dehydrated ATPS region at the same time in order to maximize the GNPs that become concentrated into the resulting UCON-poor leading front. One approach to achieve these design criteria was to dry the conjugates and store them in powder form housed in a sample microcentrifuge tube. In this case, the liquid sample is first added into the tube, in which the

GNPs are resolubilized and immediately bind to any human IgM present. Next, the test strip is added into the sample tube, and the GNPs collectively wick up the test strip, first making contact with the UCON-salt pad. When this occurs, the dehydrated UCON-salt mixture is rehydrated by the wicking solution, inducing the formation and separation of the UCON-rich and the UCON-poor phases. The GNPs are concentrated in the newly-formed UCON-poor fluid front, while the newly-formed and more viscous UCON-rich region lags behind. The spacer pad contains BSA to ensure even transition of the UCON-poor phase into the nitrocellulose-based detection region and prevent nonspecific binding of the GNPs.

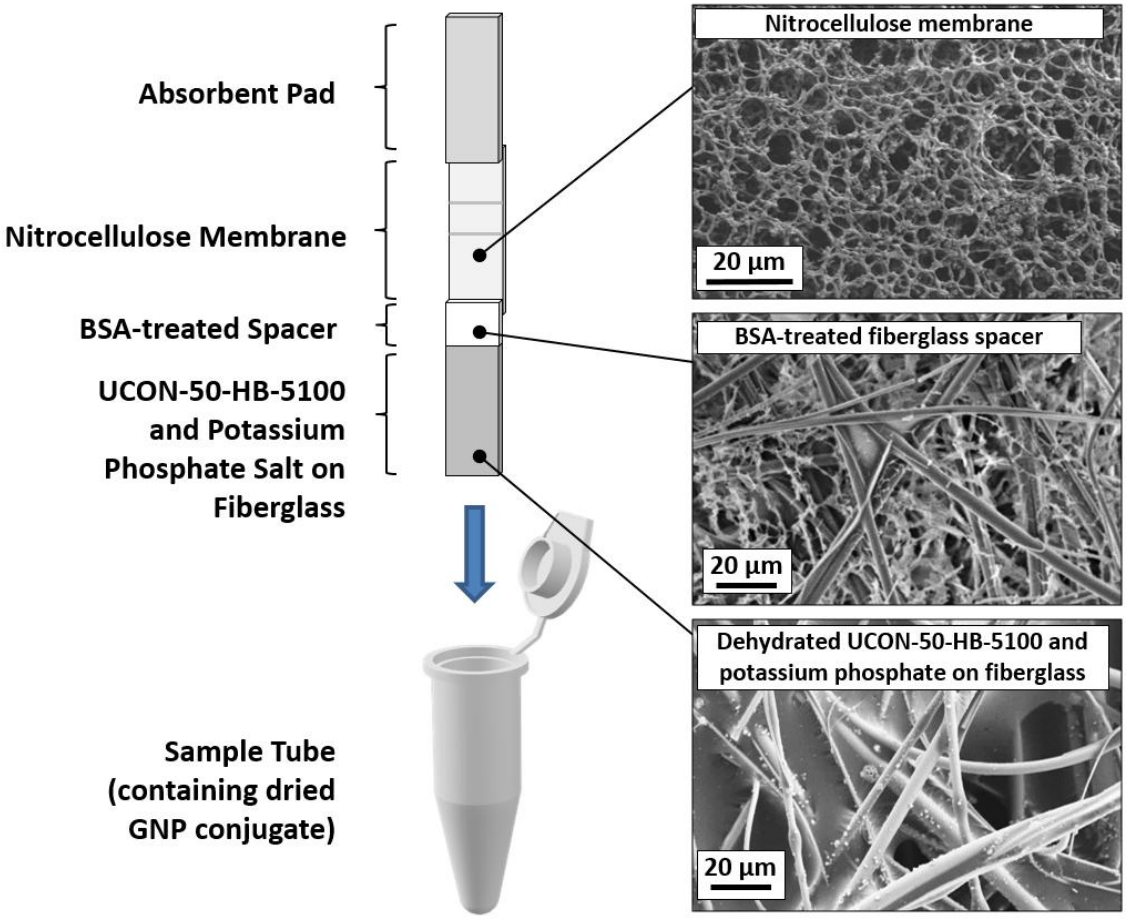

Figure 3.5 The integrated TUBE and LFA design, which includes the sample tube containing the dried GNP conjugate and the test strip containing the UCON-salt ATPS dehydrated into a fiberglass pad. SEM images of the UCON-salt pad, the BSA-treated spacer, and the nitrocellulose membrane are also shown.

The SEM image (Figure 3.4) of the blank fiberglass region of the fiberglass paper shows a porous fiber-based matrix structure. The dehydrated PEG, potassium phosphate, and mixed UCON-50-HB-5100-potassium phosphate regions show a similar porous structure, with the addition of web-like connections, which is believed to contain a majority of their respective ATPS components (Figure 3.4). These images demonstrate that the process of dehydration does not significantly deform the porous structure of the fiberglass paper, which is critical for proper wicking of the sample fluid. An SEM image of the nitrocellulose paper (Figure 3.5) shows a typical pore structure and size that accommodates transport of the sample fluid

3.3.5. Improved Limit of Detection for *C. trachomatis* and Human IgM using the Integrated LFA and Dehydrated ATPS

The ARROW design was then used to effectively concentrate a *C. trachomatis* sample suspension, resulting in an improved limit of detection for LFA. To do this, sample suspensions of varying initial concentrations of *C. trachomatis* were applied to LFA test strips, with and without the ARROW component. As indicated in the results of the LFA panel (Figure 3.6), the LFA only system started showing false negative results at around 15.8 μg mL^{-1} *C. trachomatis* while the integrated LFA and ARROW system started showing false negative results at around 1.58 μg mL^{-1} *C. trachomatis*. This visually demonstrates a 10-fold improvement in the limit of detection.

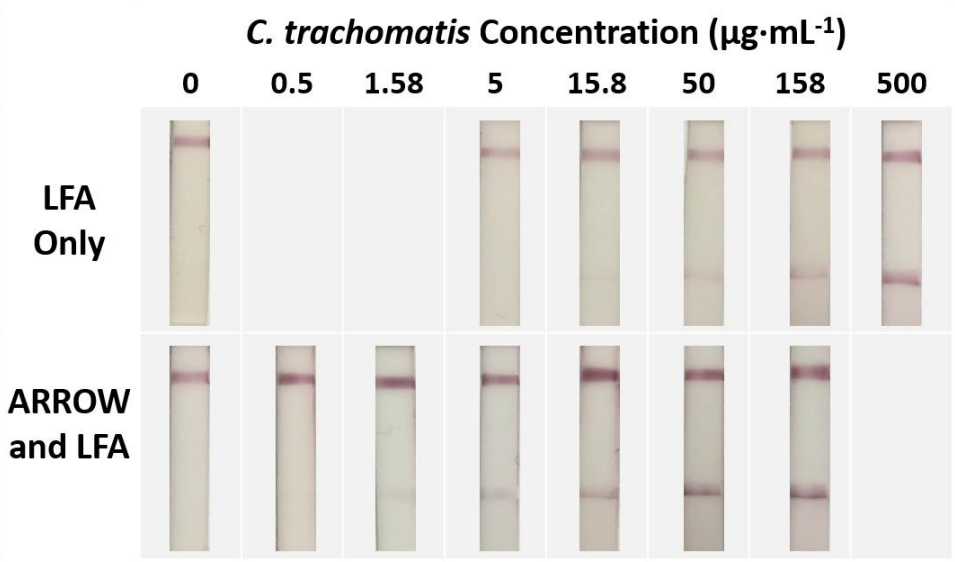

Figure 3.6 Improvement in the limit of detection of *C. trachomatis* LFA by incorporation of the ARROW. Comparison of LFA results at varying *C. trachomatis* concentrations, with and without the ARROW is presented. Test lines are located on the bottom of the LFA strips and control lines are located on the top of the LFA test strips. Negative control results are shown in the leftmost panels for 0 µg mL^{-1} *C. trachomatis*.

Lastly, the TUBE diagnostic was used to effectively concentrate human IgM in a PBS sample and improve the LFA limit of detection (Figure 3.7). In this case, the detection limit of the LFA control was determined to be 0.31 µg mL^{-1}. On the other hand, the integrated TUBE and LFA system was able to accurately detect human IgM at 0.031 µg mL^{-1}, visually demonstrating a 10-fold improvement in the limit of detection compared to the LFA control. The observed detection limit improvements achieved within both the ARROW and TUBE designs are attributed to the concentration of the target biomarker into a volume that is smaller than the original sample. As this volume flows across the test line region, there is an enhanced the probability that the immobilized antibodies will bind to the concentrated target. An interesting point that may be worth further investigation is the theoretical extent by which the volume of the leading phase can be reduced before it becomes impractical (i.e., the leading phase volume becomes too small and bypasses the test line quickly without providing adequate time for binding between the biomarker and the test line antibodies). Future investigations into the

balance between adequate target binding time and leading front volume are of particular interest to our group.

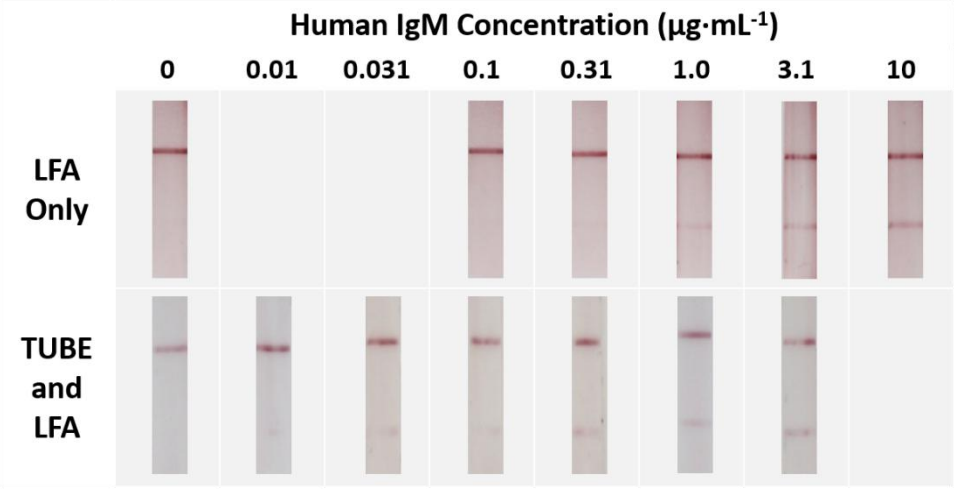

Figure 3.7 Improvement in the limit of detection of human IgM LFA by incorporation of the TUBE. A comparison of LFA results at varying human IgM concentrations, with and without the TUBE is presented. Test lines are located on the bottom of the LFA strips and control lines are located on the top of the LFA test strips. Negative control results are shown in the leftmost panels.

To quantitatively assess the improvement in the limit of detection, the pixel contrast of the test lines on the LFA images was calculated using a customized MATLAB program developed and described by our laboratory (Figure 3.8) [19]. For any given concentration of *C. trachomatis*, there was a significant increase in the relative test line intensity for the integrated ARROW and LFA system compared to the LFA only system. For example, at 50 µg mL^{-1} *C. trachomatis*, the LFA only condition had a relative intensity of 30.3% ± 10.8%, while the integrated ARROW and LFA had a relative intensity of 76.8% ± 11.1%. Similar results were seen in the image analysis of the IgM tests with the integrated TUBE and LFA at all IgM concentrations. For example, at 1.0 µg mL^{-1} IgM, the LFA only condition had a relative pixel intensity of 36.1% ± 6.6%, while the integrated TUBE and LFA had a pixel contrast intensity of 66.1% ± 10.0%. In both cases, the image analysis was able to detect test lines with significantly

greater intensities than the background at lower concentrations when the dehydrated ATPS components were integrated.

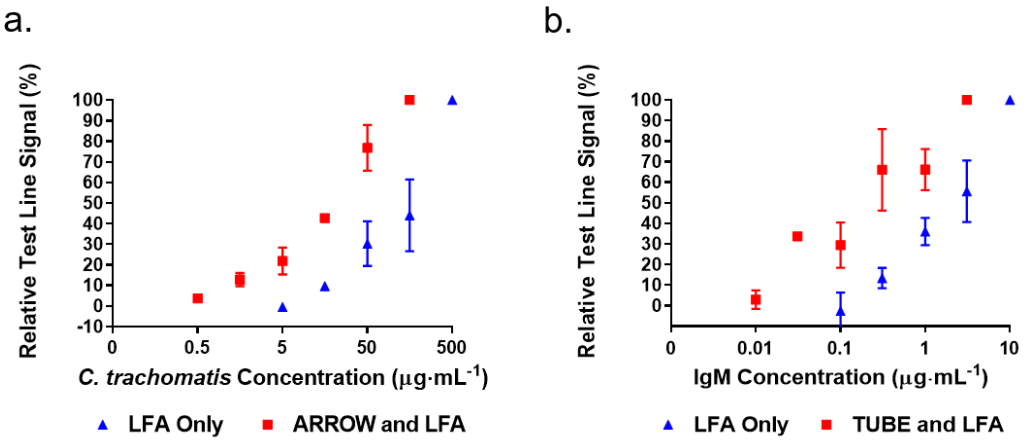

Figure 3.8 Plots of the quantified LFA test line intensities for a. the ARROW/LFA system and the LFA only system, and b. the TUBE/LFA system and the LFA only system.

3.3.6. Improved Detection of IgM in Undiluted Serum

To demonstrate its utility in more complex biological matrices, the TUBE design was also used to detect human IgM spiked in fetal bovine serum (FBS). The test procedure was identical to that of the tests in PBS. As with the case of the tests in PBS, all tests in FBS did not require any prior dilution in buffers, extraction steps, or running buffer additions to aid flow. The undiluted sample volumes of the control LFA and the TUBE and LFA were 25 μL and 150 μL, respectively. As shown in Figure 3.9, the detection limit of the LFA control remained at 0.31 μg mL^{-1} and the detection limit of the TUBE and LFA integration was 0.031 μg mL^{-1}. These experiments demonstrated that the TUBE design was capable of processing serum samples and demonstrated a 10-fold improvement in the LFA detection limit for the human IgM.

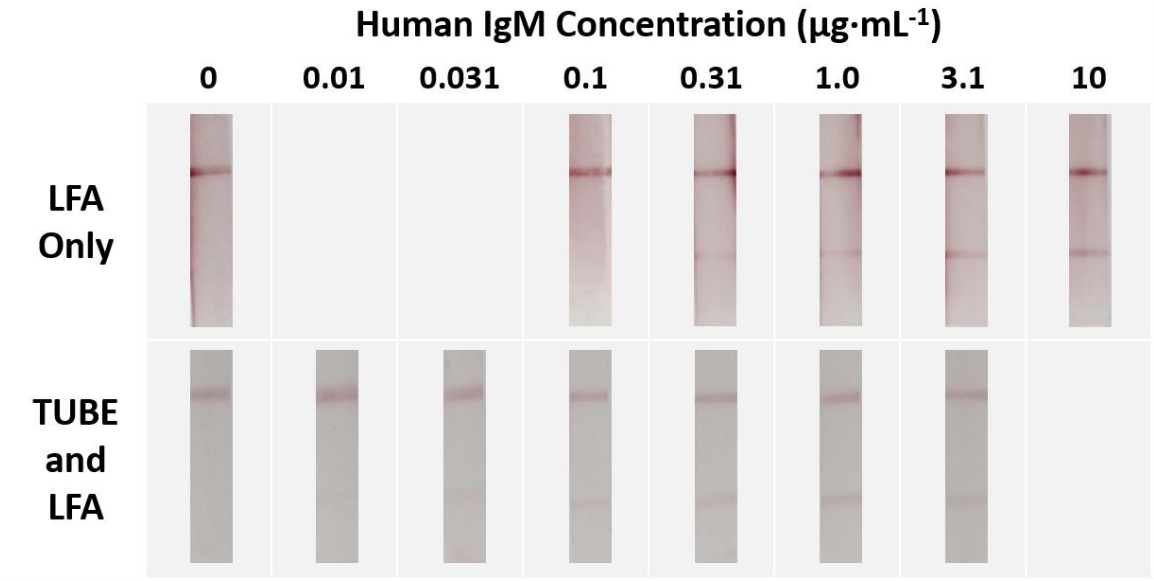

Figure 3.9 The TUBE is used to improve the LFA limit of detection of human IgM in FBS. A comparison of LFA results at varying human IgM concentrations, with and without the TUBE is presented. The LFA control detected IgM at a concentration as low as 0.31 µg mL^{-1}, whereas the TUBE and LFA integration detected IgM at a concentration as low as 0.031 µg mL^{-1}.

3.4 Conclusions

In the current study, the authors present two new paper-based diagnostic designs that are capable of thermodynamic target concentration through dehydration of ATPS components. With these paper-based devices, only the sample needs to be added without additional sample preparation steps. The dehydrated PEG-potassium phosphate salt ATPS was used in the ARROW design to concentrate and detect *C. trachomatis*, and the dehydrated UCON-50-HB-5100-potassium phosphate ATPS was used in the TUBE design to concentrate and detect human IgM. Specifically, the ARROW and the TUBE designs improved the LFA limit of detection for their respective biomarker targets by 10-fold, while still providing results in less than 15 minutes.

An LFA diagnostic with improved sensitivity, that still maintains its low cost, rapid time to result, and ease of use, will significantly increase its applicability as a POC screening test for

infectious diseases. It is possible that the dehydrated ATPS technology can be applied to a variety of different targets suitable for detection by LFA. Most LFA-based diagnostics for infectious diseases are not developed or not used due to poor sensitivity. Considering that the dehydrated ATPS can improve LFA sensitivity without adding any additional steps to the user, this novel technology has the potential to create many viable infectious disease LFA tests, both for use by physicians and as over-the-counter tests.

Chapter 4. Extending the Washburn Model to Aqueous Two-Phase Systems in Porous Media

4.1 Introduction

4.1.1 The Importance of Modeling Phase Separation in Paper

Paper-based phase separation of ATPSs has been demonstrated in the PEG-potassium phosphate salt system and more recently been demonstrated in the Triton X-114 micellar system, as discussed in Chapter 2. In both cases, the addition of a mixed solution to fiberglass paper resulted in visible phase separation within minutes, in which one of the two phases is formed at the leading fluid front (the leading phase) and the other phase follows behind (the lagging phase). In the case of the PEG-salt ATPS, the leading phase is the salt-rich phase and the lagging phase is the PEG-rich phase. For the Triton X-114 ATPS, the micelle-poor phase is the leading phase and the micelle-rich phase is the lagging phase. While this phenomenon is not completely understood, the porous paper is an added element that can significantly alter the traditional mechanism of phase separation. In general, the pores in paper enable fluid to wick and move via capillary action, which introduces a convective component that is not seen in traditional test tubes [58]. Furthermore, the density of the phases, which was a dominant parameter that dictated traditional phase separation and the orientation of the phases, seems to have less of an effect in paper as the phases with greater density still appear to flow higher in vertical flow (i.e. the salt-rich phase of the UCON-salt ATPS). New possible mechanisms can be hypothesized from a variety of topics and fields, ranging from fluid flow in porous media, multiphase flow, paper or thin-layer chromatography, as well as thermodynamic models of stochastic processes such as nucleation and spinodal decomposition, in order to provide insight.

A mathematical model that can accurately predict two-phase system wicking behavior in paper-based devices is essential in the process of device design. Such a model can be used to identify, under conditions that allow for phase separation, the leading phase and lagging phase for any given ATPS. Furthermore, the model could be used to determine the optimal concentrations and volumes of two-phase components that are required to produce a specific flow pattern. This is especially important as paper-based ATPSs have great potential for automated concentration of biomolecules. In order to model the phase separation behavior on a macroscopic level, we looked into fluid mechanics models for wicking in porous media.

Wicking or spontaneous imbibition is the movement of a liquid into a porous medium, driven by a negative capillary pressure that is created at the liquid-air interface. The capillary pressure arises as a result of wetting the surface of the porous material. Wicking plays an important role in many natural and industrial phenomena. One of the accepted approaches to mathematically modeling the wicking phenomenon is the Washburn equation, or the Lucas-Washburn equation, in which the porous medium is modeled as a bundle of smaller and aligned capillary tubes of equal radii.

In this chapter, we evaluated the Washburn model as a framework to describe the flow of isolated phases of the PEG-salt and Triton X-114 ATPSs in fiberglass paper. We compared bulk phase fluid characteristics to identify the viscosity difference between the phases as a key determinant of which phase becomes the leading phase once applied to paper. We also evaluated the Washburn model generalized for non-Newtonian power law fluids and used it to model the polymer-rich and micelle-rich phases. We then used the framework to predict the phase separation capabilities of the PEG-Dextran and PEG-polyacrylic acid ATPSs.

4.1.2 The Uses of Hydrogels

Hydrogels are loosely crosslinked hydrophilic polymer networks that are able to swell and retain aqueous solutions. They are generally highly absorbent and may contain over 90% water in their completely swollen state. Hydrogels can be comprised of both natural and synthetic polymers, and synthesized by physical or chemical crosslinks to provide 3-D structures of specific mechanical and chemical properties. Hydrogels have been extensively studied for tissue repair and drug delivery applications, in which they act as scaffold supports for cells and biomimetic membranes [76–80]. In more recent years, they have been favorable substrates for robust *in vitro* detection of analytes due to their non-fouling properties and solution-like environment, and only more recently have seen applications in combination with paper-based diagnostics [83–85].

4.1.3 Rationale for Hydrogels as an Alternative Porous Medium

The mechanisms that lead to significant reduction in phase separation time of ATPSs when they are applied to paper membranes is of great interest to our group. Several factors may contribute to this phenomenon, which include the use of a porous membrane, specific interactions (electrostatic, van der Waals, and hydrophobic/hydrophilic interactions) between the paper material and the ATPS components, viscosity differences, interfacial tensions, and gravitational and buoyant forces. By gaining a better understanding of how these factors all contribute to phase separation, we can further improve our existing device. Like paper membranes, hydrogels are porous platforms that readily accept aqueous solutions, and thus can provide another means of accelerating phase separation of ATPSs. On a broader scope of application, hydrogels also have potential compatibility with POC applications since they can be affordable, compact, and require minimal power and training to use once they are synthesized.

Therefore, in addition to using the Washburn equation as a framework for predicting phase separation in paper, we applied the framework to predict the ability of ATPSs to phase separate within hydrogels. In doing so, we successfully demonstrated phase separation of various systems in polyethylene glycol dimethacrylate-based hydrogel systems.

4.2 Theory

4.2.1 The Hagen-Poiseuille Equation – Fully Developed Flow of a Newtonian Fluid in a Circular Tube

This section summarizes the derivation of the Hagen-Poiseuille equation, which describes the laminar, fully developed flow of a Newtonian fluid through a long circular tube of constant cross section. Consider an elemental washer-like control volume within the circular tube as shown in Figure 4.1.

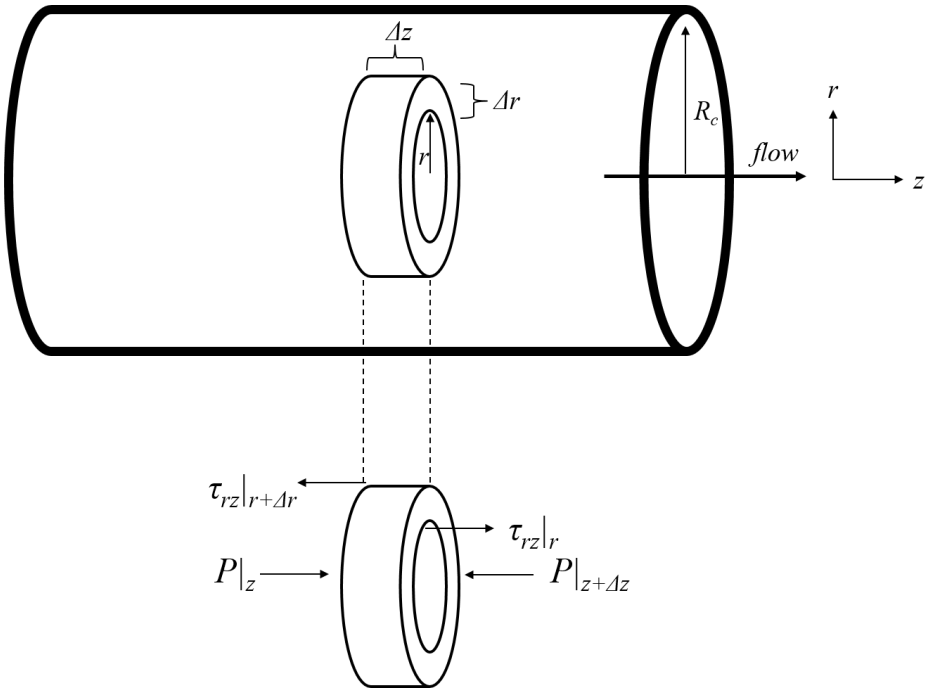

Figure 4.1 Force distribution on a selected control volume of a Newtonian fluid flowing through a circular tube.

A pressure gradient drives flow in the positive z direction. Note that since pressure decreases as we move along the z axis in the positive direction, dP/dz is negative. A force balance on the cylindrical shell incorporates the pressures at z and $z+\Delta z$ and the shear stress terms at r and $r+\Delta r$. The resulting force balance is given as

$$P\Big|_z\left[\pi(r+\Delta r)^2-\pi r^2\right]-P\Big|_{z+\Delta z}\left[\pi(r+\Delta r)^2-\pi r^2\right]+\tau_{rz}\Big|_{r+\Delta r}\left[2\pi(r+\Delta r)\Delta z\right]-\tau_{rz}\Big|_r\left[2\pi r\Delta z\right]=0 \quad (1)$$

By neglecting second order Δr terms, utilizing the mathematical property $\tau_{rz}\Big|_{r+\Delta r}\left[2\pi(r+\Delta r)\Delta z\right]=(\tau_{rz}r)\Big|_{r+\Delta r}\left[2\pi r\Delta z\right]$, and dividing both sides of the equation by $2\pi\Delta r\Delta z$, Eq. (1) can be manipulated to

$$-r\frac{P\Big|_{z+\Delta z}-P\Big|_z}{\Delta z}+\frac{\tau_{rz}\Big|_{r+\Delta r}-\tau_{rz}\Big|_r}{\Delta r}=0 \quad (2)$$

Taking the limits as $\Delta z\to 0$ and $\Delta r\to 0$ results in Eq. (3):

$$-r\frac{dP}{dz}+\frac{d(\tau_{rz}r)}{dr}=0 \quad (3)$$

$$\frac{d(\tau_{rz}r)}{dr}=r\frac{dP}{dz} \quad (4)$$

Specifically, for a Newtonian fluid, the following relationship holds:

$$\tau_{rz}=\mu\left(\frac{dV_z}{dr}\right) \quad (5)$$

in which μ is the fluid viscosity and dV_z/dr is the fluid velocity gradient, or the stream rate. Substituting Eq. (5) into Eq. (4) and integrating twice results in the following equation for the velocity profile:

$$V_z = \frac{1}{4\mu}\frac{dP}{dz}r^2 + C_1 \ln(r) + C_2 \tag{6}$$

in which C_1 and C_2 are constants of integration. Note that the pressure gradient is constant as we have assumed fully developed flow in a cylindrical tube. The relevant boundary conditions for Eq. (6) include a maximum velocity at the center of the tube (which is the furthest from the wall), and the no-slip boundary condition at the wall of the tube, which are shown below:

$$\frac{dV_z}{dr} = 0 \text{ at } r = 0 \tag{7}$$

$$V_z = 0 \text{ at } r = R_c \tag{8}$$

where R_c is the called the capillary radius, depicted in Figure 4.1. Applying the two boundary conditions results in the following equation for the velocity of liquid moving through the tube as a function of the distance from the center of the tube:

$$V_z = \frac{1}{4\mu}\frac{dP}{dz}\left[r^2 - R_c^{\,2}\right] \tag{9}$$

Since the pressure gradient is constant, we have $dP/dz = -\Delta P/L$ where ΔP is the pressure difference over the distance traveled by the fluid in the tube (L). Finally, the volumetric flow rate of the liquid through the tube, Q, is given by

$$Q = \int_0^{R_c} V_z(2\pi r dr) = -\frac{2\pi\Delta P}{4\mu L}\int_0^{R_c}(r^2 - R_c^{\,2})r dr \tag{10}$$

where $2\pi r dr$ is the cross-sectional area element and the integral is computed from the center to the wall of the tube. Completing the integration yields

$$Q = \frac{\pi \Delta P R_c^{\,4}}{8 \mu L} \tag{11}$$

Equation (11), also known as the Hagen-Poiseuille equation or Poiseuille's equation, is a physical law that applies to both Newtonian liquids and gases.

4.2.2 The Washburn Equation for Flow in Porous Media

The Washburn equation, or the Lucas-Washburn equation, based on the Hagen-Poiseuille equation and its assumptions, has been applied to model capillary-driven flows in porous media, including paper [86,87]. This section reviews the derivation of the Washburn equation and its adaption for porous media. First, the system is modeled as a tube with one end connected to a liquid reservoir and the other end open to the atmosphere. Washburn focuses on the small capillaries that satisfy laminar flow conditions and starts with Poiseuille's Law as follows:

$$dV = \frac{\pi \Delta P}{8 \mu L} (R_c^{\,4} + 4 \varepsilon R_c^{\,3}) dt \tag{12}$$

where dV is the volume of the liquid that flows through the given cross-section of the capillary in time dt, L is the distance the liquid flowed in the capillary, ΔP is the pressure drop across the given length, μ is the fluid viscosity, and ε is the slip coefficient. Note that the slip coefficient arises from the general case in which the no-slip boundary condition is not applicable. Shortly before the time of Washburn's initial 1921 publication, the concept of slip was a highly discussed topic, however, in the present time it is generally accepted that a fluid under laminar flow will have zero velocity relative to the boundary at the solid-liquid boundary. When the no-slip condition can be applied to practically the entire region of flow, the slip coefficient term will become zero as addressed later in the derivation. At the end of a time period t the fluid will have

moved a distance L and the moving velocity is described as dL/dt. The volume term is also expressed as

$$dV = \pi R_c^{\,2} dz \tag{13}$$

Substituting Eq. (13) into Eq. (12) results in the following expression for the moving velocity

$$\frac{dL}{dt} = \frac{\Delta P}{8R_c^{\,2}\mu L}(R_c^{\,4} + 4\varepsilon R_c^{\,3}) \tag{14}$$

The total net pressure consists of the atmospheric, hydrostatic, and capillary pressure (determined from the Young-Laplace equation, Eq. (15)) which is then substituted into Eq. (14) to yield Eq. (16)

$$P_{capillary} = \frac{2\gamma}{R_c}\cos(\theta) \tag{15}$$

$$\frac{dL}{dt} = \frac{\left[P_{atm} + \rho g(h - l_s \sin(\varphi)) + \frac{2\gamma}{R_c}\cos(\theta)\right]}{8R_c^{\,2}\mu L}(R_c^{\,4} + 4\varepsilon R_c^{\,3}) \tag{16}$$

Here, P_{atm} is the atmospheric pressure, ρ is the liquid density, g is the gravitational constant, γ is the liquid-air surface tension, θ is the contact angle, h is the height of the liquid, φ is the angle depicted in Figure 4.2, and l_s is the linear distance of the fluid traveled assuming no winding of the capillary (as illustrated in Figure 4.2). Assuming that φ, θ, and ε are constants, the capillary is considered unwinding and $l_s = L$. Equation (16) can be integrated using substitution and the initial condition that at $t = 0,\ L = 0$ results in the following expression:

$$\frac{(\rho g \sin(\varphi))(R_c^{\,2} + 4\varepsilon R_c)}{8\mu} t + L = \frac{-\left[P_{atm} + \rho g h + \frac{2\gamma}{R_c}\cos(\theta)\right]}{\rho g \sin(\varphi)} \ln\left[\frac{P_{atm} + \rho g (h - L\sin(\varphi)) + \frac{2\gamma}{R_c}\cos(\theta)}{P_{atm} + \rho g h + \frac{2\gamma}{R_c}\cos(\theta)}\right]$$

(17)

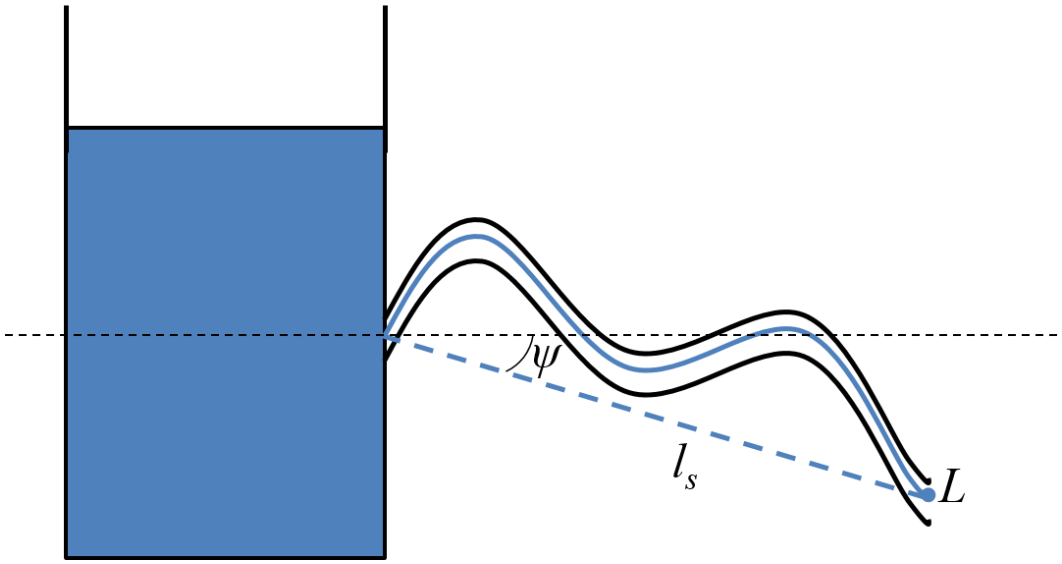

Figure 4.2 Example of the capillary tube from the Washburn model. *L* is defined as the actual distance traveled by the fluid (solid blue line) and l_s is defined as the linear distance traveled, or the shortest distance between the beginning end of the capillary and the leading fluid front (dashed blue line).

At this point, two limiting cases corresponding to $\varphi = 90°$ (vertical tube) and $\varphi = 0°$ (horizontal tube) are discussed.

Case 1: Vertical Flow

In the vertical flow case, $\varphi = 90°$. Furthermore, $\varepsilon = 0$ as the no-slip condition applies. Also, in the case of flow that is driven under capillary pressure in small capillary tubes, the atmospheric and hydrostatic pressures are negligible compared to the capillary pressure (i.e., $P_{atm} + \rho g(h - L) \approx 2\gamma\cos(\theta)/R_c$). These approximations simplify Eq. (17) to

$$\frac{(\rho g R_c^{\,2})}{8\mu} t + L = \frac{-\left[\frac{2\gamma}{R_c}\cos(\theta)\right]}{\rho g} \ln\left[1 - \frac{\rho g L}{\frac{2\gamma}{R_c}\cos(\theta)}\right] \tag{18}$$

Note that $\rho g L \ll 2\gamma\cos(\theta)/R_c$ also holds for a reasonable γ with a small capillary radius (R_c), as the gravitational term is relatively small. A Taylor series expansion of the logarithmic term can then be performed about $\rho g L / (2\gamma\cos(\theta)/R_c) \approx 0$. This yields:

$$\frac{(\rho g R_c^{\,2})}{8\mu} t + L = \frac{-\left[\frac{2\gamma}{R_c}\cos(\theta)\right]}{\rho g} \left[-\frac{\rho g L}{\frac{2\gamma}{R_c}\cos(\theta)} - \frac{\rho^2 g^2 L^2}{2\left(\frac{2\gamma}{R_c}\cos(\theta)\right)^2}\right] \tag{19}$$

Simplifying Eq. (19) results in

$$L^2 = \frac{\gamma R_c \cos(\theta) t}{2\mu} \tag{20}$$

where L is the distance moved by the fluid front, t is time, D is the average hydraulic pore diameter, γ is the surface tension, and μ is the fluid viscosity. This is the commonly used Washburn equation.

Case 2: Horizontal Flow

In the case when $\varphi = 0°$, we need to look back to Eq. (16) and rearrange the equation as follows

$$\frac{L}{\left[P_{atm} + \rho g(h - l_s \sin(\varphi)) + \frac{2\gamma}{R_c}\cos(\theta)\right]} dL = \frac{(R_c^{\,2} + 4\varepsilon R_c)}{8\mu} dt \tag{21}$$

Here, we can apply $\varphi = 0°$, $\varepsilon = 0$ (no-slip condition applies), and use the assumption that atmospheric and hydrostatic pressures are again negligible compared to the capillary pressure (i.e., $P_{atm} + \rho g(h-L) \approx 2\gamma\cos(\theta)/R_c$).

$$\frac{L}{\left[\frac{2\gamma}{R_c}\cos(\theta)\right]}dL = \frac{R_c^{\,2}}{8\mu}dt \tag{22}$$

Integrating both sides of Eq. (22) and using the initial condition at $t = 0,\ L = 0$, we again obtain the Washburn equation as shown in Eq. (20).

4.2.3 Flow of Non-Newtonian Fluids in Circular Tubes

While the Washburn equation assumes Newtonian fluid flow, the solutions we intend to study may not always demonstrate Newtonian behavior. To predict the dynamics of such fluids, the constitutive model for fluid viscosity is changed to the power law model introduced by Ostwald and de Waele [88,89], which is given below for cylindrical coordinates:

$$\mu_{eff} = k\left(\frac{dV_z}{dr}\right)^{n-1} \tag{23}$$

where μ_{eff} is the effective viscosity, k is the flow consistency index, and n is the flow behavior index. The power law model is a simple and useful relationship that approximately describes the behavior of non-Newtonian fluids within a given range of shear rates. Values of $n < 1$ represent shear-thinning (pseudoplastic) fluids, while values of $n > 1$ represent shear-thickening (dilatant) fluids. When $n = 1$, the Newtonian model is recovered, with k being equal to the viscosity coefficient μ.

The following is a summarized derivation of the application of the Washburn equation to power law fluids [90–92]. Assumptions used in the derivation include:

- Uniform capillary radius
- Gravitational effects are disregarded under horizontal flow and for small vertical capillaries
- The fluid is incompressible
- Flow is fully developed, laminar, and unidirectional

The procedure for the solution of elementary flow problems for power law fluids is very similar to that for Newtonian fluids, but with the added complexity introduced by the power law stress-strain relationship [93]. We start with Eq. (4) and integrate once to give:

$$\tau_{rz} = \frac{1}{2}\frac{dP}{dz}r + \frac{B_1}{r} \tag{24}$$

where B_1 is a constant of integration. Using the boundary condition at $r = 0$, τ_{rz} is finite, we see that B_1 has to be zero since one does not expect an infinite shear stress at the axis of the tube.

$$\tau_{rz} = \frac{1}{2}\frac{dP}{dz}r \tag{25}$$

Subsequently, we use the power law-modified equation for shear stress, which is given by substituting Eq. (23) into Eq. (5) in place of the viscosity term. Thus, we obtain

$$\tau_{rz} = k\left(\frac{dV_z}{dr}\right)^n \tag{26}$$

which is then equated to Eq. (25). Rearranging for the velocity gradient, taking the *n*th root of both sides and integrating the first-order derivative gives

$$V_z = \left(\frac{1}{2k}\frac{dP}{dz}\right)^{1/n} \frac{r^{(1/n)+1}}{(1/n)+1} + B_2 \tag{27}$$

in which B_2 is a constant of integration. Using the no-slip boundary condition that $V_z = 0$ at $r = R_c$ results in the final expression for the velocity profile:

$$V_z = \left(\frac{1}{2k}\frac{dP}{dz}\right)^{1/n} \frac{1}{(1/n)+1}\left[r^{1/n+1} - R_c^{\,1/n+1}\right] \tag{28}$$

Note that an alternative method is to integrate twice to obtain the velocity gradient expression with two constants of integration. Using the maximum velocity at boundary condition at $r = 0$ and the no-slip boundary condition, as mentioned in Eqs. (7) and (8) in the above Hagen-Poiseuille derivation, will produce the same result as Eq. (28). The volumetric flow rate is then given as

$$\begin{aligned} Q &= \int_0^{R_c} V_z (2\pi r dr) \\ Q &= \frac{2\pi}{1/n+1}\left(\frac{1}{2k}\frac{dP}{dz}\right)^{1/n} \int_0^{R_c} (r^{1/n+1} - R_c^{\,1/n+1}) r dr \\ Q &= \frac{\pi R_c^{\,3}}{3+1/n}\left(-\frac{R_c}{2k}\frac{dP}{dz}\right)^{1/n} \end{aligned} \tag{29}$$

In the integrations above, the pressure gradient was again treated as constant due to assuming fully developed flow in a cylindrical tube. Moreover, since the pressure gradient is a constant, $dP/dz = -\Delta P/L$ where ΔP is the pressure difference and L is the distance traveled by the fluid

in the tube. Since the moving velocity $dL/dt = Q/(\pi R_c^2)$, substituting this expression into Eq. (29) results in the following equation for the moving velocity:

$$\frac{dL}{dt} = \frac{R_c}{3+1/n}\left(\frac{R_c}{2k}\frac{\Delta P}{L}\right)^{1/n} \tag{30}$$

Neglecting gravitational effects, only the capillary pressure remains, therefore $\Delta P = P_{capillary}$ as described in Eq. (15). Adding this substitution results in Eq. (31), which is then rearranged to Eq. (32):

$$\frac{dL}{dt} = \frac{R_c}{3+1/n}\left(\frac{R_c}{2k}\frac{2\gamma\cos(\theta)}{R_c L}\right)^{1/n} \tag{31}$$

$$L^{1/n}dL = \frac{R_c}{3+1/n}\left(\frac{2\gamma\cos(\theta)}{k}\right)^{1/n} dt \tag{32}$$

Integration of Eq. (32) with the initial condition at $t = 0,\ L = 0$ results in Eq. (33), which is the Washburn equation expanded to power law fluids.

$$L = \left[\left(\frac{n+1}{3n+1}\right)\left(\frac{\gamma\cos(\theta)}{k}\right)^{1/n} R_c t\right]^{\frac{n}{n+1}} \tag{33}$$

This expression matches what has been reported in the literature [90]. In addition, if $n = 1$ and $k \equiv \mu$, Eq. (33) returns the classical Washburn equation for Newtonian fluids. Within this study, we first use the Washburn model for Newtonian fluids to describe ATPS phase flow, and then evaluate the use of the model modified for power law fluids.

4.3 Materials and Methods

4.3.1 ATPS Preparation and Bulk Phase Extraction

All ATPSs were prepared using component concentrations that produced a 1:1 equilibrium volume ratio at 25 ℃. To prepare the PEG-salt ATPS, polyethylene glycol 8000 (PEG 8000) (VWR, PA, USA) and potassium phosphate (in a dibasic:monobasic mass ratio of 5:1) were dissolved in Dulbecco's phosphate-buffered saline (PBS, pH 7.4, containing 1.47 mM KH_2PO_4, 8.10 mM Na_2HPO_4, 138 mM NaCl, 2.67 mM KCl, and 0.495 mM $MgCl_2$) (Invitrogen, CA, USA). The final concentrations of the components were 12.5% w/w PEG and 7.5% w/w potassium phosphate. To prepare the Triton X-114 ATPS, Triton X-114 was dissolved in PBS to a final concentration of 4% w/w. To prepare the PEG-Dextran ATPS, PEG 8000 and dextran (MW 6000) were dissolved in PBS to final concentrations of 7% w/w PEG and 17% w/w dextran. The PEG-polyacrylic acid (PAA) ATPS was prepared with PEG 8000 and sodium polyacrylate (Polysciences, PA, USA) dissolved in PBS to final concentrations of 15% w/w PEG and 14.3% w/w PAA. All reagents were purchased from Sigma Aldrich unless otherwise stated. Each solution was vortexed and allowed to phase separate overnight. After phase separation was completed, the solution was centrifuged for 5 min at 2000 rpm, and the immiscible coexisting phases were extracted via syringes and collected in separate tubes for characterization.

4.3.2 Nanoparticle Synthesis

BSA-coated gold nanoparticles (BSA-GNs) were synthesized in the same manner previously mentioned in Chapter 2. PAA-coated iron oxide nanoparticles were produced in the following manner. 100 mL of 1 M NaOH was prepared and stirred under nitrogen gas. 10 mL of a 1:2 molar ratio of $FeCl_2/FeCl_3$ was then added dropwise. After mixing for 2 hours, the iron oxide nanoparticles (IONPs) were then separated using a magnet and centrifuged for 15 min at

3500 rpm. To coat the IONPs with PAA, the IONP suspension was first sonicated. Then 5 mL of 0.1% (w/w) PAA solution in water was added to the suspension, which was then sonicated again for 8 minutes to produce PAA-coated IONPs.

4.3.3 Imbibition Experiments

Imbibition experiments were conducted to measure the flow speeds of each of the bulk ATPS phases through fiberglass paper (Whatman Inc, GE Healthcare Bio-Sciences, PA, USA). The paper was cut into 0.5 cm × 7 cm strips and marked with a pen every 0.5 cm along the length of the strip. An ambient temperature of 25 ± 0.5 ℃ and humidity of 49% ± 2% were maintained throughout the experiments in this study. To minimize evaporation effects, the paper strips were placed in a casing consisting of glass slides and adhesive tape (Lohmann Technologies, KY, USA). The casing was designed with a 0.5 cm wide slit through which the paper strips could be inserted. The glass cover of the casing enabled clear visualization of the imbibition process and was treated with Sigmacote to prevent fluid absorption onto the glass. A 10 cm Petri dish was filled with 2 mL of the extracted bulk phase and 2 µL of Brilliant Blue FCF dye (The Kroger Co., Cincinnati, OH). The dye was added to help visualize the advancing fluid through the paper strip. For vertical flow measurements, the paper strip and casing was dipped into the Petri dish that was lightly mixed with a micro stir bar. For horizontal (lateral) flow measurements, 2 mL of the extracted phase fluid (which also contained 2 µL of Brilliant Blue FCF dye) was held in a plastic case. The paper strip and casing were inserted horizontally across the plastic case until the paper strip made contact with the fluid (Figure 4.3). The wicking process was recorded using a Canon PowerShot SX200 IS video camera (Canon, Tokyo, Japan). Experiments were performed in triplicate and time points were determined with Windows Movie Editor.

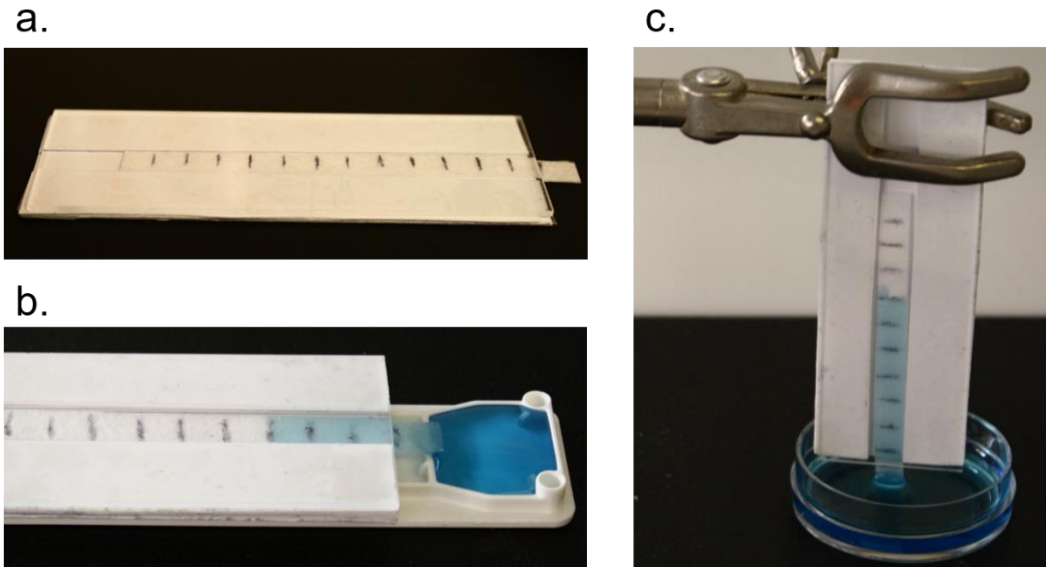

Figure 4.3 (a.) Paper strips enclosed in a casing consisting of a Sigmacote-treated glass slide and adhesive membrane. Paper strip wicking from reservoir during experimentation for (b.) horizontal flow and (c.) vertical flow.

4.3.4 Bulk Phase Characterization

Wilhelmy plate surface tension measurements of each of the bulk phases were collected using the Krüss K100 force tensiometer (Krüss USA, NC, USA) at 25 ℃. A standard platinum plate attached to the tensiometer was used. Measurements were taken in triplicate. The surface tensions of PBS and deionized water were also measured as controls. Sessile drop contact angle measurements on the fiberglass paper substrate were taken using a goniometer and video capturing software. Viscosity measurements were acquired using a Brookfield LVDV-I Prime digital viscometer (AMETEK Brookfield, MA, USA). Viscosity measurements were performed in triplicate and averaged.

4.3.5 Hydrogel Synthesis

Microporous polyethylene glycol dimethacrylate (PEGDMA) hydrogels were synthesized using the salt-leaching method. Briefly, a 70% (w/w) solution of PEGDMA (Mw 750) in a saturated NaCl solution was prepared. This solution was then centrifuged for 10 min at 2,000

rpm to separate any precipitated salt from the rest of the PEGDMA solution. The supernatant was then extracted and was used as the precursor solution for the hydrogels. NaCl crystals in the size range of approximately 45 μm were prepared with a mortar and pestle and sieve. 0.5 g of salt crystals were added to every 1 mL of PEGDMA solution, followed by 1 μL of 20% (w/v) Irgacure 2959 in 70% ethanol. The entire mixture was mixed and pipetted onto a Sigmacote-coated glass slide. A second Sigmacote-treated glass slide was placed on top of the solution with coverslips stacked to form spacers. The two glass slides were strongly held together by binder clips. The solution was treated with UV light at 3" distance for 10 min. The gel was then carefully removed from the mold and submerged in deionized water overnight to leach the salt crystals from the gel interior. The hydrogels were then removed, frozen at -80 °for 15 min, dried under low pressure in a lyophilizer for 10 min, and then dried further in ambient air conditions for 30 min, which caused the hydrogels to turn slightly white in color.

4.4 Results and Discussion

4.4.1 Imbibition Experiments with Paper

The results of the imbibition experiments for the ATPS bulk phases are shown in Figure 4.4. For the PEG-salt ATPS, the PEG-rich phase demonstrated significantly slower wicking speeds than the salt-rich phase, while for the Triton X-114 ATPS, the micelle-rich phase demonstrated significantly slower wicking speeds than the micelle-poor phase. These studies of the bulk phase speeds correlate with our empirical observations of ATPS phase separation in that the leading phase for each ATPS appears to be the faster flowing phase. Furthermore, there is a noticeable decrease in flow speed when the fluids flowed vertically up the paper strip rather than horizontally across the strip. While the original derivation suggests that the same Washburn equation is suitable for both vertical and horizontal flow, it is evident that this does not work well

with our experimental results. Although gravitational effects were neglected in the derivation for the vertical case, it is possible that they act to counter the capillary pressure and slow down fluid flow. Future studies may involve incorporating gravitational contributions to the vertical model to make it more accurately describe the experimental results. Regardless, the micelle-poor and salt-rich phases still demonstrated faster flow speeds relative to the micelle-rich and PEG-rich phases when flowing vertically, so this did not change which phase became the leading phase. From these observations, we thought that it is possible that detailed characterization and study of the bulk phases of a particular ATPS can be used to model and predict the leading phase in paper. The bulk phases for these two systems were then characterized for the parameters included in the Washburn equation.

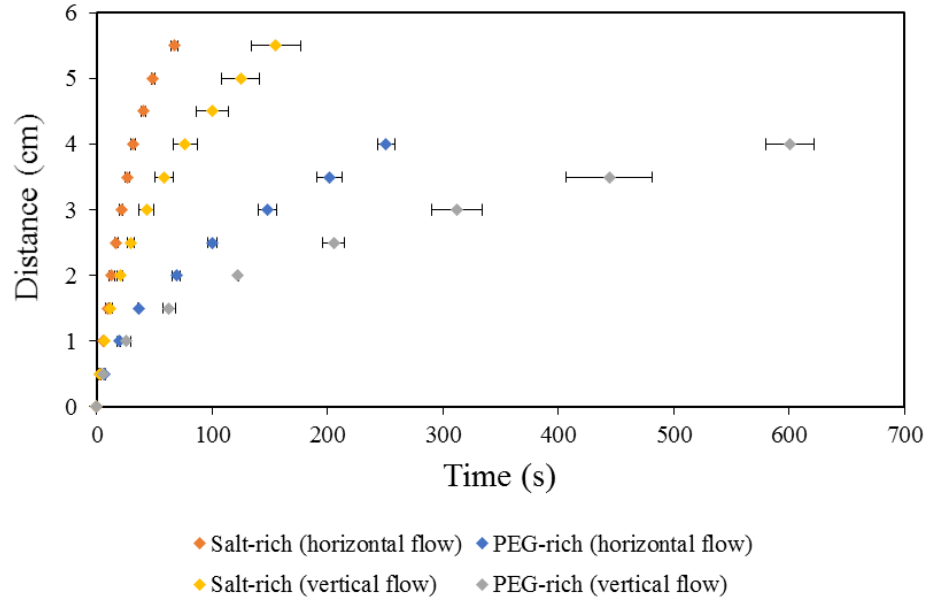

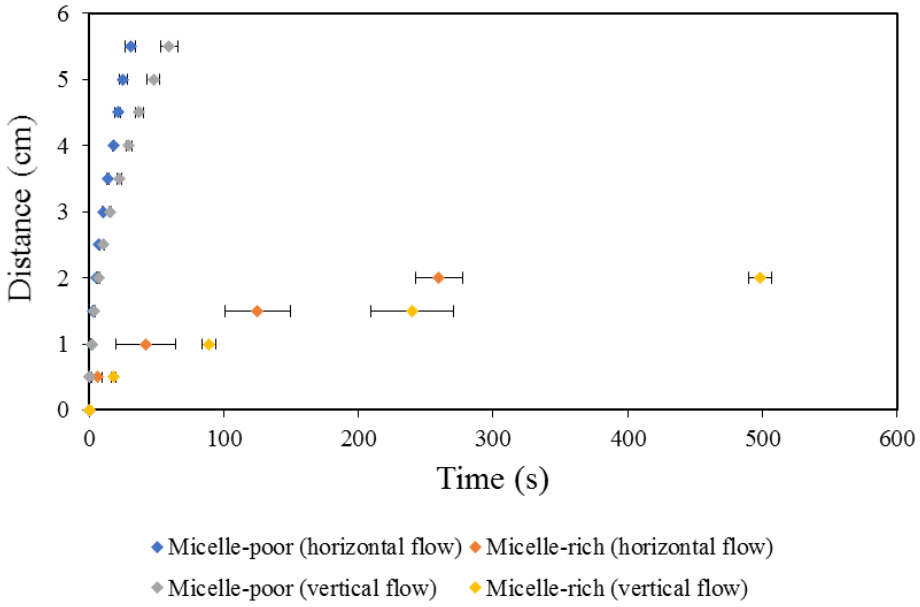

Figure 4.4 Experimental results for wicking of the PEG-salt bulk phases and Triton X-114 bulk phases in fiberglass paper. The horizontal flow orientation is compared to the vertical orientation.

4.4.2 Properties of the Extracted Bulk Phases

Surface tension, contact angle, and viscosity measurements were collected for each of the bulk phases of the PEG-salt and Triton X-114 ATPSs. The results are listed in Table 4.1. All phases were found to completely wet the fiberglass paper during sessile drop experiments, producing no measurable static contact angle. Therefore, we made the assumption that $\theta \approx 0^{\circ}$ for all phases tested.

Table 4.1 Experimental surface tension, viscosity, and static contact angle measurements of PEG-salt and Triton X-114 ATPS bulk phases.

Bulk Phase	Surface Tension ($mN\ m^{-1}$)	Viscosity (cP)	Static contact angle on paper (°)
Salt-rich phase	57.47 ± 0.03	1.83 ± 0.03	~ 0
PEG-rich phase	55.34 ± 0.09	23.88 ± 1.29	~ 0
Micelle-poor phase	29.99 ± 0.01	1.55 ± 0.04	~ 0
Micelle-rich phase	29.97 ± 0.01	120.67 ± 0.47	~ 0

The surface tensions of the deionized water and PBS controls were 72.07 ± 0.02 mN m^{-1} and 68.22 ± 0.01 mN m^{-1}, respectively. The surface tension of the salt-rich phase of the PEG-salt system was found to be lower (57.47 ± 0.03 mN m^{-1}) compared to that of the PBS control, and quite comparable to that of the PEG-rich phase (55.34 ± 0.09 mN m^{-1}). While the lowered surface tension of the PEG-rich phase can be attributed to the presence of PEG at the surface, we speculate that the decrease in surface tension of the salt-rich phase can be explained by the presence of the additional phosphate ions added to the PBS. In general, the lowering of surface tension by salt depends on the nature of the salt ions, specifically their size and charge density. Smaller ions with high charge density, such as Na^{+} and Cl^{-}, can become highly hydrated as they increase the organization of water molecules by tightly noncovalently binding the water around themselves. The electrostatic interactions formed between water and the salt ions are stronger

than the hydrogen bonds formed between water molecules. The intermolecular bonds formed in the bulk solution increase, and as a result the surface tension increases. On the other hand, larger ions with low charge density become less hydrated as the electrostatic interactions between the water and salt ion are weaker than the hydrogen bonds between water molecules. The ions become highly polarizable and move to the surface. The penalty for moving a water molecule to the surface therefore decreases, leading to a decrease in surface tension. The effect of phosphate ions on surface tension ultimately depends on the pH of the buffered solution and the proportion of the various dissociated forms of the phosphate ion. At pH 7.4, phosphate ions exist as 39% $H_2PO_4^-$ which is a relatively polarizable species capable of decreasing the liquid surface tension. The surface tension measurements for the micelle-poor and micelle-rich phases were also very similar. This makes sense as both phases contain Triton X-114 at concentrations above the surfactant's critical micelle concentration (CMC). Above the CMC, the water-air interface becomes saturated with surfactant, and further addition of surfactant goes toward adding to or creating micelles. Therefore, the surface tension is expected to remain relatively constant.

In both the PEG-salt and Triton X-114 ATPS, the viscosities between the two phases were found to differ greatly. The salt-rich phase had a measured viscosity of 1.83 ±0.03 cP while the PEG-rich phase had a measured viscosity of 23.88 ± 1.29 cP (an approximately 13.1-fold difference in viscosity between the two phases). For the Triton X-114 ATPS, the micelle-poor phase had a measured viscosity of 1.55 ±0.04 cP while the micelle-rich phase had a measured viscosity of 120.67 ±0.47 cP (an approximately 77.9-fold viscosity difference). These significant differences arise from the greater concentration of polymer or overall surfactant that exist in the more viscous phases, and correlate with the slower flow speeds observed in imbibition. From this data, we conclude that of the measured factors, fluid viscosity plays a

dominant role in deciding which phase is the leading phase, while surface tension and static contact angle appear to provide minimal effects as the differences between the two phases are small.

From a mechanistic viewpoint, it is reasonable to assume that viscosity differences will play a role in enhancing phase separation. We hypothesize that in the case of paper-based separation, the highly porous structure of the paper is able to accelerate the coalescence of domains based on these viscosity differences. For example, the Triton X-114 system has a micelle-rich phase that has a greater viscosity than the micelle-poor phase, and this viscosity difference is present at the scale of domains that are formed at the onset of phase separation. As a mixed solution is initially added to the paper, viscous micelle-rich domains that form would become held back by these porous structures while less viscous micelle-poor domains flow through the pores more easily. Therefore, micelle-rich domains have a greater likelihood of contacting and coalescing with other micelle-rich domains that are held back in the fluid flow. Likewise, the faster-flowing micelle-poor domains also coalesce more easily at the fluid front. This accelerates the formation of the resulting phases on a macroscopic level. Furthermore, a minimum difference in domain viscosities is necessary for this effect to be seen at this macroscopic level.

4.4.3 Incorporating Adjustments for Non-Newtonian Fluids

However, the viscosity differences between the two phases in the studied systems are relatively large, and since the Washburn equation assumes the fluids are Newtonian, it was important to check for any potential non-Newtonian behavior. This non-Newtonian behavior will more likely arise in the more viscous phases rather than the less viscous phases due to the higher polymer or surfactant content within these phases. Polymer and surfactant solutions above

certain concentrations will generally exhibit shear-thinning behavior [87,94–96]. We used the cone-plate viscometer to vary the shear rate and measure the change in shear stress for the micelle-rich phase and the PEG-rich phase. The data was then fitted to a power function to calculate the experimental flow behavior index (n) of these particular phases according to Eq. (26). The results for the PEG-rich and micelle-rich phases are shown in Table 4.2. Both phases returned n values less than 1, which is in agreement with the shear-thinning behavior of such solutions.

Table 4.2 Values of *n* for viscous phases calculated from viscometer experiments.

Bulk Phase	PEG-rich	Micelle-rich
n	0.874	0.876
Characteristic	Shear-thinning	Shear-thinning

Because the flow behavior indices differed from 1, we then needed to make adjustments to the Washburn model to account for the potential non-Newtonian behavior. We decided to relax the assumption of Newtonian fluids in our model, and we utilized the power law-modified Washburn equation, derived above as Eq. (33), to describe the micelle-rich and PEG-rich phases. The original equation was used to describe the salt-rich and micelle-poor phases. To verify whether the Washburn model is suitable in describing the experimental results, the imbibition data of the less viscous phases was plotted with the distance L vs. the square root of time t, and linear regression was performed. Similarly, to verify the modified Washburn model, the imbibition data of the more viscous phases was plotted with the distance L vs. t raised to the power of $n/(n+1)$, followed by linear regression. As shown in Figure 4.5, the data for all phases measured provided excellent R-squared values which confirm Washburn-like behavior,

and also confirm that the power law adjustments to the Washburn model also accurately reflected the experimental results.

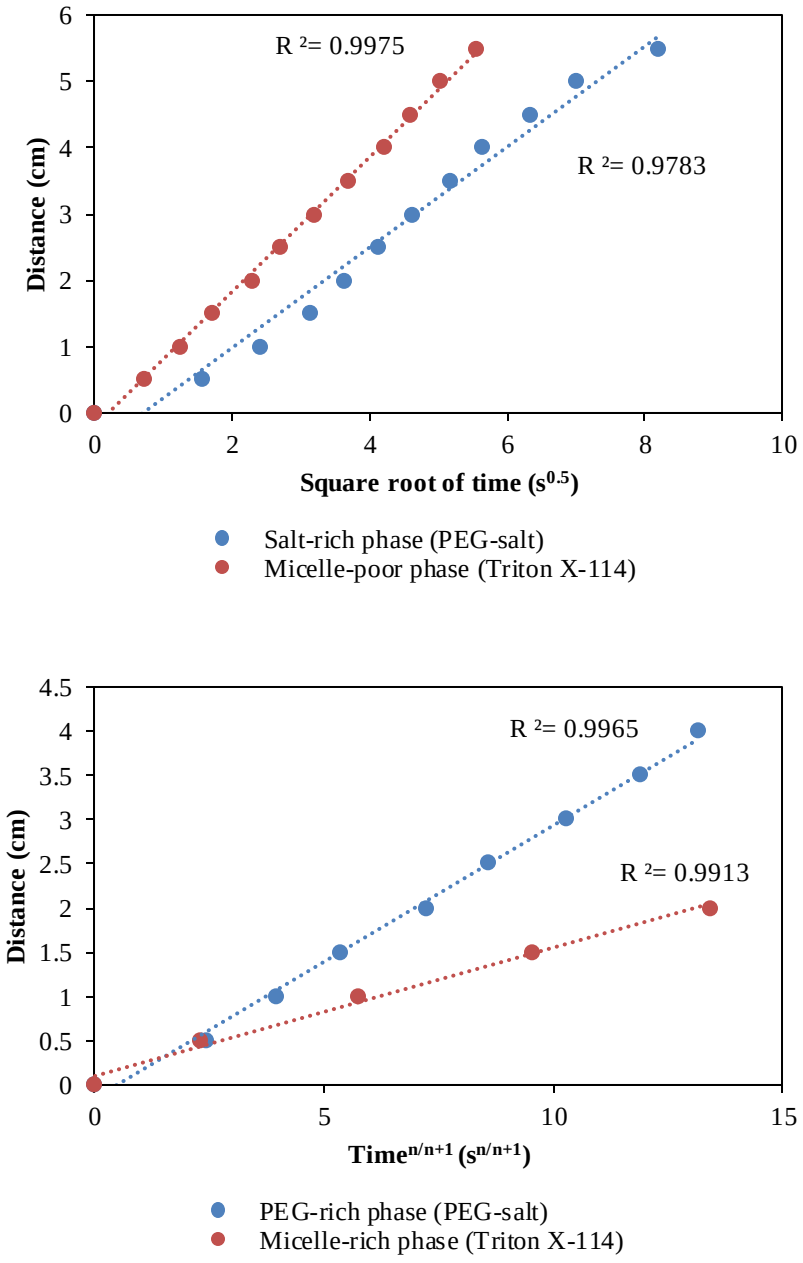

Figure 4.5 Linear regression demonstrates the validity of the Washburn equation in describing the experimental studies for the imbibition of the less viscous phases (top). Linear regression also demonstrated the validity of the power law-modified Washburn equation for describing imbibition of the more viscous phases (bottom).

One major limitation of the Washburn equation for applications to paper is that the average pore size is very difficult to measure. As fiberglass consists of non-interconnected fibers rather than a completely linked network, the capillary tube assumption in the Washburn equation is not entirely appropriate. Despite this limitation, it has been utilized for a variety of paper imbibition experiments with acceptable accuracy, with the average pore size of the paper typically measured indirectly as a result. However, there is a lack of studies in the literature that describe wicking in fiberglass paper, as most of the studies utilize cellulose or nitrocellulose-based materials. According to the Washburn equation, the slopes calculated from each phase would equal $\gamma R_c \cos(\theta)/2\mu$, and therefore, the slopes can be used to calculate the pore diameter, equivalent to $2R_c$. For the power law-modified Washburn equation, nonlinear least-squares regression was conducted to calculate the pore diameter. To simplify the analysis, we assumed that the capillary pore size does not change after imbibition. The results are shown in **Error! eference source not found.**. The pore diameter calculated from the PEG-rich data (7.7 μm) closely matches the pore diameter calculated from the salt-rich data (6.4 μm). Similarly, the pore diameter calculated from the micelle-rich data (22.4 μm) is similar to the pore diameter calculated from the micelle-poor data (20.6 μm).

Table 4.3 Comparison of the calculated pore diameters from the original Washburn equation and the power law-modified equation for the PEG-rich and micelle-rich phases. Values from the power law-modified Washburn equation are shown to be similar to the values generated for the salt-rich and micelle-poor phases (which are assumed to be Newtonian).

PEG-salt ATPS Bulk Phase	Salt-rich (original equation)	PEG-rich (power-law)
Washburn Diameter (μm)	6.4	7.7
Triton X-114 ATPS Bulk Phase	Micelle-poor (original equation)	Micelle-rich (power-law)
Washburn Diameter (μm)	20.6	22.4

We noticed that within a given ATPS, there was slight variation between the calculated capillary pore diameters of the two phases. Possible factors that contribute to the variation include small differences in wettability between the two phases or from differences in fiber swelling. Pore-scale swelling of the glass fibers changes the structure and molecular arrangement of the material, which affects the wettability and wicking properties of the material. Since we expect the two phases to effect paper swelling to different extents, we would expect some variation in the experimentally determined average pore sizes in the imbibition experiments. We also noticed that the less viscous phase has the smaller pore diameter, despite having the faster wicking velocity. Here, the difference can be attributed to the dominant influence of the phase viscosity as shown in Eq. (20). Considering these slight variations, it should be noted that the pore sizes are only approximate estimates. Despite this consideration, the calculated pore diameters still appear reasonable as typical listed pore sizes of fibrous paper fall within the 10-100 μm size range. Altogether, the results suggest that the Washburn equation and its modifications are suitable for modeling the flow of bulk phases of two-phase systems within fiberglass paper.

4.4.4 Predicting Phase Separation Ability of a Polymer-Polymer ATPSs

Encouraged by the above results, we next aimed to apply our theoretical framework to predict the phase separation of the PEG-Dextran and PEG-PAA polymer-polymer systems in paper. Both systems produce phases enriched in a particular polymer. In a tube, the PEG-Dextran system produces a top PEG-rich phase and a bottom dextran-rich phase, while the PEG-PAA system produces a top PEG-rich phase and a bottom PAA-rich phase (Figure 4.6). Since the

previous experiments with the PEG-salt and Triton X-114 systems indicate that the contact angles and surface tensions are likely to be similar between the two phases, we focused on the difference in viscosities between the two phases of these new systems as the primary predictor of phase separation.

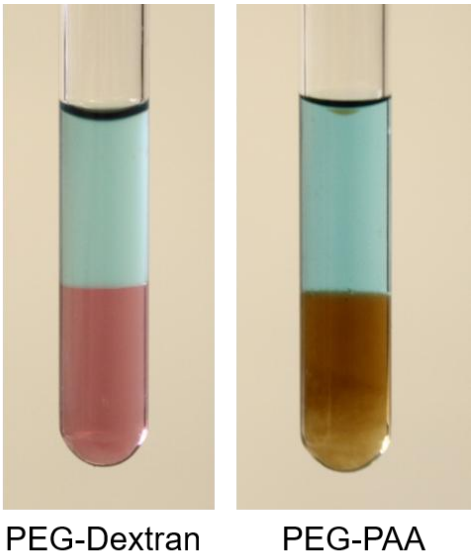

Figure 4.6 Images of phase-separated PEG-Dextran and PEG-PAA ATPSs in a test tube, with their appropriate colorimetric indicators for each phase. In the PEG-Dextran ATPS, red-colored BSA-GNs indicate the bottom dextran-rich phase and Brilliant Blue FCF dye indicates the top PEG-rich phase. In the PEG-PAA ATPS, brown-colored PAA-coated iron-oxide nanoparticles indicate the bottom PAA-rich phase and Brilliant Blue FCF indicates the top PEG-rich phase.

The measured viscosities of the individual phases are shown in Table 4.4. Within the PEG-Dextran system, the viscosities of the PEG-rich phase and dextran-rich phase were 11.3 cP and 12.7 cP, respectively. These values present a relatively small difference in viscosity, producing only a 1.1-fold difference between the two phases. On the other hand, within the PEG-PAA system the viscosity difference was larger as the PEG-rich phase viscosity was 47.1 cP and the PAA-rich phase was 15.6 cP (an approximately 3-fold difference).

Table 4.4 Measured viscosities of the PEG-Dextran and PEG-PAA phases.

Bulk Phase	Viscosity (cP)
Dextran-rich phase	12.7
PEG-rich phase (PEG-Dextran)	11.3
PAA-rich phase	15.6
PEG-rich phase (PEG-PAA)	47.1

Horizontal imbibition experiments were also performed for each of the bulk phases and the results are shown in Figure 4.7. There was a noticeable difference in wicking speeds of the PEG-PAA ATPS phases, however the difference was much less apparent for the PEG-dextran system phases.

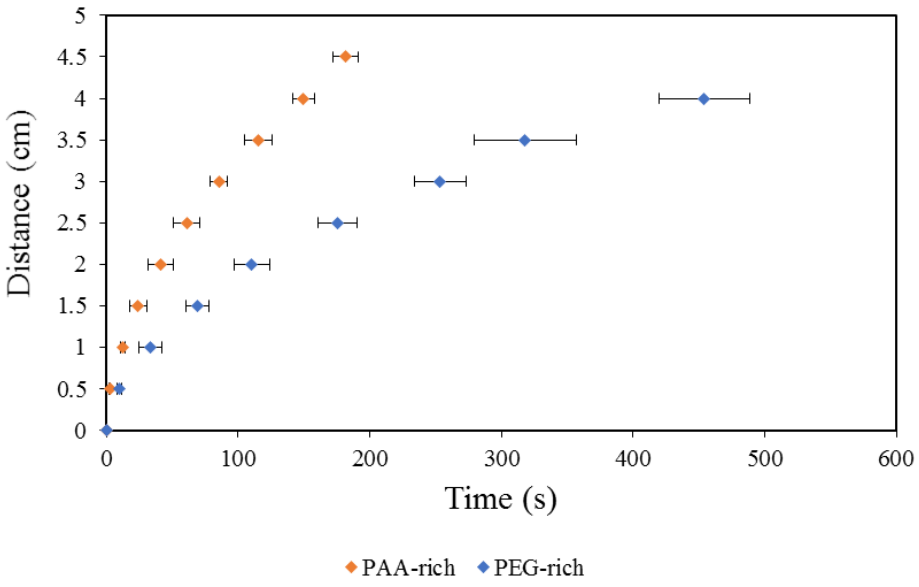

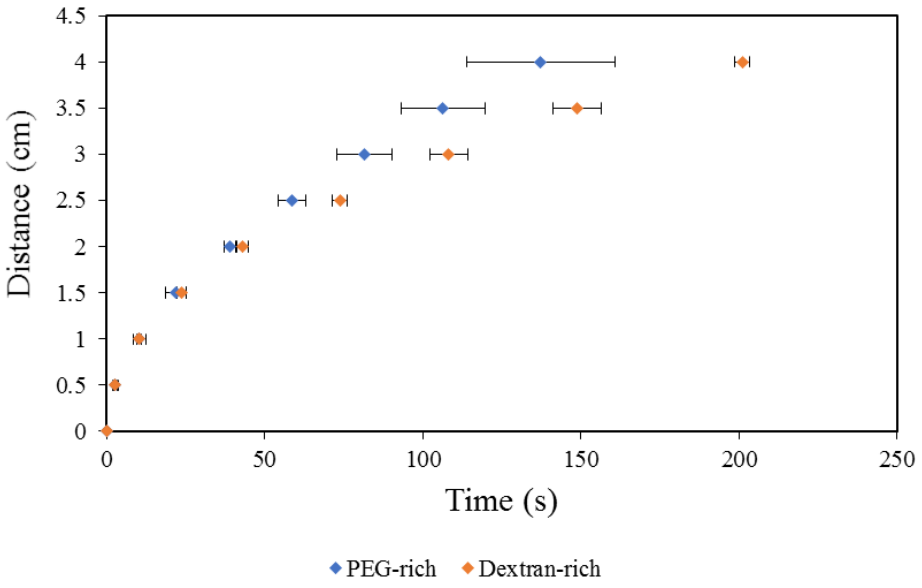

Figure 4.7 Imbibition plots for the PEG-Dextran and PEG-PAA phases on fiberglass paper.

Finally, the ATPSs were applied directly to a strip of fiberglass paper and the visual results are shown in Figure 4.8. There was no visible separation of the PEG-Dextran ATPS as the colorimetric indicators (red GNPs and Brilliant Blue FCF) blended together and appeared very diffuse. In contrast, there was noticeable phase separation of the PEG-PAA system as the leading PAA-rich phase was clearly marked by the concentrated PAA-coated iron oxide nanoparticles at the leading front of the fluid, and the PEG-rich phase, indicated by the Brilliant Blue FCF, lagged behind. Phase separation occurred within 2-3 minutes. As predicted, the larger viscosity difference between the phases of the PEG-PAA ATPS correlated with the system's ability to phase separate when applied to the paper strip. These results indicate that the viscosity difference between phases is a suitable to predict the phase separation abilities of these two-phase systems.

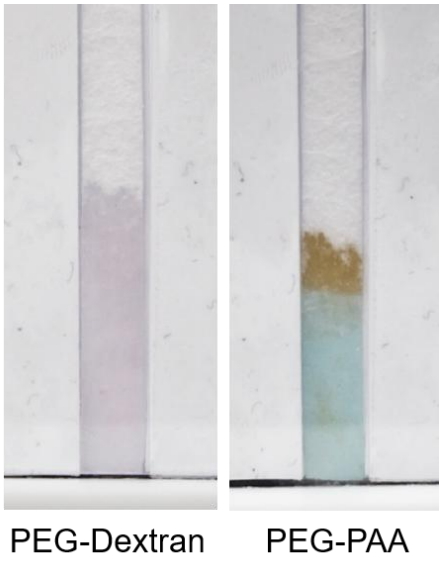

Figure 4.8 Visual results of PEG-Dextran and PEG-PAA ATPSs applied to paper. Visible phase separation is seen for the PEG-PAA ATPS but not seen for the PEG-Dextran ATPS.

4.4.5 Extending the Phase Separation Phenomenon to Hydrogels

After demonstrating that the Washburn equation and its parameters can be used to predict the phase separation of ATPSs on fiberglass paper, we next aimed to extend our established framework to predict phase separation in an entirely different type of porous medium. PEGDMA hydrogels served as our model hydrogel system as they are relatively easy to synthesize. Furthermore, their pore sizes can be tuned to the micrometer scale via methods such as salt-leaching. We made microporous PEGDMA hydrogels to allow for unhindered flow of the nanoparticles used as colorimetric indicators.

If we refer back to the Washburn equation parameters that were experimentally characterized, we note that viscosity and surface tension are parameters that describe the fluid, so the previously obtained values are still valid even when applied to a hydrogel system. Since the contact angle depends on the solid-liquid interfacial tension as well as the solid-air surface tension, we would expect these values to differ from those of the paper. Therefore, we conducted sessile drop measurements of the individual phases of the PEG-salt ATPS, the Triton X-114

ATPS, the PEG-Dextran ATPS, and the PEG-PAA ATPS on a dried PEGDMA scaffold. Since it was found that all the phases completely wetted the hydrogels, we made the same assumption that $\theta \approx 0^{\circ}$ for all phases tested on the hydrogel. Therefore, we still expected that the viscosity difference would be the dominant factor in determining the phase separation ability of these four ATPSs within hydrogels. Since the PEG-salt, Triton X-114, and PEG-PAA ATPSs demonstrated large enough differences in viscosity, we predicted that they too would separate in hydrogels based on this viscosity difference, while the PEG-Dextran ATPS would not separate based on its small phase viscosity difference.

Imbibition experiments were also conducted for each of the phases on the dried PEGDMA gels. As shown in Figure 4.9, there were noticeable differences in wicking speeds between the phases of the PEG-salt, Triton X-114, and PEG-PAA ATPSs, which were similar to that seen from the imbibition experiments on fiberglass paper. There was also no significant difference in wicking speeds of the PEG-Dextran ATPS phases, and therefore, the imbibition experiments further support the prediction that only the PEG-Dextran would not be able to separate in hydrogels.

PEG-salt ATPS

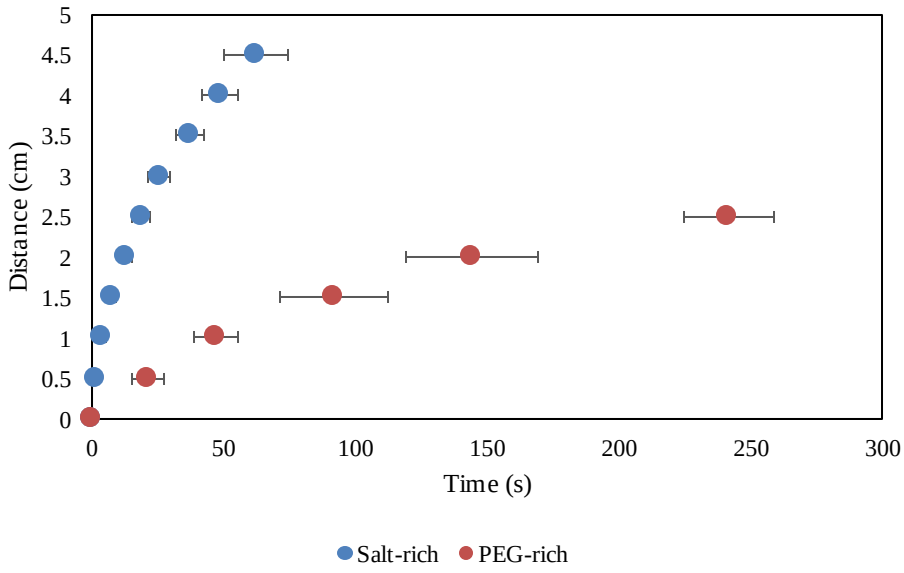

Triton X-114 ATPS

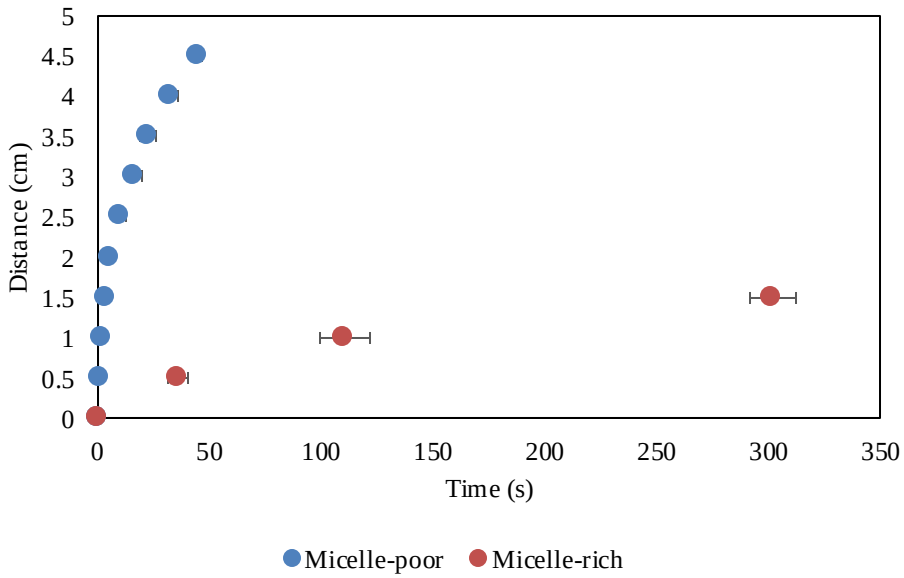

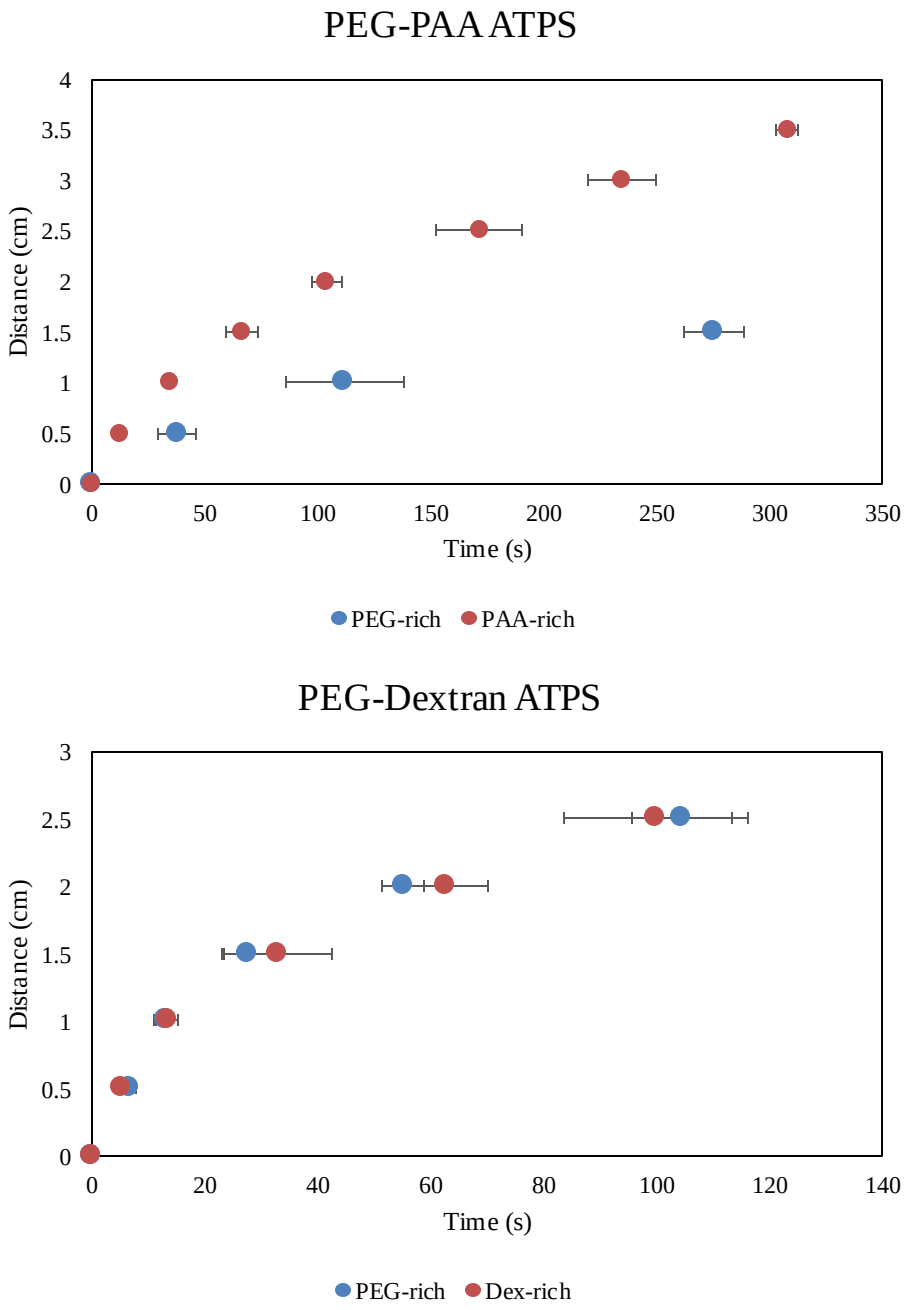

Figure 4.9 Imbibition plots for PEG-salt, Triton X-114, PEG-PAA, and PEG-Dextran ATPS phases on PEGDMA hydrogels.

The visual results from the application of the four ATPSs to the dried hydrogels are shown in Figure 4.10. As predicted, the PEG-salt, Triton X-114, and PEG-PAA ATPSs demonstrated successful phase separation within 2-3 minutes as the solutions wicked through the

hydrogels. Furthermore, we witnessed the same leading phases as seen in paper. These include the salt-rich phase (indicated by BSA-GNs), the micelle-poor phase (indicated by BSA-GNs), and the PAA-rich phase (indicated by PAA-coated IONPs). To our knowledge, this is the first time that hydrogels have been used to enhance the phase separation rate of ATPSs, demonstrating that the phenomenon is not simply restricted to paper-based materials. Furthermore, phase separation was not seen for the PEG-Dextran ATPS, which demonstrates that our theoretical framework can also be applied to successfully predict the phase separation ability and inability of various ATPSs within hydrogels, as well as within paper.

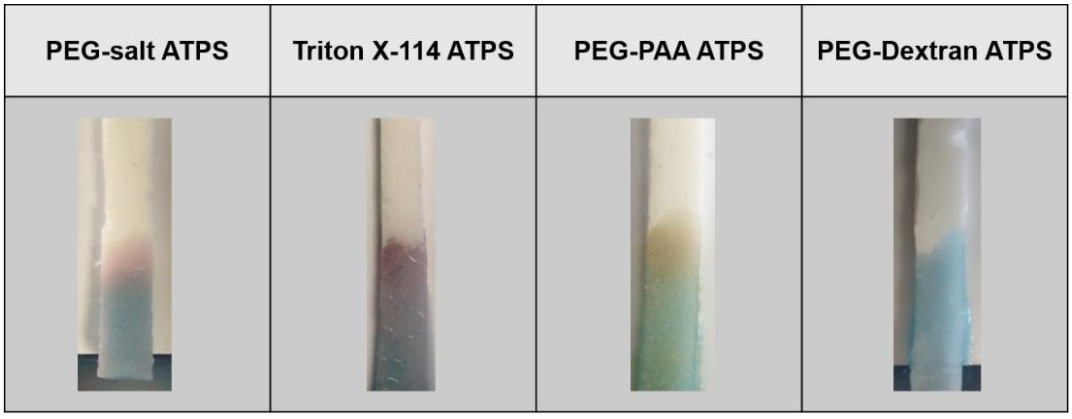

Figure 4.10 Phase separation of the PEG-salt, Triton X-114, and PEG-PAA ATPSs in hydrogels. Phase separation was witnessed within 2-3 minutes. As predicted, the PEG-Dextran ATPS was unable to phase separate.

4.4 Conclusions

In the current study, we developed a theoretical framework based on the Washburn equation to model and describe the phase separation of aqueous two-phase systems applied to paper membranes. By characterizing the viscosities, surface tensions, static contact angles, and wicking behavior of individual phases from the PEG-salt and the Triton X-114 ATPS, we found that the bulk phases exhibit classical Washburn behavior with adequate accuracy. Furthermore, we characterized the phases for the parameters in the Washburn model and identified phase viscosity as a dominant factor in determining the leading phase and lagging phase as confirmed

from our previous observations. Viscosity differences can therefore be used to predict if paper could enhance phase separation, and if so, which phase will constitute the leading phase. We then expanded the Washburn model and incorporated the power law model for fluids to account for non-Newtonian behavior in the more viscous phase, confirming the shear-thinning behavior expected of such polymer and surfactant solutions. By determining the flow behavior index of individual phases of a particular ATPS, we are able to quantitatively predict the flow behavior of the individual phases.

After establishing this framework by studying systems known to phase separate in paper, we then applied it to successfully predict the ability of the PEG-PAA polymer-polymer system to phase separate as well. In addition, we successfully predicted the inability of the PEG-Dextran polymer-polymer system to phase separate. Finally, we extended this framework to predict and demonstrate phase separation of ATPSs in PEGDMA hydrogels, demonstrating that the phase separation enhancement can potentially apply to porous media in general.

References

[1] P. Yager, G.J. Domingo, J. Gerdes, Point-of-care diagnostics for global health., Annu. Rev. Biomed. Eng. 10 (2008) 107–44.

[2] A.W. Martinez, S.T. Phillips, G.M. Whitesides, E. Carrilho, Diagnostics for the developing world: microfluidic paper-based analytical devices., Anal. Chem. 82 (2010) 3–10. doi:10.1021/ac9013989.

[3] T. Hänscheid, M.P. Grobusch, How useful is PCR in the diagnosis of malaria?, Trends Parasitol. 18 (2002) 395–398. doi:10.1016/S1471-4922(02)02348-6.

[4] R. Wong, H. Tse, Lateral Flow Immunoassay, Springer Science & Business Media, 2008. http://books.google.com/books?id=D4-capuCoRUC&pgis=1 (accessed July 17, 2014).

[5] C. Wongsrichanalai, M.J. Barcus, S. Muth, A. Sutamihardja, W.H. Wernsdorfer, A Review of Malaria Diagnostic Tools: Microscopy and Rapid Diagnostic Test (RDT), (n.d.). http://www.ncbi.nlm.nih.gov/books/NBK1695/ (accessed November 21, 2014).

[6] D. Payne, Use and limitations of light microscopy for diagnosing malaria at the primary health care level., Bull. World Health Organ. 66 (1988) 621–6. http://www.pubmedcentral.nih.gov/articlerender.fcgi?artid=2491188&tool=pmcentrez&rendertype=abstract (accessed August 24, 2015).

[7] G.A. Posthuma-Trumpie, J. Korf, A. van Amerongen, Lateral flow (immuno)assay: its strengths, weaknesses, opportunities and threats. A literature survey., Anal. Bioanal. Chem. 393 (2009) 569–82. doi:10.1007/s00216-008-2287-2.

[8] E. Fu, T. Liang, J. Houghtaling, S. Ramachandran, S.A. Ramsey, B. Lutz, P. Yager, Enhanced sensitivity of lateral flow tests using a two-dimensional paper network format., Anal. Chem. 83 (2011) 7941–6. doi:10.1021/ac201950g.

[9] I.-H. Cho, A. Bhunia, J. Irudayaraj, Rapid pathogen detection by lateral-flow immunochromatographic assay with gold nanoparticle-assisted enzyme signal amplification., Int. J. Food Microbiol. 206 (2015) 60–6. doi:10.1016/j.ijfoodmicro.2015.04.032.

[10] C. Chen, J. Wu, A fast and sensitive quantitative lateral flow immunoassay for Cry1Ab based on a novel signal amplification conjugate., Sensors (Basel). 12 (2012) 11684–96. doi:10.3390/s120911684.

[11] R. van Reis, A. Zydney, Membrane separations in biotechnology, Curr. Opin. Biotechnol. 12 (2001) 208–211. doi:10.1016/S0958-1669(00)00201-9.

[12] H. Walter, D. Brooks, D. Fisher, Partitioning In Aqueous Two – Phase System: Theory, Methods, Uses, And Applications To Biotechnology, Academic Press, Inc, Orlando, Florida, 1985.

[13] P.U. Kenkare, C.K. Hall, Modeling of phase separation in PEG–salt aqueous two-phase systems, AIChE J. 42 (1996) 3508–3522. doi:10.1002/aic.690421220.

[14] P.- åke Albertsson, Partition of Cell Particles and Macromolecules, 3rd ed., John Wiley and Sons, 1986.

[15] J. a. Asenjo, S.L. Mistry, B. a. Andrews, J.C. Merchuk, Phase separation rates of aqueous two-phase systems: Correlation with system properties, Biotechnol. Bioeng. 79 (2002) 217–223. doi:10.1002/bit.10273.

[16] F. Mashayekhi, R.Y.T. Chiu, A.M. Le, F.C. Chao, B.M. Wu, D.T. Kamei, Enhancing the lateral-flow immunoassay for viral detection using an aqueous two-phase micellar system., Anal. Bioanal. Chem. 398 (2010) 2955–61. doi:10.1007/s00216-010-4213-7.

[17] F. Mashayekhi, A.M. Le, P.M. Nafisi, B.M. Wu, D.T. Kamei, Enhancing the lateral-flow immunoassay for detection of proteins using an aqueous two-phase micellar system., Anal. Bioanal. Chem. 404 (2012) 2057–66. doi:10.1007/s00216-012-6278-y.

[18] R.Y.T. Chiu, P.T. Nguyen, J. Wang, E. Jue, B.M. Wu, D.T. Kamei, Dextran-Coated Gold Nanoprobes for the Concentration and Detection of Protein Biomarkers., Ann. Biomed. Eng. (2014). doi:10.1007/s10439-014-1043-3.

[19] D.T. Kamei, E. Jue, C.D. Yamanishi, R.Y.T. Chiu, B.M. Wu, Using an Aqueous Two-Phase Polymer-Salt System to Rapidly Concentrate Viruses for Improving the Detection Limit of the Lateral-Flow Immunoassay., Biotechnol. Bioeng. (2014). doi:10.1002/bit.25316.

[20] R.Y.T. Chiu, E. Jue, A.T. Yip, A.R. Berg, S.J. Wang, A.R. Kivnick, P.T. Nguyen, D.T. Kamei, Simultaneous concentration and detection of biomarkers on paper., Lab Chip. 14 (2014) 3021–8. doi:10.1039/c4lc00532e.

[21] T. Rosenfeld, M. Bercovici, 1,000-fold sample focusing on paper-based microfluidic devices, Lab Chip. 14 (2014) 4465–4474. doi:10.1039/C4LC00734D.

[22] B.Y. Moghadam, K.T. Connelly, J.D. Posner, Isotachophoretic preconcenetration on paper-based microfluidic devices., Anal. Chem. 86 (2014) 5829–37. doi:10.1021/ac500780w.

[23] C.-M. Cheng, A.W. Martinez, J. Gong, C.R. Mace, S.T. Phillips, E. Carrilho, K.A. Mirica, G.M. Whitesides, Paper-based ELISA., Angew. Chem. Int. Ed. Engl. 49 (2010) 4771–4. doi:10.1002/anie.201001005.

[24] E. Fu, S.A. Ramsey, P. Kauffman, B. Lutz, P. Yager, Transport in two-dimensional paper networks., Microfluid. Nanofluidics. 10 (2011) 29–35. doi:10.1007/s10404-010-0643-y.

[25] E. Fu, T. Liang, P. Spicar-Mihalic, J. Houghtaling, S. Ramachandran, P. Yager, Two-dimensional paper network format that enables simple multistep assays for use in low-resource settings in the context of malaria antigen detection., Anal. Chem. 84 (2012) 4574–9. doi:10.1021/ac300689s.

[26] D.H. Choi, S.K. Lee, Y.K. Oh, B.W. Bae, S.D. Lee, S. Kim, Y.-B. Shin, M.-G. Kim, A dual gold nanoparticle conjugate-based lateral flow assay (LFA) method for the analysis of troponin I., Biosens. Bioelectron. 25 (2010) 1999–2002. doi:10.1016/j.bios.2010.01.019.

[27] L. Rivas, M. Medina-Sánchez, A. de la Escosura-Muñiz, A. Merkoçi, Improving sensitivity of gold nanoparticle-based lateral flow assays by using wax-printed pillars as delay barriers of microfluidics., Lab Chip. 14 (2014) 4406–14. doi:10.1039/c4lc00972j.

[28] J.C. Linnes, A. Fan, N.M. Rodriguez, B. Lemieux, H. Kong, C.M. Klapperich, Paper-based molecular diagnostic for Chlamydia trachomatis., RSC Adv. 4 (2014) 42245–42251. doi:10.1039/C4RA07911F.

[29] J. Iqbal, A. Siddique, M. Jameel, P.R. Hira, Persistent histidine-rich protein 2, parasite lactate dehydrogenase, and panmalarial antigen reactivity after clearance of Plasmodium falciparum monoinfection., J. Clin. Microbiol. 42 (2004) 4237–41. doi:10.1128/JCM.42.9.4237-4241.2004.

[30] J.C. Mouatcho, J.P.D. Goldring, Malaria rapid diagnostic tests: challenges and prospects., J. Med. Microbiol. 62 (2013) 1491–505. doi:10.1099/jmm.0.052506-0.

[31] E. Tjitra, S. Suprianto, M.E. Dyer, B.J. Currie, N.M. Anstey, Detection of histidine rich protein 2 and panmalarial ICT Malaria Pf/Pv test antigens after chloroquine treatment of uncomplicated falciparum malaria does not reliably predict treatment outcome in eastern Indonesia., Am. J. Trop. Med. Hyg. 65 (2001) 593–8. http://www.ncbi.nlm.nih.gov/pubmed/11716120 (accessed August 14, 2015).

[32] A. Bobenchik, R. Shimizu-Cohen, R.M. Humphries, Use of rapid diagnostic tests for diagnosis of malaria in the United States, J. Clin. Microbiol. 51 (2013) 379. doi:10.1128/JCM.02509-12.

[33] M.A. Dimaio, I.T. Pereira, T.I. George, N. Banaei, Performance of BinaxNOW for diagnosis of malaria in a U.S. hospital., J. Clin. Microbiol. 50 (2012) 2877–80. doi:10.1128/JCM.01013-12.

[34] D. Foster, J. Cox-Singh, D.S.A. Mohamad, S. Krishna, P.P. Chin, B. Singh, Evaluation of three rapid diagnostic tests for the detection of human infections with Plasmodium knowlesi., Malar. J. 13 (2014) 60. doi:10.1186/1475-2875-13-60.

[35] WHO, Malaria Rapid Diagnostic Test Performance. Summary results of WHO product testing of malaria RDTs: Round 1-5 (2008-2013), 2012.

[36] M. Heutmekers, P. Gillet, J. Maltha, A. Scheirlinck, L. Cnops, E. Bottieau, M. Van Esbroeck, J. Jacobs, Evaluation of the rapid diagnostic test CareStart pLDH Malaria (Pf-pLDH/pan-pLDH) for the diagnosis of malaria in a reference setting, Malar. J. 11 (2012) 204. doi:10.1186/1475-2875-11-204.

[37] G. Frens, Particle size and sol stability in metal colloids, Kolloid-Zeitschrift Und Zeitschrift Für Polym. 250 (1972) 736–741. doi:10.1007/BF01498565.

[38] F.H. Quina, W.L. Hinze, Surfactant-Mediated Cloud Point Extractions: An Environmentally Benign Alternative Separation Approach, Ind. Eng. Chem. Res. 38 (1999) 4150–4168. doi:10.1021/ie980389n.

[39] M.-C. Daniel, D. Astruc, Gold nanoparticles: assembly, supramolecular chemistry, quantum-size-related properties, and applications toward biology, catalysis, and nanotechnology., Chem. Rev. 104 (2004) 293–346. doi:10.1021/cr030698+.

[40] P.N. Njoki, I.-I.S. Lim, D. Mott, H.-Y. Park, B. Khan, S. Mishra, R. Sujakumar, J. Luo, C.-J. Zhong, Size Correlation of Optical and Spectroscopic Properties for Gold Nanoparticles, J. Phys. Chem. C. 111 (2007) 14664–14669. doi:10.1021/jp074902z.

[41] O.J. Bjerrum, J. Selmer, J. Hangaard, F. Larsen, Isolation of human erythrocyte acetylcholinesterase using phase separation with Triton X-114 and monoclonal immunosorbent chromatography., J. Appl. Biochem. 7 356–69. http://www.ncbi.nlm.nih.gov/pubmed/3912371 (accessed January 7, 2015).

[42] C.K. Murray, R.A. Gasser, A.J. Magill, R.S. Miller, Update on rapid diagnostic testing for malaria., Clin. Microbiol. Rev. 21 (2008) 97–110. doi:10.1128/CMR.00035-07.

[43] A. Moody, Rapid Diagnostic Tests for Malaria Parasites, Clin. Microbiol. Rev. 15 (2002) 66–78. doi:10.1128/CMR.15.1.66-78.2002.

[44] J.W. Jang, C.H. Cho, E.T. Han, S.S.A. An, C.S. Lim, pLDH level of clinically isolated Plasmodium vivax and detection limit of pLDH based malaria rapid diagnostic test., Malar. J. 12 (2013) 181. doi:10.1186/1475-2875-12-181.

[45] L.M. Hafner, Pathogenesis of fallopian tube damage caused by Chlamydia trachomatis infections, Contraception. 92 (2015) 108–115. doi:10.1016/j.contraception.2015.01.004.

[46] Centers for Disease Control and Prevention, Sexually Transmitted Disease Surveillance 2014, (2014) 1–176. doi:10.1136/bmj.289.6437.99.

[47] K. Krupp, P. Madhivanan, Antibiotic resistance in prevalent bacterial and protozoan sexually transmitted infections., Indian J. Sex. Transm. Dis. 36 (2015) 3–8. doi:10.4103/0253-7184.156680.

[48] CDC, Diagnoses of HIV Infection in the United States and Dependent Areas, 2015, HIV Surveill. Rep. 27 (2015) 1–82. doi:10.1017/CBO9781107415324.004.

[49] W. Huang, C. Gaydos, M. Barnes, M. Jett-Goheen, D.R. Blake, Comparative effectiveness of a rapid point-of-care test for detection of Chlamydia trachomatis among women in a clinical setting, Sex Transm Infect. 89 (2013) 108–114. doi:10.1136/sextrans-2011-050355.

[50] W.C. Miller, Screening for Chlamydial Infection, Sex. Transm. Infect. 25 (1998) 201–211.

[51] L. Mahilum-Tapay, V. Laitila, J.J. Wawrzyniak, H.H. Lee, S. Alexander, C. Ison, A. Swain, P. Barber, I. Ushiro-Lumb, B.T. Goh, New point of care Chlamydia Rapid Test--bridging the gap between diagnosis and treatment: performance evaluation study., BMJ. 335 (2007) 1190–4. doi:10.1136/bmj.39402.463854.AE.

[52] N. Low, N. Broutet, Y. Adu-Sarkodie, P. Barton, M. Hossain, S. Hawkes, Global control of sexually transmitted infections, Lancet. 368 (2006) 2001–2016. doi:10.1016/S0140-6736(06)69482-8.

[53] R. Wong, H. Tse, Lateral Flow Immunoassay, 1st ed., Springer, New York, 2009.

[54] J.A. Land, J.E.A.M. Van Bergen, S.A. Morre, M.J. Postma, Epidemiology of Chlamydia trachomatis infection in women and the cost-effectiveness of screening, Hum. Reprod. Update. 16 (2009) 189–204. doi:10.1093/humupd/dmp035.

[55] V. Gubala, L.F. Harris, A.J. Ricco, M.X. Tan, D.E. Williams, Point of care diagnostics: Status and future, Anal. Chem. 84 (2012) 487–515. doi:10.1021/ac2030199.

[56] Y. Xu, M. Liu, N. Kong, J. Liu, Lab-on-paper micro- and nano-analytical devices: Fabrication, modification, detection and emerging applications, Microchim. Acta. 183 (2016) 1521–1542. doi:10.1007/s00604-016-1841-4.

[57] E. Fu, B. Lutz, P. Kauffman, P. Yager, Controlled reagent transport in disposable 2D paper networks., Lab Chip. 10 (2010) 918–920. doi:10.1039/b919614e.

[58] J.L. Osborn, B. Lutz, E. Fu, P. Kauffman, D.Y. Stevens, P. Yager, Microfluidics without pumps: reinventing the T-sensor and H-filter in paper networks., Lab Chip. 10 (2010) 2659–65. doi:10.1039/c004821f.

[59] G.E. Fridley, H.Q. Le, E. Fu, P. Yager, Controlled release of dry reagents in porous media for tunable temporal and spatial distribution upon rehydration, Lab Chip. 12 (2012) 4321. doi:10.1039/c2lc40785j.

[60] B. Lutz, T. Liang, E. Fu, S. Ramachandran, P. Kauffman, P. Yager, Dissolvable fluidic time delays for programming multi-step assays in instrument-free paper diagnostics., Lab Chip. 13 (2013). doi:10.1039/c3lc50178g.

[61] M.M. Thuo, R. V. Martinez, W.J. Lan, X. Liu, J. Barber, M.B.J. Atkinson, D. Bandarage, J.F. Bloch, G.M. Whitesides, Fabrication of low-cost paper-based microfluidic devices by embossing or cut-and-stack methods, Chem. Mater. 26 (2014) 4230–4237. doi:10.1021/cm501596s.

[62] W. Lan, X.U. Zou, M.M. Hamedi, J. Hu, C. Parolo, E.J. Maxwell, P. Bu, G.M. Whitesides, Paper-Based Potentiometric Ion Sensing, Anal. Chem. 86 (2014) 9548–9553.

[63] A.K. Badu-Tawiah, S. Lathwal, K. Kaastrup, M. Al-Sayah, D.C. Christodouleas, B.S. Smith, G.M. Whitesides, H.D. Sikes, Polymerization-based signal amplification for paper-based immunoassays., Lab Chip. 15 (2014) 655–659. doi:10.1039/c4lc01239a.

[64] N.A. Taranova, A.E. Urusov, E.G. Sadykhov, A. V. Zherdev, B.B. Dzantiev, Bifunctional gold nanoparticles as an agglomeration-enhancing tool for highly sensitive lateral flow tests: a case study with procalcitonin, Microchim. Acta. (2017) 1–7. doi:10.1007/s00604-017-2355-4.

[65] D.H. Choi, S.K. Lee, Y.K. Oh, B.W. Bae, S.D. Lee, S. Kim, Y.-B. Shin, M.-G. Kim, A dual gold nanoparticle conjugate-based lateral flow assay (LFA) method for the analysis of troponin I, Biosens. Bioelectron. 25 (2010) 1999–2002. doi:10.1016/j.bios.2010.01.019.

[66] N. Wiriyachaiporn, W. Maneeprakorn, C. Apiwat, T. Dharakul, Dual-layered and double-targeted nanogold based lateral flow immunoassay for influenza virus, Microchim. Acta. 182 (2015) 85–93. doi:10.1007/s00604-014-1303-9.

[67] X. Fu, Y. Chu, K. Zhao, J. Li, A. Deng, Ultrasensitive detection of the β-adrenergic agonist brombuterol by a SERS-based lateral flow immunochromatographic assay using flower-like gold-silver core-shell nanoparticles, Microchim. Acta. 184 (2017) 1711–1719. doi:10.1007/s00604-017-2178-3.

[68] D.Y. Pereira, R.Y.T. Chiu, S.C.L. Zhang, B.M. Wu, D.T. Kamei, Single-step, paper-based concentration and detection of a malaria biomarker, Anal. Chim. Acta. 882 (2015) 83–89. doi:10.1016/j.aca.2015.04.040.

[69] H. Jang, S.R. Ryoo, K. Kostarelos, S.W. Han, D.H. Min, The effective nuclear delivery of doxorubicin from dextran-coated gold nanoparticles larger than nuclear pores, Biomaterials. 34 (2013) 3503–3510. doi:10.1016/j.biomaterials.2013.01.076.

[70] M.-C. Daniel, D. Astruc, Gold Nanoparticles: Assembly, Supramolecular Chemistry, Quantum - Size - Related Properties, and Applicationstoward Biology, Catalysis, and Nanotechnology, Chem. Rev. 104 (2004) 293–346.

[71] P.N. Njoki, I.I.S. Lim, D. Mott, H.-Y. Park, B. Khan, S. Mishra, R. Sujakumar, J. Luo, C.J. Zhong, Size correlation of optical and spectroscopic properties for gold nanoparticles, J. Phys. Chem. C. 111 (2007) 14664–14669. doi:10.1021/jp074902z.

[72] R.A. Wooding, H.J. Morel-Seytoux, Multiphase Fluid Flow Through Porous Media, Annu. Rev. Fluid Mech. 8 (1976) 233–274.

[73] R. Hatti-kaul, Aqueous Two-Phase Systems Methods and Protocols, 1st ed., Humana Press, 2000.

[74] S.A. Morse, Binary Solutions and the Lever Rule Revisited, J. Geol. 105 (1997) 471–482.

[75] J.R. Choi, Z. Liu, J. Hu, R. Tang, Y. Gong, S. Feng, H. Ren, T. Wen, H. Yang, Z. Qu, B. Pingguan-Murphy, F. Xu, Polydimethylsiloxane-Paper Hybrid Lateral Flow Assay for Highly Sensitive Point-of-Care Nucleic Acid Testing, Anal. Chem. 88 (2016) 6254–6264. doi:10.1021/acs.analchem.6b00195.

[76] S. Bäckström, J. Benavente, R. W. Berg, K. Stibius, M. S. Larsen, H. Bohr, C. Hélix-Nielsen, Tailoring Properties of Biocompatible PEG-DMA Hydrogels with UV Light, Mater. Sci. Appl. 3 (2012) 425–431. doi:10.4236/msa.2012.36060.

[77] A.S. Hoffman, Hydrogels for biomedical applications, Adv. Drug Deliv. Rev. 64 (2012) 18–23. doi:10.1016/j.addr.2012.09.010.

[78] A.G. Lee, C.P. Arena, D.J. Beebe, S.P. Palecek, Development of macroporous poly(ethylene glycol) hydrogel arrays within microfluidic channels, Biomacromolecules. 11 (2010) 3316–3324. doi:10.1021/bm100792y.

[79] K. Deligkaris, T.S. Tadele, W. Olthuis, A. van den Berg, Hydrogel-based devices for biomedical applications, Sensors Actuators, B Chem. 147 (2010) 765–774. doi:10.1016/j.snb.2010.03.083.

[80] N. Annabi, J.W. Nichol, X. Zhong, C. Ji, S. Koshy, A. Khademhosseini, F. Dehghani, Controlling the porosity and microarchitecture of hydrogels for tissue engineering., Tissue Eng. Part B. Rev. 16 (2010) 371–383. doi:10.1089/ten.teb.2009.0639.

[81] J. Kobayashi, A. Kikuchi, K. Sakai, T. Okano, Aqueous chromatography utilizing hydrophobicity-modified anionic temperature-responsive hydrogel for stationary phases, J. Chromatogr. A. 958 (2002) 109–119. doi:10.1016/S0021-9673(02)00388-6.

[82] M.B. Dainiak, I.Y. Galaev, A. Kumar, F.M. Plieva, B. Mattiasson, Chromatography of living cells using supermacroporous hydrogels, cryogels, Adv. Biochem. Eng. Biotechnol. 106 (2007) 101–127. doi:10.1007/10_2006_044.

[83] R.R. Niedl, C. Beta, Hydrogel-driven paper-based microfluidics., Lab Chip. 15 (2015) 2452–9. doi:10.1039/c5lc00276a.

[84] X. Yan, J. Wang, L. Zhu, J.J. Lowrey, Y. Zhang, W. Hou, J. Dong, Y. Du, A ready-to-use, versatile, multiplex-able three-dimensional scaffold-based immunoassay chip for high throughput hepatotoxicity evaluation, Lab Chip. 15 (2015) 2634–2646. doi:10.1039/C5LC00313J.

[85] D. Puchberger-Enengl, C. Krutzler, F. Keplinger, M.J. Vellekoop, Single-step design of hydrogel-based microfluidic assays for rapid diagnostics, Lab Chip. 14 (2014) 378–383. doi:10.1039/C3LC50944C.

[86] R. Lucas, Ueber das Zeitgesetz des kapillaren Aufstiegs von Flüssigkeiten, Kolloid-Zeitschrift. 23 (1918) 15–22. doi:10.1007/BF01461107.

[87] E.W. Washburn, The Dynamics of Capillary Flow, Phys. Rev. 17 (1921) 273–283. doi:10.1103/PhysRev.17.273.

[88] W. Ostwald, Ueber die Geschwindigkeitsfunktion der Viskosität disperser Systeme. I, Kolloid-Zeitschrift. 36 (1925) 99–117. doi:10.1007/BF01431449.

[89] A. de Waele, Viscometry and plastometry, Oil Color Chem Assoc J. 6 (1923) 33–88.

[90] S. Cito, Y.-C. Ahn, J. Pallares, R.M. Duarte, Z. Chen, M. Madou, I. Katakis, Visualization and measurement of capillary-driven blood flow using spectral domain optical coherence tomography, Microfluid Nanofluidics. 13 (2012) 227–237. doi:10.1007/s10404-012-0950-6.

[91] C.L.A. Berli, R. Urteaga, Asymmetric capillary filling of non-Newtonian power law fluids, Microfluid. Nanofluidics. 17 (2014) 1079–1084. doi:10.1007/s10404-014-1388-9.

[92] R.M. Digilov, Capillary Rise of a Non-Newtonian Power Law Liquid: Impact of the Fluid Rheology and Dynamic Contact Angle, Langmuir. 24 (2008) 13663–13667. doi:10.1021/la801807j.

[93] R.B. Bird, R.C. Armstrong, O. Hassager, C. Curtiss, Dynamics of polymeric liquids, Wiley, New York, 1977.

[94] Z.-P. Liang, X.-D. Wang, Y.-Y. Duan, Q. Min, C. Wang, D.-J. Lee, Dynamic Wetting of Non-Newtonian Fluids: Multicomponent Molecular-Kinetic Approach, Langmuir. 26 (2010) 14594–14599. doi:10.1021/la102041q.

[95] H.-N. Xu, S.-F. Ma, Effect of Temperature on Viscosity of Aqueous Triton X-114 Solution, J. Chem. Eng. Data. 56 (2011) 2677–2679. doi:10.1021/je100775e.

[96] I. Mukherjee, K. Manna, G. Dinda, S. Ghosh, S.P. Moulik, Shear- and Temperature-Dependent Viscosity Behavior of Two Phosphonium-Based Ionic Liquids and Surfactant Triton X-100 and Their Biocidal Activities, J. Chem. Eng. Data. 57 (2012) 1376–1386. doi:10.1021/je200938k.